A THREE-DIMENSIONAL NUMERICAL SIMULATION OF A HAILSTORM

by

© Stephen Macpherson

A thesis submitted to the Faculty of Graduate Studies and Research
in partial fulfillment of the requirements for a degree of
Master of Science.

Department of Meteorology
McGill University
Montreal, Quebec

October 1981

ABSTRACT

A graupel parameterization scheme, essentially that suggested by Stephens (1979), is added to the three-dimensional cumulus convection model developed by Steiner (1973) and updated by Yau (1979b, 1980a). The bulk water parameterization assumes graupel follows an inverse exponential distribution with a constant number concentration. Graupel microphysical processes include conversion of ice crystals to graupel, raindrop freezing by the Bigg (1953) process and contact with ice crystals, accretion of raindrops, riming of cloud droplets, vapor deposition, sublimation, and melting. Rain and graupel are allowed to precipitate.

Two- and three-dimensional simulations of a hailstorm are performed and the results of the latter are compared with an observed storm reported by Chisholm (1970) and the two-dimensional run. Results of the three-dimensional experiment show good general agreement with the observed storm and with features commonly present in observation and other simulated storms. Some modifications are suggested to the model to better simulate certain specific features, thus making it a more useful tool in the study of hailstorms.

RÉSUMÉ

Une forme de paramétrisation de la neige roulée, telle que suggérée essentiellement par Stephens (1979), a été ajoutée au modèle en trois dimensions de convection des cumuli développé par Steiner (1973) et mis à jour par Yau (1979b, 1980a). La paramétrisation du volume en eau assume que la neige roulée suit une distribution exponentielle inversée avec un nombre de concentration constant. Le procédé microphysique de la neige roulée comprend la conversion de cristaux de glace en neige roulée, le gel des gouttes de pluie selon le procédé de Bigg (1953) ou encore dû au contact avec des cristaux de glace, l'accrétion de gouttes de pluie, la transformation des gouttelettes de nuage en givre, le dépôt de la vapeur, la sublimation et la fonte. À l'intérieur du modèle, il est possible pour la pluie et la neige roulée de précipiter.

Des simulations en deux et trois dimensions d'un orage accompagné de grêle ont été fait; les résultats de ce dernier ont ensuite été comparés à ceux du précédent de même qu'aux observations recueillies par Chisholm (1970) lors d'un orage. Les résultats obtenus par le modèle en trois dimensions présentent une bonne corrélation avec les données provenant de l'orage observé, de même qu'avec les particularités généralement rencontrées au cours des orages réels ou simulés. Toutefois, si l'on tient compte des quelques modifications suggérées, le modèle pourrait mieux simuler certains traits particuliers et ainsi devenir un outil important dans l'étude des orages accompagnés de grêle.

ACKNOWLEDGMENTS

The author wishes to express his deep appreciation to Dr. M. K. Yau for his interest, guidance and support as thesis supervisor. In addition I would like to thank Dr. R. R. Rogers for his help and concern during a difficult time. The efforts and support above and beyond the call of duty of Ms. Lisa Appleton in figure drafting, proofreading and typing of this thesis are as well deeply appreciated. The constant help of the department secretary, Mrs. Kathy Peterson, much appreciated by the author, must also be mentioned.

This research was supported by the National Science and Engineering Research Council, McGill University, and the Atmospheric Environment Service of Canada. Thanks are also extended to the McGill University Amdahl V7 computer for its tireless efforts in executing the long and complex program to give, if somewhat slowly, the results presented in this work.

TABLE OF CONTENTS

LIST OF FIGURES

Note: An asterisk (*) indicates that the figure is on the facing page.

LIST OF SYMBOLS

Symbol	Explanation	Value	Units
a	Constant in equation for terminal velocity of ice/snow	2.07	
a'	Autoconversion threshold	10^{-6}	$g\ cm^{-3}$
A'	Constant in Bigg's freezing	0.66	K^{-1}
a_1, a_2	Temperature-dependent parameters used in calculating deposition rate for ice crystals	see Koenig (1972)	
AC	Autoconversion rate		$g\ g^{-1}\ s^{-1}$
ADVEC	Advection		
B	Buoyancy		$cm\ s^{-2}$
B'	Constant in Bigg's freezing	10^{-4}	$cm^{-3}\ s^{-1}$
b	Constant in equation for terminal velocity of ice/snow	0.31	
C_D	Drag coefficient	0.6	
C_p	Specific heat of dry air at constant pressure	1.005×10^7	$erg\ g\ K^{-1}$
CC	Cloud collection (accretion) by rain		$g\ g^{-1}\ s^{-1}$
COND	Rate of condensation		$g\ g^{-1}\ s^{-1}$
CONTH	Rate of raindrop contact freezing		$g\ g^{-1}\ s^{-1}$
CONV	Rate of ice/snow conversion to graupel		$g\ g^{-1}\ s^{-1}$
D	Diameter of a graupel particle		cm

Symbol	Explanation	Value	Units
$\overline{D}$	Mean diameter of graupel distribution		cm
D_m	Melted diameter of an ice crystal		cm
D_{oi}	Ice particle "median volume diameter"		cm
D_r	Diameter of a raindrop		cm
$\overline{D}_r$	Mean diameter of rain distribution		cm
DEP	Rate of vapor deposition onto ice/snow		$g\ g^{-1}\ s^{-1}$
DEPH	Rate of deposition onto graupel distribution		$g\ g^{-1}\ s^{-1}$
DIFFU	Diffusion		
$E(D_r \backslash D)$	Efficiency of collection/coalescence for graupel	1.0	
E_{gr}	Efficiency of riming for graupel	1.0	
E_i	Collection efficiency of an ice crystal	1.0	
$\overline{E}_i$	Average collection efficiency of ice/snow	1.0	
$e_{si}(T)$	Saturation vapor pressure over a flat ice surface		dynes cm^{-2}
EVPC	Rate of cloud evaporation		$g\ g^{-1}\ s^{-1}$
EVPR	Rate of evaporation of rain		$g\ g^{-1}\ s^{-1}$
f(Re)	Ventilation factor		
$f(Re)_g$	Ventilation function for graupel distribution		
F_i	Sub-grid-scale force		$cm\ s^{-2}$
FALLOUT	Rate of fallout of precipitating particles		$g\ g^{-1}\ s^{-1}$
g	Acceleration due to gravity	980.	$cm\ s^{-2}$
G(T,p)	Function of T and p for vapor deposition on ice		$g\ s^{-1}\ cm^{-2}$
GLAC	Rate of glaciation of cloud water		$g\ g^{-1}\ s^{-1}$
H	Height of domain	24	km

Symbol	Explanation	Value	Units
HCOL	Rate of rain collection by graupel distribution		$g\ g^{-1}\ s^{-1}$
K	Autooonversion rate constant	10^{-3}	s^{-1}
K'	Molecular thermal conductivity of air	2360.0	$erg\ cm^{-1}\ s^{-1}\ K^{-1}$
k	Constant (in fallspeed height factor)	10^{-4}	m^{-1}
k'	Constant in expression for eddy coefficient	0.1764	
$\|K\|_{ice}$	Dielectric constant for ice	0.436	
$\|K\|_{water}$	Dielectric constant for water	1.0	
L_{li}	Latent heat of freezing	3.336×10^{9}	$erg\ g^{-1}$
L_{vi}	Latent heat of sublimation	2.837×10^{10}	$erg\ g^{-1}$
L_{vl}	Latent heat of condensation		$erg\ g^{-1}$
m	Mass of a particle		g
$\overline{m}$	Mean mass of graupel distribution		g
$m_g(D)$	Mass of graupel particle as function of diameter		g
m_i	Mass of a single ice crystal		g
MELT	Rate of melting for ice/snow		$g\ g^{-1}\ s^{-1}$
MELTH	Rate of graupel melting		$g\ g^{-1}\ s^{-1}$
N(D)	Graupel exponential size distribution		cm^{-4}
N_i	Existing number of ice particles at a point		g^{-1}
$N_i(D_m)$	Snow exponential size distribution		cm^{-4}
N_n	Maximum number of ice nuclei activated		g^{-1}
N_{og}	Graupel distribution intercept		cm^{-4}
N_{oi}	Snow distribution intercept		cm^{-4}
N_{or}	Rain distribution intercept	0.1	cm^{-4}
$N_r(D_r)$	Rain exponential size distribution		cm^{-4}

Symbol	Explanation	Value	Units
N_{tg}	Total number concentration of graupel particles	10^{-4}	cm^{-3}
N_{tr}	Total number concentration of raindrops		cm^{-3}
NUCLEA	Rate of nucleation		$g\ g^{-1}\ s^{-1}$
p	Air pressure		dynes cm^{-2}
p_{00}	Sea-level air pressure	10^{6}	dynes cm^{-2}
PIFR	Rate of raindrop freezing from Bigg's process		$g\ g^{-1}\ s^{-1}$
Q	Any variable		
q	Particle mixing ratio		$g\ g^{-1}$
q_c	Cloud water mixing ratio		$g\ g^{-1}$
q_g	Graupel mixing ratio		$g\ g^{-1}$
q_i	Ice/snow mixing ratio		$g\ g^{-1}$
q_r	Rain water mixing ratio		$g\ g^{-1}$
q_{si}	Saturation vapor mixing ratio over ice		$g\ g^{-1}$
q_v	Vapor mixing ratio		$g\ g^{-1}$
q_v'	Deviation of vapor from basic state		$g\ g^{-1}$
q_{vs}	Saturation vapor mixing ratio		$g\ g^{-1}$
R_a	Gas constant for dry air	2.878×10^{6}	$cm^{2}\ s^{-2}\ K^{-1}$
Re	Reynolds number for ice particle		
R_i	Snowfall rate		mm hr^{-1}
R_r	Rainfall rate at the surface		mm hr^{-1}
RIM	Rate of riming for ice/snow		$g\ g^{-1}\ s^{-1}$
RIMH	Rate of riming by graupel distribution		$g\ g^{-1}\ s^{-1}$
SS	Supersaturation with respect to ice		
SUBH	Rate of sublimation of graupel distribution		$g\ g^{-1}\ s^{-1}$
T	Temperature		K

Symbol	Explanation	Value	Units
t_b	Buoyancy time scale		s
T_0	Freezing temperature of water	273.15	K
t_s	Deformation time scale		s
T_{sfc}	Graupel particle surface temperature		K
u	Horizontal velocity component in x-direction		cm s^{-1}
u_i, u_j	Tensor velocity components		cm s^{-1}
v	Horizontal velocity component in y-direction		cm s^{-1}
V_i	Terminal velocity of an ice crystal		cm s^{-1}
$V_i(D_{oi})$	Terminal velocity associated with ice crystal "median volume diameter"		cm s^{-1}
$\overline{V}_g$	Mass weighted terminal velocity of graupel		cm s^{-1}
$V_g(D)$	Terminal velocity of a graupel particle		cm s^{-1}
V_r	Rain terminal velocity		cm s^{-1}
$\overline{V}_r$	Mass weighted terminal velocity of rain		cm s^{-1}
$V_r(D_r)$	Terminal velocity of raindrop with diameter D_r		cm s^{-1}
w	Vertical velocity component		cm s^{-1}
x_i	Component of distance (i=1:x, i=2:y, i=3:z direction)		cm
z	Height		m
Z_e^r	Equivalent radar reflectivity for rain		mm^6 m^{-3}
Z_e^g	Equivalent radar reflectivity for graupel		mm^6 m^{-3}
$\Gamma(x)$	Gamma function		
Δ	Grid spacing scale = $(\Delta x \Delta y \Delta z)^{1/3}$		cm
δ_{ij}	Kroneker delta (=1 if i=j, else =0)	1 or 0	

Symbol	Explanation	Value	Units
δt	Model time step		s
Δx, Δy, Δz	Grid spacing in x, y, z directions respectively	1, 1, 0.5	km
ε	Ratio of molecular weights of water to air	0.622	
θ	Total potential temperature		K
θ'	Perturbation of θ from Θ		K
$\Theta(z)$	Basic-state potential temperature		K
λ	Graupel distribution slope		cm^{-1}
λ_i	Snow distribution slope		cm^{-1}
λ_r	Rain distribution slope		cm^{-1}
$\mu(T)$	Dynamic viscosity of air		$g\ cm^{-1}\ s^{-1}$
ν_h	Eddy coefficient for velocity		
ν_m	Eddy coefficient for scalar quantities		
π	Ratio of the circumference of a circle to its diameter	3.141596	
Π''	$\pi_p' - < \pi_p' >$		
$\Pi(z)$	Basic-state non-dimensional pressure		
π_p	Total non-dimensional pressure		
π_p'	Perturbation of π_p from Π		
ρ_a	Air density (basic-state)		$g\ cm^{-3}$
ρ_g	Density of graupel particle	0.1, 0.6, or 0.9	$g\ cm^{-3}$
ρ_i	Density of ice/snow crystal	0.5	$g\ cm^{-3}$
ρ_w	Density of water	1.0	$g\ cm^{-3}$
ρ_{vsfc}	Vapor density at surface of graupel particle		$g\ cm^{-3}$
$\psi(T,p)$	Diffusivity of water vapor in air		$cm^2\ s^{-1}$
$\left.\frac{\partial\theta}{\partial z}\right\|_{moist}$	Moist adiabatic lapse rate		$°C\ cm^{-1}$
$< x >$	Horizontal average of x		

CHAPTER 1

INTRODUCTION

1.1 Background

Hailstorms are awesome displays of atmospheric violence which can cause tremendous destruction through flooding, hail damage and high winds. Tornadoes and intense electrical activity are often associated with these storms, which not only destroy property but endanger life. It is not surprising, then, that hailstorms have been the object of a great deal of research. An important tool in this research is the use of models, which combine the results of detailed observations with theoretical research to yield a better understanding of hailstorms. With improved understanding, an effort can be made to predict and control storms in order to protect property and lives. In the latter aspect, numerical cloud models are particularly useful in testing new theories of hail suppression before they are applied to actual storms.

Due to the limitations of present-generation computers, numerical models of cumulus convection have had to emphasize either the dynamics or the microphysics, although both are interdependent and equally important.

A survey of the literature, presented in Chapter 2, reveals that detailed microphysics is used in models with simplified dynamics while simpler "bulk water" techniques are used in more dynamically complex models.

In general, models are usually classified according to the number of spatial dimensions, the simplest models (fewest dimensions) being used for detailed investigation into microphysical processes, and the more complex models used in connection with simplified "bulk water" microphysical parameterizations to capture more realistically the large-scale storm features and dynamical-microphysical interactions. The simplest model, sometimes labeled "zero-dimensional" (0D), essentially represents a single point in the atmosphere where temperature, pressure, updraft, etc. are held constant. The next step in complexity is the one-dimensional (1D) model, in which environmental conditions are simply functions of the vertical distance (z). Only the up-and-down motion of particles in an updraft/downdraft vertical profile can be followed. If a parcel of air is followed, the model is called Lagrangian (1DL), while a one-dimensional time-dependent model (1DT) allows vertical profiles to vary with time. Two dimensions (2D) give added realism but increased complexity and computational load. These models often assume symmetry conditions and are either slab-symmetric or axisymmetric. Two-dimensional flow and other fields can vary with time (2DT) or can be constant (streamline).

The most complex model is a three-dimensional time-dependent model (3DT), used rarely in the past in numerical cloud simulations due mainly to excessive taxing of economic and computer resources. Steiner (1973) was one of the first to develop a 3DT numerical model of convection and, since that time, relatively few other 3D models have been used in storm simulations even though the limitations of one- and two-dimensional models are well-known. With fewer than three dimensions, important features such as three-dimensional wind shear, turbulence and storm rotation are impossible to simulate while the effects of unnaturally restricting updrafts and downdrafts to a vertical line (1D) or plane (2D) can greatly affect storm development. As the dynamics cannot be realistically simulated in one or two dimensions, the important microphysical-dynamical interactions cannot be faithfully reproduced either.

A three-dimensional model is therefore necessary to simulate a hailstorm which is generally embedded in a wind field that varies both in direction and magnitude with height. However, just as realistic simulations of hailstorms cannot be expected from 1D or 2D models, neither can they be expected in 3D models without the inclusion of a comprehensive microphysical scheme that includes the ice phase. The ice phase consists of several types of ice particles for which the terminology is not exactly standardized. Pruppacher and Klett (1978), in their textbook on cloud microphysics, suggest the following definitions of ice particles. The primary ice particle is the ice or snow crystal which is nucleated from the vapor or from the freezing of supercooled cloud droplets at sub-zero temperatures. They can have various crystalline shapes (needles, dendrites, hexagonal plates, etc.) and grow by vapor deposition only. Ice crystals are usually no more than 5 mm in diameter and have small terminal fallspeeds. Snowflakes are aggregates of ice crystals and are generally less than 2 cm in diameter. Ice crystals can grow to a size that enables them to rime (approximately 300μm in diameter). When the features of the rimed ice crystal still resemble the original ice crystal, it is simply called a rimed ice crystal, but when the features of the primary ice particle are faintly or no longer visible, the rimed ice crystal is referred to as graupel.

Graupel, sometimes called soft hail or snow pellet, is white, opaque, and has a "fluffy" appearance due to the aggregation of the collected droplets which have frozen onto the ice crystal in such a way as to create an air-filled capillary system. Graupel particles are conical, rounded or irregular in shape and have bulk densities less than 0.8 g cm^{-3}. Hard, transparent, globular or irregular ice particles that originate as frozen drops or ice crystals which have melted and refrozen are referred to as "type a" ice pellets or sleet and have bulk densities between the density of ice and 0.99 g cm^{-3}. Small hail particles or "type b" ice pellets originate as frozen drops or ice crystals which have grown by riming into irregular or roundish semi-transparent particles. They often have water in a capillary system and typically have bulk densities between 0.8 and 0.99 g cm^{-3}. Hailstones are rimed ice crystals, graupel or ice pellets which have grown by the collection of liquid water into roundish, ellipsoidal or conical ice particles of relatively high bulk density. Maximum hailstone diameters are generally greater than 5 mm, which is the maximum diameter of the other rimed crystal particles mentioned above. Hailstones are partially to completely opaque and often have lobes or other protuberances on the surface. Growth centers often found at the center of onion-type layered hailstones, sometimes called "hail embryos", have been identified as both frozen raindrops and graupel. Depending on environmental conditions, graupel and hail can contain significant "liquid water fractions" which can be shed as drops or ejected as ice splinters, providing another source of ice crystals.

The ice phase can play an important role in convective dynamics and precipitation development in storms. It can be a significant source (and sink) of latent heat through melting, freezing and vapor transfers while "loading" by the heavier ice particles can significantly affect the air flow. Often the ice phase is the main source of precipitation in supercooled mid-latitude cumuli and should not be neglected in numerical models of such clouds. Obviously, it is essential for simulating hailstorms with cloud models.

1.2 Purpose of this research

At the time of writing, no results from a 3DT model with comprehensive ice phase microphysics have been published. Therefore, in response to the need for a useful numerical model capable of simulating hailstorms realistically, a bulk water graupel parameterization suggested by Stephens (1979) is modified slightly and added to the Steiner (1973)-Yau (1979b, 1980a) 3DT cumulus cloud model (which previously modeled cloud, rain and ice/snow crystals). The results are compared with an observed hailstorm, presented by Chisholm (1970), and a 2D run. It is hoped that this model will be useful in further research into hailstorms and storm modification.

1.3 Chapter outline

A review of previous research associated with hailstorms is presented in Chapter 2. The model is described in Chapter 3 and the observed storm is presented in Chapter 4. Chapter 5 presents the results from the 3D simulation which are discussed and compared to the observed storm and a 2D run in Chapter 6. The main points are summarized in Chapter 7, which concludes with suggestions for further work.

CHAPTER 2

LITERATURE REVIEW OF HAILSTORM RESEARCH

For the purpose of this review, research into hailstorms will be divided into three related areas: observational, theoretical and modeling. Much work has been done in each area, but as this thesis deals with numerical cloud modeling, the emphasis will be placed on the last category.

2.1 Observational research

Observational research can both lead to and verify theoretical research. Here, the observational research is subdivided into the detailed study of hailstones (small-scale) and hailstorms (large-scale).

The first category is concerned with the detailed examination of hailstones collected during hailstorms. Observations are made on stone properties such as density, shape, size and structure. Theories of stone origin, growth modes and processes in the storm, and stone trajectories, are advanced. For example, the observed layered structure and large size of many hailstones led to theories of hail growth which involved complex trajectories and/or high liquid water contents in the growth area. The existence of "growth centers" or "hail embryos" at the center of some stones suggested that hail originates as frozen drops or rimed ice crystals. Some examples of relatively recent work in this area of research are the studies by Knight and Knight (1970a, b, c) and English (Chisholm and English, 1973).

The second branch of observational research deals with the in-depth probes into the large-scale storm features such as storm structure and evolution, types of hydrometeors and precipitation, and storm motion. Airplanes, radiosondes, balloon tracking, direct visual observation, and radar are the approaches often used. This type of observational data serves as a basis for conceptual models and theories on storm convection, precipitation effects on storm development and structure, and the interaction of storms with the environment. Thus, while the small-scale study of hailstones contributes to a better understanding of storm microphysics, the study of large-scale hailstorm features provides insight into the storm dynamics.

Browning and Ludlam (1960) presented a detailed radar study of a storm which occurred near Wokingham, England. Several echo features were observed: "echo walls", "overhangs", and "echo-free vaults". Also observed was "discrete propagation", which occurred when new cells developed in the vicinity of existing cells. Similar features were observed in many Alberta hailstorms, examined by Chisholm (1970). A common element was found in all the storms -- a "weak echo region" (WER), equivalent to Browning and Ludlam's "echo-free vault", found in association with cloud base updrafts. Chisholm hypothesized that the WER consists of freshly-formed micron-sized cloud droplets in the core of a strong updraft.

Marwitz (1972) used data from an array of observational systems to propose a classification scheme for Alberta hailstorms. The four storm types in this scheme were supercells, multicells, severely sheared storms and squall lines. All of the observational studies mentioned above eventually led to descriptive models of hailstorms.

2.2 Theoretical research

Often stemming from observations, this kind of research deals with the highly theoretical, usually mathematical, study of the formation, growth, and structure of hailstones and hailstorms. It provides the mathematical framework for numerical hailstorm models while observational research provides the conceptual nature of models. Typical of such research are the microphysical studies by List (1963) and Macklin (1962, 1963) in which numerous expressions were derived to describe hailstone growth using heat and mass balance equations.

2.3 Models

Hailstorm models represent a vehicle for the incorporation of past observational and theoretical research into a representative picture of a hailstorm in an effort to better understand its complex nature. As such, a model can never hope to totally represent all hailstorms, but it can capture or simulate important features found in many storms. Model results can either prove the validity of the theories and concepts which make up the model, or they can indicate in what areas the theories and concepts are deficient.

Just as theoretical and observational research can focus on different aspects of hailstorms, from the small-scale microphysics to the large-scale storm features and dynamics, numerical models also can emphasize different aspects but generally fall into two main branches. One branch makes simplifying assumptions about environmental and dynamical aspects in order to examine in detail the microphysics of hydrometeor formation and growth. The other seeks to simulate larger-scale aspects of the storm involving the important interaction between cloud dynamics and microphysics. Models of this type usually employ "bulk water" microphysical parameterizations to simplify the modeling of hydrometeors so as not to add too much complexity to the already complex dynamical framework. Both types of models will be discussed as well as a few others which do not fit neatly into either category.

2.3.1 Detailed microphysics

A number of models examine the growth of artificially injected hail embryos, assumed to be frozen drops, into hailstones by the accretion of liquid water. The results of most of these models led to differing conclusions about the necessary conditions for the growth of hail embryos into large hailstones.

Ludlam (1958) developed a simple 1D steady-state model in which the up-down motion of a few relatively large frozen raindrops (hail embryos), injected in the lower levels of the cloud, was followed in the updraft. These particles could grow into hailstones by accretion and could rise and fall back through the updraft accreting the same water (as the water was not depleted by the hailstones in this model). Heat balance considerations led to the shedding of that portion of the accreted supercooled water which could not be frozen, limiting the sizes obtained by the hailstones to no more than 3 cm in diameter. These results led to the idea that complex trajectories with recycling or high liquid water contents must be necessary for the production of large hail observed in many severe hailstorms. Browning and Ludlam (1962) developed an intricate three-dimensional flow pattern for the Wokingham storm. This conceptual airflow model allowed for the recycling of hailstones as suggested by Ludlam to produce large hail. However, the time involved in producing large hail by this complex process does not agree with observation. For example, in Alberta, Hitschfeld and Douglas (1963) found that the first report of hail at the surface could follow the first radar appearance of a storm in as short a time as 20 minutes, not enough time for the recycling theory to explain the size of the reported hail. Thus they assumed that there must be regions of very high liquid water content in the cloud where hail can quickly grow to observed sizes through accretion of the liquid water. Using this assumption, they developed a model in which large hailstones (up to 5.8 cm in diameter) could be produced in 20 minutes or less in a simple up-down trajectory. However, as English (Chisholm and English, 1973) pointed out, the stones were not allowed to shed the collected water and unrealistically high liquid fractions resulted.

Other simple 1D steady-state models showed that large hail greater than 1 cm in diameter could be grown in simple up-down trajectories and in relatively short times (10 to 20 minutes) without exceptionally high liquid water contents. Gokhale and Rao (1969) released hail embryos near the top of a cloud (assumed to be the region of rain accumulation) and followed their descent through an adiabatic updraft to the 0°C level. List et al (1968) injected different concentrations of embryos at the freezing level and followed their ascent in an updraft. A similar study by Charlton and List (1972), which allowed the stones to deplete the liquid water content, also showed that large hail could be produced without complex trajectories or high liquid water contents.

Based on extensive field data of hailstorm updrafts, liquid water contents and structure as observed by airplane and radar, a 2D streamline cloud model was used by English (Chisholm and English, 1973) to follow the trajectories and growth of millimeter-sized embryos, injected at various points in a tilted updraft. Wet and dry growth modes for the hailstones were simulated as they grew by the collection of liquid water. Depending on the storm modeled, the stones were assumed to be either oblate or spherical. In the updraft, the embryos grow to radar-detectable size and then fall along the edge of the updraft to the surface, forming a "precipitation cascade". In this way such observed radar features as the weak echo region, corresponding to the region of maximum updrafts, bounded by regions of higher reflectivity (the "overhang" and the "wall") were simulated. Other features which compared well with observations were computed hail sizes, liquid fractions and growth times. It was concluded that embryo formation which allowed one ascent in a strong updraft and one descent adjacent to the updraft was sufficient for the growth of even the largest hail reported for the observed storms.

Dennis and Musil (1973) used a 1DT model to examine the wet and dry growth of hailstones. The heat and mass budget of the stones were assumed to be a function of their size and environmental conditions. Hail embryos, hypothesized to be drops of 100 μm diameter, were injected at the cloud base every five minutes and were assumed to totally freeze at the -5°C level. The subsequent ascent and descent of the frozen drops were followed as they grew by accretion of cloud water and the collection of cloud ice into hailstones. Liquid water was incorporated into the stones to simulate spongy growth, and such stones were allowed to break up when their diameters reached a critical value determined by the liquid fraction. They concluded that the important factors which dictate the hailstone diameter at the ground were the maximum updraft strength and the temperature level at which it occurs. Higher updraft strengths resulted in larger stones while the -30°C level seemed to be the optimum level for the updraft maximum to produce the largest hail at the ground.

OD models were used to investigate the growth of single ice crystals which, in addition to frozen drops, can also act as hail embryos through riming. Results from these models include the time necessary for ice crystals to grow large enough to rime significantly, thereby becoming hail embryos (or graupel).

Jayaweera (1971) examined the diffusional growth of ice crystals of different shapes in a constant environment, the crystal shape being a function of temperature. Crystals grew to riming size (approximately 300 μm in "diameter") in three to eight minutes. A similar model was developed by Koenig (1971) and produced riming-size crystals in a similar time scale -- two to six minutes. The computations were used to derive a useful parameterized equation relating the depositional growth rate to the ice crystal mass and the environmental temperature. A more sophisticated model was used by Hindman and Johnson (1972) to investigate both the growth of crystals to riming size and the growth of rimed crystals into spherical ice particles ("graupel"). For this purpose, a distribution of supercooled cloud droplets was assumed and the crystal fallspeeds and riming efficiencies were calculated. Assuming a cloud water content of 1 g cm^{-3}, crystals could grow to riming size in one to three minutes and "graupel" was formed in three to ten minutes.

More complex models were also used to study ice and hail growth processes and interactions. A large number of size categories were employed and the stochastic collection equation was used to calculate growth by the collection processes. In contrast to the papers cited above, the process of hail (or graupel) initiation from both rimed ice crystals and frozen drops (occurring naturally rather than being artificially injected) is explicitly modeled in all but the first of these models.

Danielson et al (1972) modeled cloud, rain, and hail using a model in which parcels were released from the surface every 30 seconds. As ice crystals were not included in this model, hail was initialized by drop freezing only. The initial cloud droplet distribution was varied to investigate the subsequent effects on hail growth. Precipitation-sized particles were allowed to fall out of each parcel, affecting the parcels below it, and hydrometeors could alter the updraft substantially through "loading". It was found that hail growth depended on the updraft speed, surface mixing ratio (vapor), and height of the freezing level, all combining to determine when and where collection of liquid drops became the dominant growth process. It was also found that the presence of large liquid drops in the initial cloud droplet distribution increased the number and mass of the hailstones. Their results showed that large liquid water contents were not necessary to produce large hail, confirming previous findings described above.

Young (1975) followed a closed parcel, containing 550 different size categories of cloud, rain, snow, and graupel particles, in a specified vertical velocity profile. Two hail suppression concepts were examined -- hail embryo competition and updraft glaciation. Seeding clouds to increase the number of hail embryos in such a way as to narrow their size spectrum proved to be an effective means of increasing embryo competition (and therefore suppressing hail) only in storms where hail grows in simple up-down trajectories. However, for more complex trajectories, the complete glaciation of embryo-forming cells adjacent to the main updraft proved more effective.

The important process of ice multiplication was included in a 1DT model, developed by Scott and Hobbs (1977), which divided liquid water, ice crystals, snow and graupel into numerous size categories. The Hallett and Mossop (1974) ice multiplication process was included to simulate the ejection of ice splinters from ice particles which grow by collecting liquid water, thereby increasing the concentration of ice crystals. The process of ice-crystal aggregation to produce snow was also modeled. Maritime and continental clouds were simulated by using the appropriate cloud condensation nuclei (CCN) spectrum.

The results showed graupel to be the predominant ice particle in the maritime cloud, comprising more than half the total ice mass (10% of the total condensate). For the continental cloud, the <u>total</u> ice mass was only 0.01% of the total condensate, with graupel greater in mass (but not in number) than the ice crystals and snow. The difference can be explained by the greater percentage of large liquid drops in the maritime cloud as a result of the maritime CCN spectrum. The freezing of these larger drops was the main source of graupel in the maritime cloud while the more time-consuming process of ice crystal conversion to graupel through riming was the main graupel-formation process in the continental cloud. Thus, the more quickly-formed graupel in the maritime cloud could begin to deplete significant amounts of liquid water sooner, thereby collecting greater mass than the equivalent graupel particles in the continental cloud. The difference in drop size distributions between the maritime and continental clouds (from the different CCN spectra) also resulted in different ice crystal concentrations, due to the drop size-dependent ice multiplication process. As the ice multiplication process was dependent on drops greater than 23 μm (of which there were more in the maritime cloud), the ice crystal concentration increased substantially with time in the maritime simulation but was relatively constant for the continental case. The splinters produced by ice multiplication provided more ice crystals for the large drops to accrete. Thus the formation of graupel by drop (contact) freezing increased substantially in the major ice multiplication region (-3 to -8°C).

Takahashi (1976) used 135 size categories for liquid drops, graupel and hail and 105 for disk-shaped ice crystals in an axisymmetric 2DT model with similar microphysics to that of Scott and Hobbs. The domain was relatively small: 2 km in radius and 6 km in height. The results indicated that ice crystal concentrations at certain levels could be increased substantially by the ice multiplication process combined with recycling. In fact, recycling of all hydrometeors occurred and was considered to be a major factor in the creation and growth of hail in hailstorms. However, it is quite likely that hydrometeor recirculation was unnaturally "forced" by both the small domain and the assumption of axisymmetry, which restricted the circulation.

2.3.2 Bulk water microphysics

As mentioned previously, the purpose of using bulk water techniques is to simplify the modeling of the microphysics in models which emphasize the dynamics. Despite the sometimes "gross" simplifications made in bulk water parameterizations, they should still yield results comparable with the findings of the more detailed microphysical studies and be consistent with observations.

Most of the bulk water techniques used to represent ice particles stem from the work of Kessler (1969). Based on the results of observations by Marshall and Palmer (1948), a simple inverse exponential size distribution was assumed for rain particles, in contrast to the many discrete size categories used by Scott and Hobbs, Takahashi, and others. Given the rain-mixing ratio at a point, all that was needed to define the distribution was the external specification of one of the distribution parameters, such as a constant slope, intercept or total number concentration, from which the others could be derived. (The Marshall-Palmer distribution is defined by a constant intercept of 0.08 cm^{-4}.) Then the "mean diameter", "mean fallspeed" and growth rates can be derived for the distribution by integrating the expressions derived for a single particle over the entire diameter range (zero to infinity). The inverse exponential function is analytically integrable and so the resulting expressions are simply functions of the distribution parameters, easily calculated given the precipitation content.

Simpson and Wiggert (1969) used this type of parameterization for rain and ice particles in a 1DL model to study latent heat effects from cloud seeding on cloud dynamics and precipitation. The precipitation was initiated by autoconversion from cloud water. Their results showed that the release of latent heat from simulated seeding increased model cloud top height and precipitation for clouds with naturally small vertical growth (6 to 7 km) whereas seeding naturally taller clouds (8 to 10 km) did not increase precipitation. Weinstein (1970) also examined seeding effects in a similar fashion to Simpson and Wiggert using a 1DT model. His results did not show an exact correspondence between increased cloud top height (due to seeding) and precipitation but rather emphasized the importance of seeding time and temperature.

Cotton (1972) assumed inverse exponential distributions for rain and graupel but used 21 classes for ice crystals of different shapes which are temperature-dependent in a parcel (1DL) model. Some of the processes included were vapor deposition, riming and raindrop freezing (both immersion and contact freezing). At sub-zero temperatures, ice saturation techniques were employed when there was no cloud water present. Seeding was simulated by simply increasing the number of ice crystals in a given class. "Seeding" maritime-type clouds resulted in a significant release of latent heat through increased contact freezing. This was found to be one of the principal causes for the increase in cloud top height in the seeded clouds.

A numerical simulation of a hailstorm was attempted by Orville and Kopp (1977), using a 2DT slab-symmetric model with a large domain of 20 km by 20 km and a grid resolution of 200 m. Five classifications of water substance were considered: water vapor, cloud water, cloud ice (crystals), rain and precipitating ice (hail). Inverse exponential distributions were assumed for rain and precipitating ice, each distribution being defined by a constant intercept and the hydrometeor content. Autoconversion of cloud and liquid water collection are rain sources while precipitating ice is initiated from raindrop freezing (based on the work of Bigg, 1953 and referred to as "Bigg's freezing") and conversion from cloud (through an approximation to the Bergeron-Findeisen process). Hail grows by the accretion of liquid water and the collection of cloud ice while sublimation and melting deplete the hail content.

Both wet and dry growth modes are simulated for the hail. One difference between the wet and dry growth modes is the collection efficiency of hail for cloud ice, assumed to be only 0.1 for dry growth but increased to 1.0 for wet growth to reflect the increased capturing capacity for ice crystals by the hailstone's liquid coat. Shedding of liquid water also occurs in the wet growth mode, the shed water being added to the rain content. The equation for wet growth is taken from Musil (1970). Glaciation was simulated by the isobaric freezing of all cloud water advected above the -35°C isotherm. Additional features of the model included evaporation, heating and cloud shadow effects.

The model managed to reproduce such observed severe storm features as a sloping updraft, gust front, shelf clouds and pedestal clouds. Other features produced in the model which agreed with observations were a precipitation cascade ("wall") and radar overhang. An important finding was the appearance of "warm buoyant bubbles" which led to a cellular storm pattern in some of the simulations.

The unexpectedly high ice particle concentrations, which varied with time, found in many maritime clouds prompted Koenig and Murray (1976) to investigate ice generation in maritime and continental clouds. Another goal of their research was to examine the effects of seeding on cloud dynamics. For these purposes, a 2D mixed Eulerian-Lagrangian axisymmetric model was used which employed bulk water microphysics. Liquid drops were modeled according to Kessler (1969) while the ice parameterization was based on the work of Koenig (1966, 1972). Ice particles were divided into two categories -- Type A ice and Type B ice. Type A ice arises from nucleation (from the vapor), a function of temperature, and consists of initially small ice crystals which begin to grow by vapor diffusion only. Type B ice arises from drop contact freezing and (initially) consists of generally larger, more spherical ice particles formed from the collision of a water drop with a Type A ice crystal. Both types of ice particles can grow by vapor diffusion and riming.

For the purpose of calculating the ice particle growth rates, the entire spectrum of ice particles in each category was represented by the mass of a "growth mean particle", defined by the ice mixing ratio and number density (both of which must be determined at each time step). Four different growth regimes are defined, depending on the "growth mean mass", each characterized by an appropriate method for computing growth due to diffusion and/or riming. Melting is simulated by assuming an "average particle radius" for the ice particles and sublimation is modeled in an analogous way to the evaporation of raindrops (Kessler). The "volume median radius" is used to calculate the representative terminal fall velocity for fallout.

Results indicated general agreement between model calculations and observations with respect to the size and quantity of liquid and ice hydrometeors. However, the increase in ice crystal concentration with time, which led to the exceptionally high crystal concentrations observed in maritime clouds, was not well captured, indicating the need for the inclusion of a time-dependent ice generation process. The inclusion of the Hallett and Mossop ice multiplication process, which generated large, time-dependent ice crystal concentrations in the maritime simulation of Scott and Hobbs mentioned above, may have improved the results in this respect. It was also concluded that "seeding" did little to affect the gross dynamic structure of small cumulonimbus clouds, i.e. the periodicity of draft development, but could, in some cases, increase cloud height (but not necessarily precipitation) in agreement with Weinstein's results.

To investigate the effects of seeding, Yau (1979b) added ice crystals to the previously-modeled cloud and rain in the Steiner-Yau 3DT cumulus cloud model. Major ice phase processes in the bulk water parameterization were nucleation from the vapor, deposition, riming, melting, fallout, and crystal aggregation into snowflakes. As this scheme is used for describing ice crystals (and snow) in the model used for this thesis, it will be described in more detail in Chapter 3. Seeded and non-seeded runs were executed (using only two dimensions) and the results were compared with observations of a seeded cloud at Yellowknife, N.W.T. The results of the numerical simulation indicated a slightly higher cloud top for the "seeded" run but a lower liquid water content than in the "natural" run. However, after 30 minutes in the "seeded" run, the melting of snowflakes ensured a steady supply of rainwater although it all evaporated before it could reach the ground. The simulated cloud compared reasonably well with the observed cloud, considering the restrictions of using only two dimensions to simulate a three-dimensional cloud. Good agreement was indicated between observed and calculated maximum vertical velocity and cloud water content while the simulated cloud top was lower than the observed top.

Stephens (1979) developed a comprehensive, yet reasonably simple, ice phase parameterization for use in a 3DT cumulus cloud model. Using bulk water techniques similar to those employed by Orville and Kopp, the initiation and growth of ice crystals and graupel was parameterized. Ice crystals were assumed to be monodispersely ~~distributed hexagonal~~ plates whereas "graupel" followed an inverse exponential distribution (with a specified number concentration rather than intercept as in Orville and Kopp's scheme). The graupel class was divided into three subclasses -- light graupel, heavy graupel and hail. The graupel parameterization was adopted for the model used in the research for this thesis and so will be described fully in Chapter 3 (the model description).

A 1DT model similar to one developed by Cotton (1975) was used to test the parameterization. Soundings from South Park, Colorado (continental) and Miami, Florida (maritime) were used to initiate the test runs. The model results indicated that the ice phase parameterization would be suitable for use in a two- or three-dimensional model but could be improved by the modification of several of the modeled processes and the addition of other ice phase processes which were considered important but were not included.

To conclude this review of past literature dealing with models, a unique, relatively simple model of warm and cold rain microphysics for use in cumulus cloud simulations, developed by Yau and Austin (1979), will be discussed. The model was a hybrid between a full stochastic scheme and a bulk water parameterization, retaining many of the advantages of each while removing some of the restrictions. Stochastic methods may be more realistic but make large computational (and storage) loads on computers. On the other hand, the assumption of inverse exponential distributions for hydrometeors used in most bulk water schemes may not be valid for many clouds. To overcome these restrictions, cloud water was treated very simply as in Kessler's bulk water parameterization while rain and graupel were partitioned into 25 size categories, allowing the development of particle size spectra. The processes included evaporation, condensation, freezing, riming, deposition (sublimation), melting and the "stochastic" processes of collection and breakup. Wet and dry growth of graupel were modeled as well.

A 1D kinematic updraft was used to compare this scheme with both stochastic and bulk water methods. Sensitivity tests were also performed to investigate autoconversion of cloud to rain, raindrop self-interaction (collection), and the inclusion of the ice phase (cloud ice and graupel). Results showed that for warm rain simulations, resulting drop-size spectra were almost identical with those obtained by the more complex and time-consuming full stochastic methods. The results were relatively insensitive to assumptions about the autoconversion process due to a counterbalancing effect between autoconversion and collection. Raindrop self-interaction proved to be a major mechanism in the development of precipitation and drop size evolution. Impaction drop breakup narrowed the drop size distribution, delaying the onset of precipitation and reducing the maximum rainfall rate. The inclusion of the ice phase gave insight into the relationship between the rate of cloud glaciation and hydrometeor growth. Rapid freezing with depletion of supercooled water can inhibit the growth of rain and graupel while a moderate freezing rate combined with a supply of supercooled water enhances the development of graupel.

The microphysical scheme described above was later incorporated by Yau (1980b) in a dynamic framework, a two-cylinder model of cumulus cells, which was applied to computing cumulus heat and mass transports.

CHAPTER 3

THE MODEL

3.1 Introduction

Steiner (1973), in a pioneering effort, developed a 3DT model of cumulus convection. The emphasis in this model was on the dynamics, and no precipitation microphysics were included. Although Steiner presented the theory of deep convection in his thesis, the simpler shallow convection equations were used in his research. In the past few years, this model has been modified by Yau (1979b, 1980a) to include

- modeling of deep convection (z = approximately 10 km)
- calculation of the basic state from a sounding
- the addition of warm rain and ice crystal/snow microphysics
- calculation of condensation and evaporation using Asai's (1965) saturation technique

Other more recent modifications include the inclusion of buoyant instability in the calculation of sub-grid-scale processes and the inclusion of vapor effects on the basic state.

The research presented in this thesis basically involved the addition of bulk water graupel microphysics to this model for the purpose of simulating a hailstorm in three dimensions.

This chapter presents the model in two sections: the first outlining the complete microphysical parameterization and the second describing the model's dynamic and numerical aspects. All equations are in c.g.s. units unless otherwise specified.

3.2 Microphysics

Bulk water microphysical techniques are used to represent cloud water, rain, ice/snow, and graupel. The sections on cloud, (warm) rain and ice crystals are largely taken from Yau (1979b, 1980a) except for the section on ice saturation thermodynamics, which is based on Stephens (1979).

The important processes included in the parameterization and their symbols are:

1. Autoconversion of cloud to rain (AC)
2. Collection of cloud by rain (CC)
3. Nucleation of individual ice crystals from the vapor (NUCLEA)
4. Riming of cloud water onto ice particles (RIM, RIMH)
5. Aggregation of ice crystals to form snowflakes
6. Vapor deposition and sublimation (DEP(H), SUB(H))
7. Conversion of ice crystals (or snow) to graupel (CONV)
8. Evaporation of liquid water (EVPC, EVPR)
9. Melting of ice particles into cloud or rain (MELT(H))
10. Rain accretion by graupel (HCOL)
11. Initiation of graupel through raindrop freezing (by both contact with ice crystals and Bigg's freezing) (CONTH, PIFR)
12. Fallout of snow, rain and graupel (FALLOUT)
13. Glaciation of cloud water at temperatures <-35°C (GLAC)

In the bulk water microphysical parameterization used here, a slightly unconventional classification system is used for the ice phase. Ice particles fall into two general classes: ice crystals/snow and graupel. Ice crystals/snow (or simply ice/snow) refers to those ice particles nucleated from the vapor or from cloud droplet freezing (glaciation) which can aggregate to form snowflakes. Graupel, following the scheme suggested by Stephens (1979), is the term used to represent the other class of ice particles which are assumed to be spherical and originate as frozen drops or ice/snow that has grown to "graupel size" by deposition and riming. Graupel is further divided into three sub-classes: light graupel, heavy graupel, and hail, for which the particle bulk densities are assumed to be 0.1, 0.6, and 0.9 g cm^{-3} respectively. Only the graupel content determines into which sub-class the graupel content falls and the particle density is set accordingly. Light graupel is further distinguished by a different fallspeed equation. In this manner, the "graupel" class incorporates both graupel and hail.

3.2.1 Cloud and rain water

Cloud water is condensed from the vapor state (COND) and evaporated (EVPC) using Asai's (1965) saturation technique which takes latent heat considerations into account. Cloud and rain are modeled following Kessler (1969). Raindrops follow a Marshall-Palmer (1948) distribution and can fall relative to the air while cloud droplets are suspended and move with the air flow.

Autoconversion of cloud to rain (AC) is used to parameterize the coalescence process for rain initiation while rain processes include accretion (CC) and evaporation (EVPR). These processes, along with the terminal fallspeed (V_r) and rainfall rate (R_r), are formulated by Kessler (1969) as

$$AC = \begin{cases} K(q_c - \frac{a'}{\rho_a}) \ , & q_c > \frac{a'}{\rho_a} \\ 0 \ , & q_c \leq \frac{a'}{\rho_a} \ , \end{cases} \tag{1}$$

$$CC = 928\ q_c(\rho_a q_r)^{7/8}\ \exp(kz/2) \tag{2}$$

$$\begin{aligned} EVPR &= 4.3(q_v - q_{vs})(\rho_a q_r)^{13/20} \quad \text{for } q_v < q_{vs} \\ &= 0 \quad \text{otherwise} \end{aligned} \tag{3}$$

$$\begin{aligned} V_r &= 2864(\rho_a q_r)^{1/8}\ \exp(kz/2) \\ R_r &= 18.35(\rho_a q_r)^{9/8}\ \ (\mathrm{mm}^{-1}\ \mathrm{hr}^{-1}) \end{aligned} \tag{4}$$

where K, the autoconversion rate constant, is $10^{-3}s^{-1}$, a', the autoconversion threshold, is 10^{-6} g cm^{-3} and k is 10^{-4} m^{-1}. The saturation mixing ratio is denoted by q_{vs} while q_v, q_c and q_r denote water vapor, cloud water and rain water contents, respectively, all in units of g g^{-1}. ρ_a is the air density in g cm^{-3}.

3.2.2 Ice crystals

3.2.2.1 Single crystals

Nucleation (NUCLEA)

Ice crystals are initiated by nucleation from the vapor following Koenig and Murray (1976). Nucleation occurs when the air is saturated with respect to water and the temperature is <0°C or when the air is saturated with respect to ice and the temperature is <-12°C. Fletcher (1969) gives the maximum number of ice nuclei per gram of air activated at a temperature T as

$$N_n = 10^{-5} \exp(0.6\Delta T) \qquad (5)$$

(where $\Delta T = T_0 - T$) giving an order of magnitude increase for every 4°C decrease in temperature.

If there are some crystals present at a point (N_i), only the excess of N_n over that number will be nucleated. The nucleated crystals are assumed to be monodisperse particles with a mass of 10^{-11} g (equivalent to an ice sphere of 3 μm radius). Thus, the change to the ice/snow mixing ratio is

$$\mathrm{NUCLEA} = 10^{-11} (N_n - N_i)/\delta t \qquad (5a)$$

Deposition and riming

These ice particles grow as individual crystals by deposition and riming until their mass reaches the "aggregation threshold" of 1.4×10^{-5} g, at which point they are assumed to aggregate to form snowflakes which are distributed exponentially.

The mass of a single crystal (m_i) is calculated using the ratio of the ice particle mixing ratio (q_i) to the maximum total number of particles per gram of air (N_n) with a lower limit of 10^{-11} g, i.e.:

$$m_i = \begin{cases} \frac{q_i}{N_n}, & \frac{q_i}{N_n} > 10^{-11} \text{ g} \\ 10^{-11} \text{ g}, & \frac{q_i}{N_n} \leq 10^{-11} \text{ g} \end{cases} \tag{6}$$

Growth by diffusion of a single crystal of mass m_i is given by Koenig (1971) as

$$\frac{dm_i}{dt} = a_1 m_i^{a_2} \left(\frac{q_v - q_{si}}{q_{vs} - q_{si}}\right) \tag{7}$$

where a_1 and a_2 are functions of temperature (tabulated by Koenig, 1971) and q_{si} is the saturation mixing ratio over ice. To get the rate of change in mixing ratio, equation (7) is multiplied by the number of ice crystals, as follows:

$$\text{DEP} = \frac{dq_i}{dt} = a_1 m_i^{a_2} \left(\frac{q_v - q_{si}}{q_{vs} - q_{si}}\right) N_i \tag{8}$$

The riming rate for a single crystal is

$$\frac{dm_i}{dt} = \frac{\pi D_m^2}{4} V_i(D_m) E_i \rho_a q_c$$

and (9)

$$\text{RIM} = \frac{dq_i}{dt} = \frac{\pi D_m^2}{4} V_i(D_m) N_i E_i \rho_a q_c$$

where D_m is the melted diameter (calculated from the mass of an ice crystal and assuming a bulk density of 0.5 g cm^{-3}), V_i is the crystal terminal fallspeed taken from Langleben (1954), and E_i is the assumed collection efficiency of 1.0.

3.2.2.2 Crystal aggregates (snow)

If the calculated crystal mass m_i is larger than the aggregation threshold (1.4×10^{-5} g), the crystal content is assumed to be exponentially distributed according to

$$N_i(D_m) = N_{oi} e^{-\lambda_i D_m} \tag{10}$$

where the intercept N_{oi} and the slope λ_i can be related to the snow content $(\rho_a q_i)$ by using a relationship between snowfall rate R_i and content given by Sekhon and Srivastava (1970) as

$$\rho_a q_i = 2.07 \times 10^{-3} R_i^{\,0.86} \tag{11}$$

It turns out that, in c.g.s. units,

$$\begin{aligned} N_{oi} &= 2.45 \times 10^{-9}(\rho_a q_i)^{-1.09} \\ \lambda_i &= 9.4 \;\; \times 10^{-3}(\rho_a q_i)^{-0.522} \end{aligned} \tag{12}$$

Deposition and riming

The deposition/sublimation and riming rates for the (exponential) spectrum are derived by simply integrating equations (8) and (9) over the entire diameter range (0 to ∞). This gives

$$\mathrm{DEP} = a_1\left(\frac{\pi}{6}\rho_w\right)^{a_2} \frac{N_{oi}\;\Gamma(3a_2+1)}{\rho_a\;\lambda_i{}^{3a_2+1}} \left(\frac{q_v-q_{si}}{q_{vs}-q_{si}}\right) \tag{13}$$

$$\mathrm{RIM} = \left(\frac{\pi}{4}a\right)\left(\frac{\rho_w}{\rho_i}\right)^{2/3} \frac{N_{oi}\;\Gamma(3+b)}{\lambda_i{}^{3+b}}\,\overline{E}_i q_c \tag{14}$$

where ρ_w is the density of water, a and b are constants in the expression for the terminal fallspeed of the ice particles, ρ_i is the density of ice and $\overline{E}_i$ the mean collection efficiency of the ice particle spectrum for cloud water.

Fallspeed

The terminal fallspeed for both ice crystals and snow is given by

$$V_i(D_{oi}) = a\, D_{oi}^{\,b} \qquad (\mathrm{cm\ s^{-1}}) \qquad (15)$$
$$= 207\, D_{oi}^{\,0.31}$$

where D_{oi}, the median volume diameter, is related to the ice content by

$$D_{oi} = 390(\rho_a q_i)^{0.525} \qquad (16)$$

Melting

When the temperature is higher than 0°C, the entire ice crystal/snowflake content is melted instantaneously into either cloud droplets or raindrops, depending on the median volume diameter D_{oi}. If $D_{oi} < 200\ \mu m$ (the conventional borderline diameter between cloud drops and raindrops), then the ice is melted into cloud. Otherwise, the rain category receives the melted ice.

$$\mathrm{MELT} = \frac{q_i}{\delta t} \qquad (17)$$

and the changes of cloud (δq_c) or rain (δq_r) in a time step are

$$\delta q_c = q_i\ ,\quad D_{oi} < 200\ \mu m \qquad (18)$$
$$\delta q_r = q_i\ ,\quad D_{oi} \geq 200\ \mu m$$

Ice saturation thermodynamics

If the temperature is below -35°C at a certain point, then all the cloud water advected into this point is isobarically frozen and the ice/

snow, water vapor, and temperature are isobarically adjusted to ice saturation using a process similar to the one employed by Stephens (1979). All operations on the graupel and rain content are suspended except for advection and diffusion.

3.2.3 Graupel

The graupel parameterization described here is essentially the one suggested by Stephens (1979). It has been modified slightly by including heterogeneous (Bigg) raindrop freezing, as described by Orville and Kopp (1977), as another source of graupel.

Some other minor modifications will be mentioned in the appropriate sections.

This particular parameterization was chosen for its simplicity, comprehensiveness and appropriateness for a 3D model. This scheme, compatible with the microphysics in the existing model, is by no means perfect -- several important ice phase processes were not included to keep the parameterization relatively simple -- but represents a starting point or foundation for future work on 3D simulations of storms.

Detailed derivations of the following equations will not be presented as, for the most part, they can be found in Stephens (1979) or in other references (cited).

3.2.3.1 Distribution of graupel

Graupel particles are assumed to follow an inverse exponential distribution, which represents well the averaged graupel size distribution from observations as given in Jones (1959), Musil et al (1978), Federer and Waldvogel (1975), Douglas (1964) and current (unpublished) results of the

Alberta Hail Studies (ALHAS) project. Thus, the graupel size distribution is given by

$$N(D) = N_{og}e^{-\lambda D} \tag{19}$$

where N(D) is the number concentration of graupel particles per diameter (D) increment, N_{og} is the intercept, and λ the slope.

By integration over the entire size (D) spectrum (0 to ∞) we have the following relations for the slope parameters

$$\lambda = \left(\frac{\pi \rho_g N_{tg}}{\rho_a q_g}\right)^{1/3} \tag{20}$$

$$N_{og} = N_{tg}\lambda \tag{21}$$

where ρ_g is the graupel density, N_{tg} the total number concentration of graupel particles, ρ_a the air density and q_g the graupel mixing ratio. N_{tg} is an externally specified constant. Thus, given the graupel content ($\rho_a q_g$), all the slope parameters are defined.

Other investigations have set other parameters constant, such as Manton and Cotton (1977), who used a constant slope, λ (for rain), and Orville and Kopp (1977), who defined N_{og} to be constant (for rain and graupel). Stephens explains why a constant N_{tg} was chosen to define the graupel distribution in the scheme used here. A constant slope implies a balance between coalescence/accretion and breakup, appropriate for raindrops but not graupel. A constant intercept, N_{og}, gave rise to exceedingly high melting rates for graupel in the simulations done by Orville and Kopp. By fixing N_{tg}, this problem is alleviated slightly but not eliminated. Another alternative would be to carry the total number concentration, i.e. recalculate it at each time step (as done by Koenig and Murray, 1976), but this would increase the complexity of the scheme as well as execution time.

The problem of choosing an appropriate value for the total number concentration N_{tg} is also discussed by Stephens. The value of N_{tg} should correspond to observations. Data taken from the field (using impact platforms) indicate total concentrations of graupel of between 10^{-8} and 10^{-4} cm^{-3} (Douglas, 1964; Federer and Waldvogel, 1975; Musil et al, 1978). Low values of N_{tg} imply a graupel content composed of large hailstones in low total concentration while higher values imply the existence of many more, smaller graupel particles. Stephens modeled the latter category of particles by choosing a "high" value of 10^{-4} cm^{-3} for N_{tg} and that is the value used here.

Given the graupel content and the value of N_{tg}, the mean diameter $\overline{D}$ and the mean mass $\overline{m}$ can be computed as

$$\begin{aligned}\overline{D} &= \frac{1}{N_{tg}} \int_0^{\infty} D\, N(D)\, dD \\ &= \frac{1}{\lambda} = \frac{1}{(\pi \rho_g N_{tg}/\rho_a q_g)^{1/3}}\end{aligned} \tag{22}$$

$$\begin{aligned}\overline{m} &= \frac{1}{N_{tg}} \int_0^{\infty} m_g(D)\, N(D)\, dD \\ &= \frac{\rho_a q_g}{N_{tg}}\end{aligned} \tag{23}$$

Note that both the mean diameter $\overline{D}$ and mean mass $\overline{m}$ are directly proportional to the graupel content $(\rho_a q_g)$ and inversely proportional to the total number concentration N_{tg}. The mean mass is only used to determine into which subclass (light graupel, heavy graupel, or hail) the graupel content falls.

3.2.3.2 Types of graupel: density and terminal velocity

As mentioned previously, graupel can fall into one of three subclasses depending on the mean mass: light graupel, heavy graupel, or hail. Each type of particle is characterized by a different density and terminal velocity as outlined in the following table.

For graupel mean mass $\overline{m}$ (g)	Type of graupel	Assigned density ρ_g (g cm^{-3})	Terminal velocity (cm s^{-1}) $V_g(D)$
$<10^{-3}$	light graupel	0.1	$594.(p_{00}/p)^{1/2}D^{1/2}$
$10^{-3}<\overline{m}<2\text{x}10^{-2}$	heavy graupel	0.6	$(4\rho_g\, g/3\rho_a C_D)^{1/2}D^{1/2}$
$>2\text{x}10^{-2}$	hail	0.9	

The terminal velocities used to advect the graupel distribution are mass weighted and have the form

$$\overline{V}_g = \frac{\Gamma(4.5)}{6} V_g(\overline{D})$$

where

$$V_g(\overline{D}) = \begin{cases} 594.(p_{00}/p)^{1/2}\overline{D}^{1/2} & \text{(light graupel)} \\ (4\rho_g\, g/3\rho_a C_D)^{1/2}\overline{D}^{\,1/2} & \text{(heavy graupel or hail)} \end{cases} \qquad (24)$$

The mean diameter $\overline{D}$ is calculated using (22). The drag coefficient C_D is given a value of 0.6.

3.2.3.3 The graupel processes

To calculate the various growth and transformation processes which are dependent on the size of the individual particles concerned using a continuous exponential distribution (N(D)), the following technique is employed. First, the time rate of change to the mass of an individual particle is formulated ($\frac{dm}{dt}$). This expression is then integrated over the whole size range (0 to ∞) to give the rate of change of the particle "bulk" content ($\rho_a q$) as follows:

$$\frac{d(\rho_a q)}{dt} = \int_0^\infty \frac{dm}{dt} N(D)\, dD \qquad (25)$$

where q represents the rain, snow, or graupel mixing ratio and m is the mass of a single drop or ice particle.

When describing the rates below, formulated after equation (25), only the expression for the time rate of change to the mass of an individual particle $\frac{dm}{dt}$ and the final derived expression for the time rate of change to the graupel mixing ratio $\frac{dq_g}{dt}$ will be given. The detailed intervening steps in the derivation can be found in Stephens (1979) unless otherwise indicated.

Raindrop contact freezing (CONTH)

This is the freezing of supercooled raindrops upon collision with an ice crystal or snowflake which acts as a freezing nucleant. If the rain distribution is given by an exponential distribution with constant intercept N_{or},

$$N_r(D_r) = N_{or} e^{-\lambda_r D_r} \qquad (26)$$

where, in an analogous fashion to graupel,

$$\lambda_r = \left(\frac{\pi \rho_w N_{or}}{\rho_a q_r}\right)^{1/4} \tag{27}$$

$$N_{or} = N_{tr}\lambda_r = 0.1 \text{ cm}^{-4}$$

$$\overline{D}_r = 1/\lambda_r$$

then it can be shown that the rate of contact freezing is

$$\text{CONTH} = \pi N_i \overline{D}_r^{\,2} \left| 6.1875\, \overline{V}_r - 5V_i(D_{oi}) \right| q_r \tag{28}$$

where N_i is the total number of ice crystals present at that point, $\overline{D}_r$ is the mean raindrop radius defined above (27), $V_i(D_{oi})$ is the ice crystal/snow "median volume diameter" fallspeed defined in (15) and the rain mass weighted terminal velocity $\overline{V}_r$ is given by

$$\overline{V}_r = \frac{\Gamma(4.5)}{6} (4\rho_w g/3\rho_a C_D)^{1/2} \overline{D}_r^{\,1/2} \tag{29}$$

Heterogeneous raindrop freezing (Bigg's freezing) (PIFR)

The expression for the rate of raindrop freezing is based on the work of Bigg (1953) and is explained in Wisner et al (1972). This process is included in the model of Orville and Kopp (1977) but omitted in Stephens' (1979) scheme.

$$\text{PIFR} = 20\pi^2 B' N_{or}(\rho_w/\rho_a)(\exp[A'(T_0 - T)] - 1)\lambda_r^{-7} \tag{30}$$

where A' and B' are parameters in the Bigg freezing process determined from lab experiments and T_0 is the freezing temperature (273K).

Conversion from ice crystals/snow (CONV)

Conversion of snow crystals which have grown to "graupel size" through vapor deposition and riming is handled in a simpler, yet perhaps less realistic, fashion than Stephens used, for the sake of simplicity, and should probably be modified in the future.

Stephens calculated the conversion rate using both consideration of the riming rate and a crystal mass upper limit. The riming rate is used to reflect the fact that graupel is usually initiated from ice crystals which have grown mainly by riming cloud water rather than vapor deposition (thus creating non-crystalline ice particles). At the same time it is possible for crystals and crystal aggregates to grow by both deposition and riming to sizes beyond which mass and terminal velocity versus diameter relations are no longer valid. In the latter case, a crystal "mass upper limit" was set by Stephens and used to determine when the appropriate portion of the ice crystal content should be transferred into graupel, regardless of the means of crystal growth.

To simplify the formulation of this process, the entire ice crystal/snow content at a point is transferred to graupel when the ice/snow volume diameter D_{oi} (equation (16)) exceeds an externally specified conversion threshold diameter. The threshold diameter chosen was 800 µm (0.8 mm). Thus

$$\mathrm{CONV} = \begin{cases} q_i/\delta t \ , & D_{oi} \geq 0.08 \text{ cm} \\ 0 \ , & D_{oi} < 0.08 \text{ cm} \end{cases} \qquad (31)$$

Deposition/sublimation (DEPH/SUBH)

The time rate of change of a graupel particle mass m_g due to vapor deposition is

$$\frac{dm_g}{dt} = 2\pi D \, SS \, G(T,p) \, f(Re) \qquad (32)$$

where SS is the supersaturation with respect to ice

$$SS = q_v/q_{si} - 1 \qquad (33)$$

G(T,p) is a function of temperature and pressure

$$\begin{aligned} G(T,p) &= \left[\frac{\varepsilon L_{vi}^2}{K' R_a T^2} + \frac{R_a T}{\varepsilon \psi(T,p) e_{si}(T)}\right]^{-1} \\ \psi(T,p) &= 828\left(\frac{T}{p}\right)\left(\frac{393}{T+120}\right)\left(\frac{T}{273}\right)^{3/2} \qquad (34) \\ e_{si}(T) &= p q_{si}(T)/\varepsilon \end{aligned}$$

and f(Re) is the ventilation factor, a function of the Reynolds number Re

$$\begin{aligned} f(Re) &= 1 + 0.229\,(Re)^{1/2} \qquad (35) \\ Re &= \rho_a D V_g/\mu(T) \end{aligned}$$

where $\mu(T)$ is the dynamic viscosity of air at temperature T. Equation (32) is based on the electrostatic analogue of capacitance to describe the vapor field around the graupel particle with heat and mass balance considerations.

The deposition/sublimation rate of change to the graupel mixing ratio is then given by

$$DEPH/SUBH = 2\pi \, SS \, N_{tg} \, \bar{D} \, G(T,p) \, f(Re)_g/\rho_a \qquad (36)$$

where $f(Re)_g$ is a special ventilation function for graupel given by

$$f(Re)_g = 1 + 0.265\,(\rho_a \overline{D}\,\overline{V}_g/\mu(T))^{1/2} \qquad (37)$$

Deposition occurs for SS > 1 while sublimation occurs if SS < 1.

Riming (RIMH)

The time rate of change of mass due to riming of cloud water is

$$\frac{dm_g}{dt} = \frac{\pi}{4}D^2\, V_g(D)\, E_{gr}(\rho_a q_c) \qquad (38)$$

where E_{gr} is the efficiency of riming, here assumed to be 1.0. The final form, giving the time rate of change to the graupel mixing ratio, becomes

$$RIMH = \frac{3}{7}\pi N_{tg}\,\overline{V}_g\,\overline{D}^2\, q_c \qquad (39)$$

Collection of rain water (HCOL)

The time rate of change of mass m_g of a graupel particle falling through exponentially distributed rain is

$$\frac{dm_g}{dt} = \int_{D_r=0}^{\infty} \frac{\pi}{4}(D+D_r)^2\,|\,V_r(D_r) - V_g(D)\,|\,\frac{\pi}{6}D_r^{\,3}\rho_w\, E(D_r\backslash D)\, N_r(D_r)\, dD_r \qquad (40)$$

where the collection/coalescence efficiency $E(D_r\backslash D)$ is assumed to be 1.0. The derived transfer rate for the collection of a rain distribution by a graupel distribution is then

$$HCOL = \pi\,|\,\overline{V}_r-\overline{V}_g\,|\, q_r\, N_{tg}(0.5\overline{D}^2 + 2\overline{D}_r\overline{D} + 5\overline{D}_r^{\,2}) \qquad (41)$$

Melting (MELTH)

Consideration of sensible heat flux to a graupel particle from the environment and the heat released from vapor condensation onto the particle leads to the expression for the time rate of change of mass due to melting (Mason, 1956) when T > 0°C.

$$\frac{dm_g}{dt} = -\frac{1}{L_{li}}\left[2\pi DK'(T-T_{sfc}) + 2\pi DL_{vi}\,\psi(T,p)(\rho_v-\rho_{vsfc})\right]\left[(1+0.226\,Re^{1/2})\right] \quad (42)$$

where T_{sfc} and ρ_{vsfc} are the temperature and vapor density, respectively, at the surface of the graupel particle. The final bracketed term is a ventilation factor, a function of the Reynolds number.

Integrating (42) over the entire graupel distribution gives the decrease to the graupel content due to melting, as

$$MELTH = \frac{1}{L_{li}}\left[2\pi K'(T-T_0)/\rho_a + 2\pi L_{vi}\,\psi(T,p)(q_v-q_{vs})\right]\bar{D}\,N_{tg}\,f(Re)_g \quad (43)$$

where it has been assumed that the temperature of the particle's surface is 0°C (T_0) and the surface water vapor density is liquid water saturated (q_{vs}).

An additional term for the transfer of sensible heat to the graupel from accreted water, included in Stephens' expression, is considered to make a relatively small contribution to the total rate and so is omitted. It should also be noted that when the air is subsaturated with respect to water, the condensation term containing (q_v-q_{vs}) is set to zero.

3.2.4 Radar reflectivity

The equivalent radar reflectivities are computed according to Kessler (1969).

For rain we simply have

$$Z_e^r = \int_0^\infty N_{or} e^{-\lambda_r D_r} D_r^6 \, dD \tag{44}$$
$$= 720 \, N_{or} \, \lambda_r^{-7} \times 10^{12} \quad (mm^6 \, m^{-3})$$

For dry graupel particles we assume Rayleigh scattering (Smith *et al*, 1975).

$$Z_e^g = \frac{|K|^2 ice}{|K|^2 water} \int_0^\infty N_{og} e^{-\lambda D} D^6 \, dD \tag{45}$$
$$= 0.19(720 \, N_{og} \, \lambda^{-7}) \times 10^{12} \quad (mm^6 \, m^{-3})$$
or $$= 0.19(720 \, N_{tg} \, \lambda^{-6}) \times 10^{12} \quad (mm^6 \, m^{-3})$$

where $|K|_{ice}$ and $|K|_{water}$ are the dialectric constants for ice and water respectively.

Conversion to dBz units is as follows:

$$Z_e(dBz) = 10 \log_{10} [Z_e(mm^6 \, m^{-3})] \tag{46}$$

As a result of the assumptions inherent in using an exponential distribution to describe the rain and graupel contents, the calculated reflectivities tend to overestimate actual observed values (see Smith *et al*, 1975).

3.2.5 Ice processes not included

Several ice processes included in other ice phase parameterizations were not included in the scheme used in this model, mainly because they added further complications, did not readily fit into the existing microphysical framework, or because they were deemed the least important of the many ice phase processes that were considered. Some of the processes can be added quite easily while others would demand more work to incorporate them in the model.

3.2.5.1 Ice multiplication

An important process, studied by Hallett and Mossop (1974), is ice multiplication, the ejection of small ice splinters from riming ice particles. These splinters can be an important additional source of graupel through riming and by acting as nucleants for contact freezing of raindrops. This process can increase the number concentration of ice particles substantially, as shown by Takahashi (1976), Scott and Hobbs (1977) and Koenig (1977). It is for this reason that ice multiplication cannot be modeled in the present scheme, as the total number concentration of ice particles is not carried as a variable but is either an externally specified constant (for graupel) or is temperature-dependent (ice crystals). In the future, this process should be incorporated into the model in some way.

3.2.5.2 Wet growth of graupel, accretion of ice crystals and shedding

Wet growth of graupel, described by Musil (1970) and included in such models as Orville and Kopp's (1977), is not included in the scheme but can be added with little difficulty at a later time. In the wet growth mode, the collected water coat on a graupel particle is not completely frozen and some is shed, usually assumed to be shed as raindrops and so is added to the rain distribution. For dry growth, the graupel particles are inefficient collectors of ice crystals (Orville and Kopp use an equation similar to (38) to describe crystal collection but with a low collection/coalescence efficiency of 0.1) but the liquid water coat accreted in the wet growth mode improves the collection efficiency considerably so that it can be assumed to be 1.0. However, wet growth typically occurs between the 0°C and -15°C isotherms, where the relatively small ice crystal content would not add significant mass to the graupel content. Thus, as wet growth is not modeled, shedding and accretion of ice crystals are not included as well.

3.2.6 Summary of microphysical parameterization

Water is divided into five major categories: vapor, cloud water, ice crystals/snow, rain, and graupel. Snow, rain and graupel are assumed to follow inverse exponential distributions and are allowed to precipitate. The various interactions between the five categories of water are illustrated in Figure 1, while Table 1 summarizes the various transfer rates and other expressions used in this parameterization.

Figure 2 shows a flow chart representing the way graupel is classified (i.e. light graupel, heavy graupel or hail) according to the graupel content. The graupel content at a grid point can be initiated by several processes: raindrop freezing, conversion from ice/snow crystals, advection, or diffusion. Once graupel exists at a grid point, the mean mass ($\overline{m}$) of the distribution is calculated. The mean mass then determines which type of graupel is appropriate for the given content. If the mean mass is below 10^{-3} grams, the graupel distribution is assumed to be made up of small, light graupel particles of low density (0.1 g cm^{-3}) with a specially calculated appropriate terminal velocity. If the mean mass falls between 10^{-3} grams and 2×10^{-2} grams, then the classification "heavy graupel" is used, which assumes a particle density of 0.6 g cm^{-3}. If the mean mass is greater than 2×10^{-2}

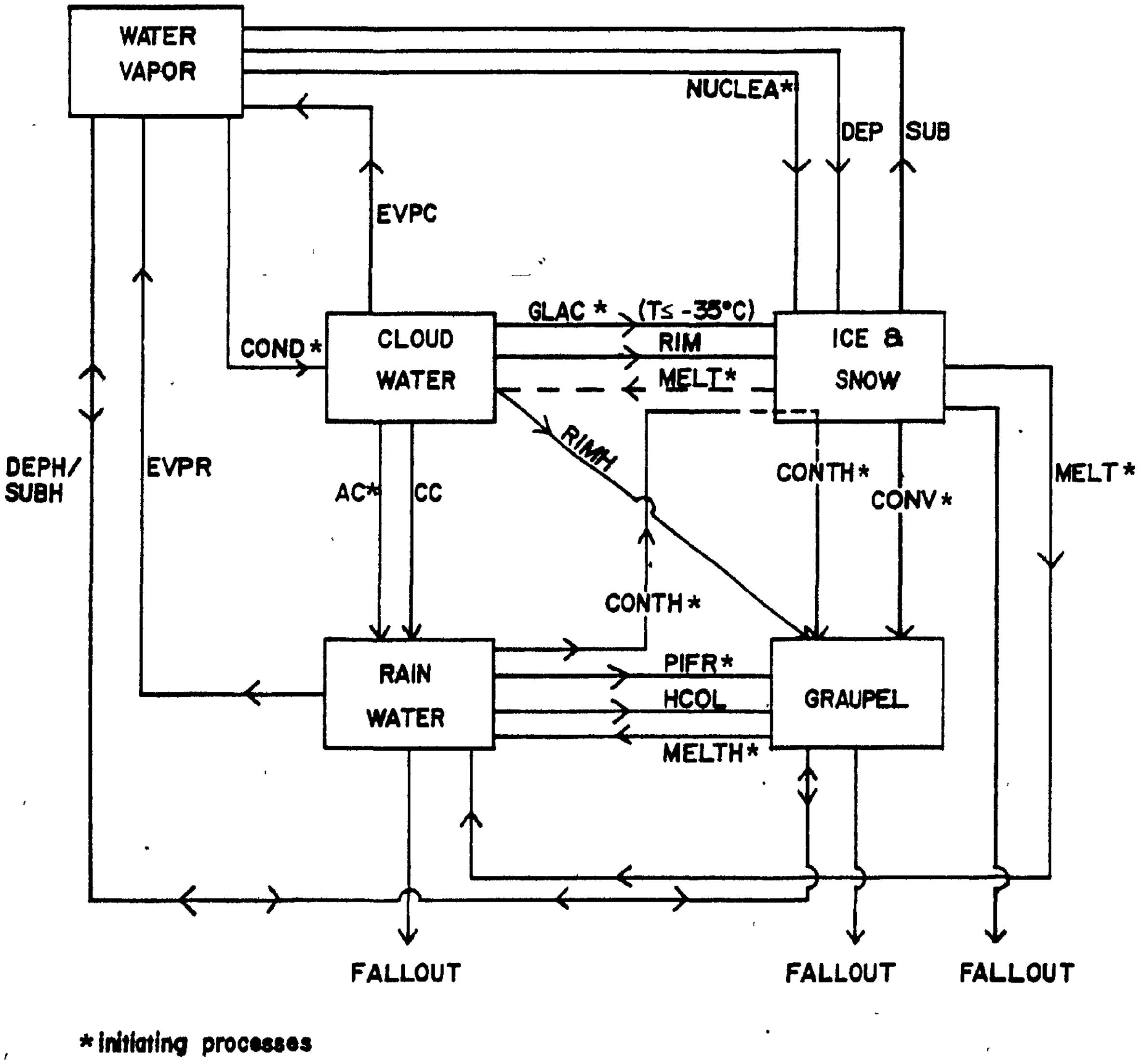

Figure 1. The microphysical processes. An asterisk (*) indicates an initiating process. The two lines (one dashed) labeled MELT* indicate that ice/snow can melt into either cloud or rain. The process names are explained in the List of Symbols.

Table 1

Symbol	Microphysical Process or Parameter	Formulation
COND	Condensation	$a(q_v-q_{vs})\left[1+\frac{L_{vl}^2\,q_{vs}}{C_pR_v\,(\pi_p\theta)^2}\right]^{-1}$
AC	Autoconversion of cloud to rain	$\begin{cases} K\,(q_c-\frac{a}{\rho_a}), & q_c>\frac{a}{\rho_a} \\ 0 & \text{otherwise} \end{cases}$
CC	Accretion of cloud by rain	$928\,q_c\,(\rho_a q_r)^{7/8}e^{kz/2}$
EVPC	Evaporation of cloud	same as COND with $q_v < q_{vs}$
EVPR	Evaporation of rain	$4.3(q_v-q_{vs})(\rho_a q_r)^{13/20}$
V_r	Fallspeed of rain	$2864(\rho_a q_r)^{1/8}e^{kz/2}$
R_r	Rainfall rate (mm hr^{-1})	$18.35(\rho_a q_r)^{9/8}$
NUCLEA	Nucleation	$10^{-11}(N_n-N_i)/\delta t$
DEP	Deposition (ice crystal)	$a_1 m_i^{a_2}\,(\frac{q_v-q_{si}}{q_{vs}-q_{si}})\,N_i$
RIM	Riming (ice crystal)	$\frac{\pi D_m^2}{4}\,V_i(D_m)\,N_i\,E_i\,\rho_a q_c$
DEP	Deposition (snow)	$a_1(\frac{\pi}{6}\rho_w)^{a_2}\,\frac{N_{oi}\,\Gamma(3a_2+1)}{\rho_a\,\lambda_i^{3a_2+1}}\,(\frac{q_v-q_{si}}{q_{vs}-q_{si}})$
RIM	Riming (snow)	$(\frac{\pi}{4}a)(\frac{\rho_w}{\rho_i})^{2/3}\,\frac{N_{oi}\,\Gamma(3+b)}{\lambda_i^{3+b}}\,\bar{E}_i q_c$
$V_i(D_{oi})$	Fallspeed of ice/snow	$a\,D_{oi}^{\,b} = 207\,D_{oi}^{\,0.31}$
MELT	Melting of ice/snow	$q_i/\delta t$
$\bar{V}_g$	Mass weighted fallspeed of graupel	$\frac{\Gamma(4.5)}{6}\begin{cases} 594.(p_{00}/p)^{1/2}\,\bar{D}^{1/2} & \text{(light graupel} \\ \text{or} & \\ (4\rho_g\,g/3\rho_a C_D)^{1/2}\,\bar{D}^{1/2} & \text{(otherwise)} \end{cases}$

Table 1 (continued)

Symbol	Microphysical Process or Parameter	Formulation
CONTH	Contact freezing	$\pi N_i \overline{D}_r^{2} \; 6.1875 \lvert \overline{V}_r - 5V_i(D_{oi}) \rvert \; q_r$
$\overline{V}_r$	Mass weighted fallspeed of rain	$\frac{\Gamma(4.5)}{6} (4\rho_w \, g/3\rho_a C_D)^{1/2} \, \overline{D}_r^{1/2}$
PIFR	Bigg's freezing	$20 \pi^2 B' N_{or} (\rho_w/\rho_a) (e^{A'(T_0-T)} - 1) \lambda_r^{-7}$
CONV	Conversion of snow to graupel	$\begin{cases} q_i/\delta t \,, & D_{oi} \geq 0.08 \text{ cm} \\ 0 \,, & D_{oi} < 0.08 \text{ cm} \end{cases}$
DEPH/ SUBH	Deposition/sublimation for graupel	$2\pi SS \, N_{tg} \overline{D} \, G(T,p) \, f(Re)_g/\rho_a$
RIMH	Riming for graupel	$\frac{3}{7} \pi N_{tg} \overline{V}_g \overline{D}^2 q_c$
HCOL	Collection of rain by graupel	$\pi \lvert \overline{V}_r - \overline{V}_g \rvert \, q_r \, N_{tg} (0.5\overline{D}^2 + 2\overline{D}_r \overline{D} + 5\overline{D}_r^{2})$
MELTH	Melting of graupel	$\frac{1}{L_{li}} [2\pi K'(T-T_0)/\rho_a + 2\pi L_{vi} \psi(T,p)(q_v - q_{vs})] \times \overline{D} N_{tg} f(Re)_g$
Z_e^r	Equivalent radar reflectivity for rain ($mm^6 \, m^{-3}$)	$720 \, N_{or} \lambda_r^{-7} \times 10^{12}$
Z_e^g	Equivalent radar reflectivity for graupel ($mm^6 \, m^{-3}$)	$0.19(720 \, N_{tg} \lambda^{-6}) \times 10^{12}$

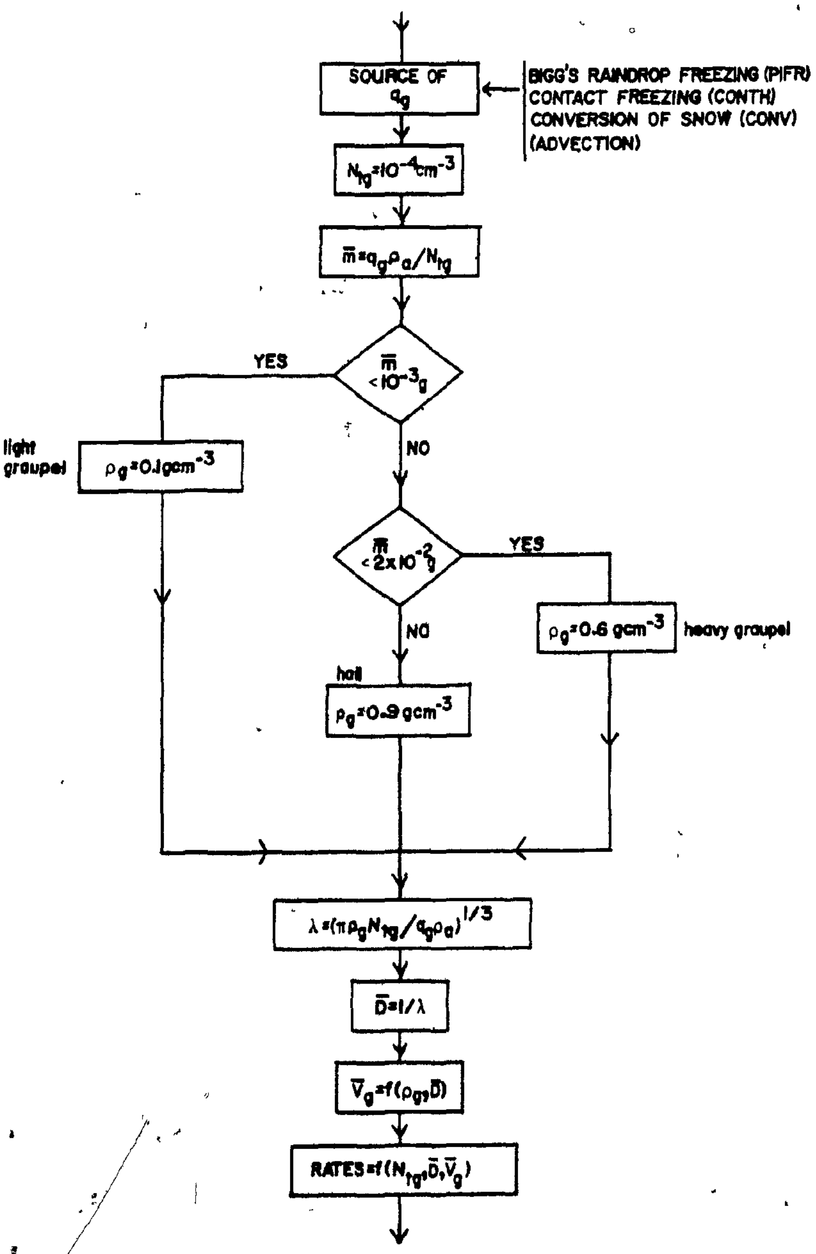

Figure 2. A flow chart showing the method of graupel classification.

grams, the density is increased to 0.9 g cm^{-3} to model "heavier" hailstones. Once the type of graupel has been determined, the slope parameters are then defined using the appropriate particle density along with the graupel content. The various rates and parameters used to determine the growth of the graupel distribution are then calculated for a given time step and the whole procedure is repeated for each grid point and time step when graupel is present.

3.3 Dynamics, thermodynamics and numerical aspects of the model

This section deals with dynamical and numerical aspects of the Steiner (1973)-Yau (1979b, 1980a) 3D model of cumulus convection used for this study taken, for the most part, from Yau (1980a). The equations are developed for variables averaged over an elemental grid volume. Details can be found in Steiner (1973) and the symbols, which are generally standard, can be found in the List of Symbols at the beginning of this thesis.

3.3.1 Major assumptions

1) Coriolis force and surface friction are neglected
2) The domain is assumed to be surrounded by identical domains
3) The deep anelastic system of equations is used

3.3.2 Equations of motion

Dimensionless pressure π_p and the potential temperature θ are expressed using perturbation methods (i.e. sums of their basic state values ($\Pi(z)$, $\Theta(z)$)) and deviations from that state (π_p', θ'). The equation of motion expressed in tensor form is

$$\frac{\partial u_i}{\partial t} = -\frac{1}{\rho_a}\frac{\partial}{\partial x_j}(\rho_a\, u_i\, u_j) - C_p\theta\frac{\partial \pi'}{\partial x_i}p + F_i \qquad (47)$$

$$-\delta_{i3} < -\frac{1}{\rho_a}\frac{\partial}{\partial x_j}(\rho_a\, u_i\, u_j) - C_p\theta\frac{\partial \pi'}{\partial x_i}p + F_i > + \delta_{i3}\,(B - < B >)$$

where F_i represents the sub-grid-scale processes and B, the buoyancy, is given by

$$B = g\left(\frac{\theta'}{\theta} + 0.61\, q_v' - q_c - q_r - q_i - q_g\right) \qquad (48)$$

where q_v' is the deviation of water vapor mixing ratio from basic state (q_v).

The angle braces (< >) denote the horizontal mean of the expression inside the braces.

3.3.3 Continuity equations for air and water substances

For deep convection, the continuity equation for air is

$$\frac{\partial}{\partial x_i}(\rho_a u_i) = 0 \qquad (49)$$

while the prognostic continuity equations for vapor (q_v), cloud (q_c), rain (q_r), ice/snow (q_i), and graupel (q_g) are:

$$\frac{\partial q_v}{\partial t} = -\frac{1}{\rho_a}\frac{\partial}{\partial x_j}(\rho_a\, u_j\, q_v) + \mathrm{DIFFU} - \mathrm{COND} + \mathrm{EVPC} + \mathrm{EVPR} - \mathrm{DEP} - \mathrm{DEPH} +$$
$$\mathrm{SUB} + \mathrm{SUBH} - \mathrm{NUCLEA}$$

$$\frac{\partial q_c}{\partial t} = -\frac{1}{\rho_a}\frac{\partial}{\partial x_j}(\rho_a\, u_j\, q_c) + \mathrm{DIFFU} + \mathrm{COND} - \mathrm{AC} - \mathrm{CC} - \mathrm{EVPC} - \mathrm{RIM} -$$
$$\mathrm{RIMH}\ (+\ \mathrm{MELT}) - \mathrm{GLAC}$$

$$\frac{\partial q_r}{\partial t} = -\frac{1}{\rho_a}\frac{\partial}{\partial x_j}\left[\rho_a(u_j - \overline{V}_r\delta_{13})q_r\right] + \mathrm{DIFFU} + \mathrm{AC} + \mathrm{CC} + \mathrm{MELTH} - \mathrm{EVPR} -$$
$$\mathrm{HCOL} - \mathrm{CONTH}\ (+\ \mathrm{MELT}) - \mathrm{PIFR} - \mathrm{FALLOUT} \qquad (50)$$

(50) continued

$$\frac{\partial q_i}{\partial t} = -\frac{1}{\rho_a}\frac{\partial}{\partial x_j}[\rho_a(u_j - V_i\delta_{i3})q_i] + \mathrm{DIFFU} + \mathrm{NUCLEA} + \mathrm{DEP} + \mathrm{RIM} + \mathrm{GLAC} - \mathrm{MELT} - \mathrm{SUB} - \mathrm{CONV} - \mathrm{FALLOUT}$$

$$\frac{\partial q_g}{\partial t} = -\frac{1}{\rho_a}\frac{\partial}{\partial x_j}[\rho_a(u_j - \overline{V}_g\delta_{i3})q_g] + \mathrm{DIFFU} + \mathrm{CONV} + \mathrm{HCOL} + \mathrm{CONTH} + \mathrm{DEPH} + \mathrm{RIMH} + \mathrm{PIFR} - \mathrm{MELTH} - \mathrm{SUBH} - \mathrm{FALLOUT}$$

where the first term is advection (ADVEC) and the second is diffusion (DIFFU) of a quantity q, given by

$$\mathrm{DIFFU} = \frac{1}{\rho_a}\frac{\partial}{\partial x_j}(\rho_a \nu_h \frac{\partial q}{\partial x_j}) \qquad (51)$$

The parentheses around MELT reflect the fact that the ice/snow is melted either into cloud or into rain, but not both.

3.3.4 Diagnostic pressure equation

From (47), the diagnostic pressure equation can be derived:

$$C_p \frac{\partial}{\partial x_i}(\rho_a \Theta \frac{\partial \Pi''}{\partial x_i}) = \frac{\partial}{\partial x_i}[-\frac{\partial}{\partial x_j}(\rho_a u_i u_j) + \rho_a F_i - \delta_{i3} < -\frac{\partial}{\partial x_j}(\rho_a u_i u_j) + \rho_a F_i >] + \frac{\partial}{\partial x_3}\rho_a(B - < B >) - \frac{\partial}{\partial t}(\frac{\partial \rho_a u_i}{\partial x_i}) \qquad (52)$$

where

$$\Pi'' = \pi_p' - < \pi_p' >$$

3.3.5 Sub-grid-scale processes

The turbulence parameterization follows that of Deardorff (1970, 1972), modified to include thermal instability effects as in Hill (1974). The term for F_i, sub-grid-scale forces, is

$$F_i = \frac{1}{\rho_a} \frac{\partial}{\partial x_j} \left[\rho_a \nu_m \left(\frac{\partial u_i}{\partial x_j} + \frac{\partial u_j}{\partial x_j} \right) \right] \tag{53}$$

where ν_m, the eddy coefficient for velocity components, has the form

$$\nu_m = k' \Delta^2 \left(t_s^{-1} + t_b^{-1} \right) \tag{54}$$

and is related to the eddy coefficient for scalar quantities ν_h by the Prandtl number ν_h/ν_m, set to 1. In equation (54) t_s and t_b represent the deformation and buoyant time scales respectively, while k' is a constant and $\Delta = (\Delta x \, \Delta y \, \Delta z)^{1/3}$ is the grid spacing scale.

The deformation time scale is proportional to the velocity deformation and is formulated by Deardorff (1972) as

$$t_s = \left\{ \left(\frac{\partial u_i}{\partial x_j} - \left< \frac{\partial u_i}{\partial x_j} \right> \right) \left(\frac{\partial u_i}{\partial x_j} + \frac{\partial u_j}{\partial x_i} - \left< \frac{\partial u_i}{\partial x_j} + \frac{\partial u_j}{\partial x_i} \right> \right) \right\}^{-1/2} \tag{55}$$

while the buoyancy time scale, representing the local thermal instability, is given by Hill as

$$\begin{aligned} t_b &= \left| - \frac{g}{\theta} \left(\frac{\partial \theta}{\partial z} - \left. \frac{\partial \theta}{\partial z} \right|_{\text{moist}} \right) \right|^{-1/2} , & \left(\frac{\partial \theta}{\partial z} - \left. \frac{\partial \theta}{\partial z} \right|_{\text{moist}} \right) < 0 \\ &= 0 , & \left(\frac{\partial \theta}{\partial z} - \left. \frac{\partial \theta}{\partial z} \right|_{\text{moist}} \right) \geq 0 \end{aligned} \tag{56}$$

where the moist adiabat $\left. \frac{\partial \theta}{\partial z} \right|_{\text{moist}}$ is calculated in saturated regions but set to 0 in subsaturated regions.

3.3.6 Thermodynamic equation

The change in the potential temperature perturbation with time is

$$\frac{\partial \theta'}{\partial t} = - \frac{1}{\rho_a} \frac{\partial}{\partial x_j} (\rho_a u_j \theta') + \mathrm{DIFFU} + \frac{L_{vl}}{C_p \pi_p} [\mathrm{COND} - \mathrm{EVPC} - \mathrm{EVPR}]$$
$$+ \frac{L_{vi}}{C_p \pi_p} [\mathrm{NUCLEA} + \mathrm{DEPC} + \mathrm{DEPH} - \mathrm{SUB} - \mathrm{SUBH}] \qquad (57)$$
$$+ \frac{L_{li}}{C_p \pi_p} [\mathrm{GLAC} + \mathrm{RIM} + \mathrm{RIMH} + \mathrm{PIFR} + \mathrm{HCOL} + \mathrm{CONTH} - \mathrm{MELT} - \mathrm{MELTH}]$$

where DIFFU is given by (51) with q replaced by θ'.

3.3.7 Numerical procedure

3.3.7.1 Grid system

The three-dimensional domain is divided into 32 x 32 x 24 grid boxes with a resolution of $\Delta x = \Delta y = 1$ km and $\Delta z = 0.5$ km, giving a domain size of 32 x 32 x 12 km in the x, y, and z directions.

The wind velocity components are computed at the faces of a grid cube and the other variables at its center, making it a "staggered grid". Each domain is surrounded by identical domains for boundary condition considerations.

3.3.7.2 Finite difference methods

A second-order, non-diffusive, leapfrog method in time and a centered-difference method in space are used to solve the prognostic equations. A fast Fourier transform technique is employed to solve the diagnostic pressure equation (52). The time step δt can either be set constant or it can vary internally according to linear stability criteria and varies between 8 and 15 seconds for the simulation presented here.

A time filtering technique by Asselin (1972) is used to prevent the splitting of solutions at even and odd time steps. Negative water contents, arising from advective truncation errors, are set to zero and the excess water substance added by this process is then subtracted from each grid cell in proportion to the amount present.

3.3.7.3 Initial and boundary conditions

Vertical boundaries are rigid and free-slip. Vertical gradients of any quantity Q must vanish while the vertical velocity component (w) must be zero at the top and bottom boundaries.

$$\left.\begin{aligned} w &= 0 \\ \frac{\partial Q}{\partial z} &= 0 \end{aligned}\right\} z = 0, H \tag{58}$$

The lateral boundary conditions are assumed periodic.

The basic state temperature, water vapor, and wind profiles are given by a real sounding (Chisholm, 1970) taken close to the time and place of the observed hailstorm (near Penhold, Alberta) that is to be simulated. This data is presented in the next chapter, which deals with the observed storm of June 27, 1967.

Convection is initiated by a saturated humidity impulse at the center of the domain. The impulse is parabolic, 9 km in width, and extends from approximately 1.25 km to 3.75 km in the z direction.

The model is written in PL1 and consists of 24 subroutines. It has been used (in various versions) at McGill University, Montreal to study evaporation, water load and wind shear (Yau, 1980a), cloud seeding (Yau, 1979b), and random surface heating as a means of initialization (Michaud, 1980). Turpeinen and Yau (1981) have compared the results from 3D warm cloud simulations with GATE radar data, finding a fair degree of realism in the simulations.

CHAPTER 4

DESCRIPTION OF OBSERVED HAILSTORM

4.1 Introduction

The hailstorm which will be used for comparison with the modeled storm occurred southwest of Penhold, Alberta on June 27, 1967 and was detailed by Chisholm (1970) in his radar study of Alberta hailstorms. It was chosen basically for numerical reasons because it was the weakest, smallest storm, existing in a weakly sheared environment with little wind relative to the storm motion. Yet, this storm produced pea- and grape-sized hail at the surface. Its low energy and relatively small vertical extent implied comparatively small vertical velocities. Thus, the model vertical velocities were expected to be of comparable magnitude ensuring numerical stability for larger time steps (the internally varied time step is a function of the maximum velocity magnitude and can become quite small for large velocities, consuming vast amounts of computer time). The small size of the storm and the weak relative flow permitted the model domain to be relatively small with a reasonable resolution. The reports of large hailstones at the surface indicated the strong activity of the ice phase processes in this particular storm. Thus, this storm seemed a good example for comparison with the simulation.

An ALHAS narrow-beam 10 cm radar located in Penhold, Alberta, and specially-equipped airplanes, were used to observe the storm on this day. The storm was cellular in nature and occurred in mid- to late afternoon, from 1538 to 1813 M.S.T. The track of the storm, which formed and decayed within radar range, is shown in Figure 3. The third cell produced the largest hail at the surface and is the only one detailed by Chisholm. Thus, this cell (Cell 3) will be used for comparison purposes. The storm moved generally southeast at approximately 7 m s^{-1}, each cell lasting roughly 30 to 45 minutes. Each new cell formed on the right-hand (south) flank of the preceding, dying cell.

4.2 Atmospheric conditions

The atmospheric conditions at the time of the storm, given by a radiosonde sounding and wind hodograph, are used to initialize the model. The soundings were taken at Penhold, approximately 70 km from the storm, at 1617 M.S.T. (during the time of formation of the storm) and may be said to be representative for the storm area.

The radiosonde sounding is shown in Figure 4 and is typical of a continental, early summer air mass. The surface air is quite dry (35% relative humidity) and warm (21°C) and above is almost dry adiabatic up to 600 mb. There is a small inversion at about 720 mb and a stable layer from 600 mb to 550 mb. The relative humidity (rh) peaks at a value of 98% at the bottom of this stable layer. The lifting condensation level (LCL) and a "loaded moist adiabatic" (LMA) parcel trajectory are indicated showing a small "positive area" and a relatively low cloud top (at about 7 km),

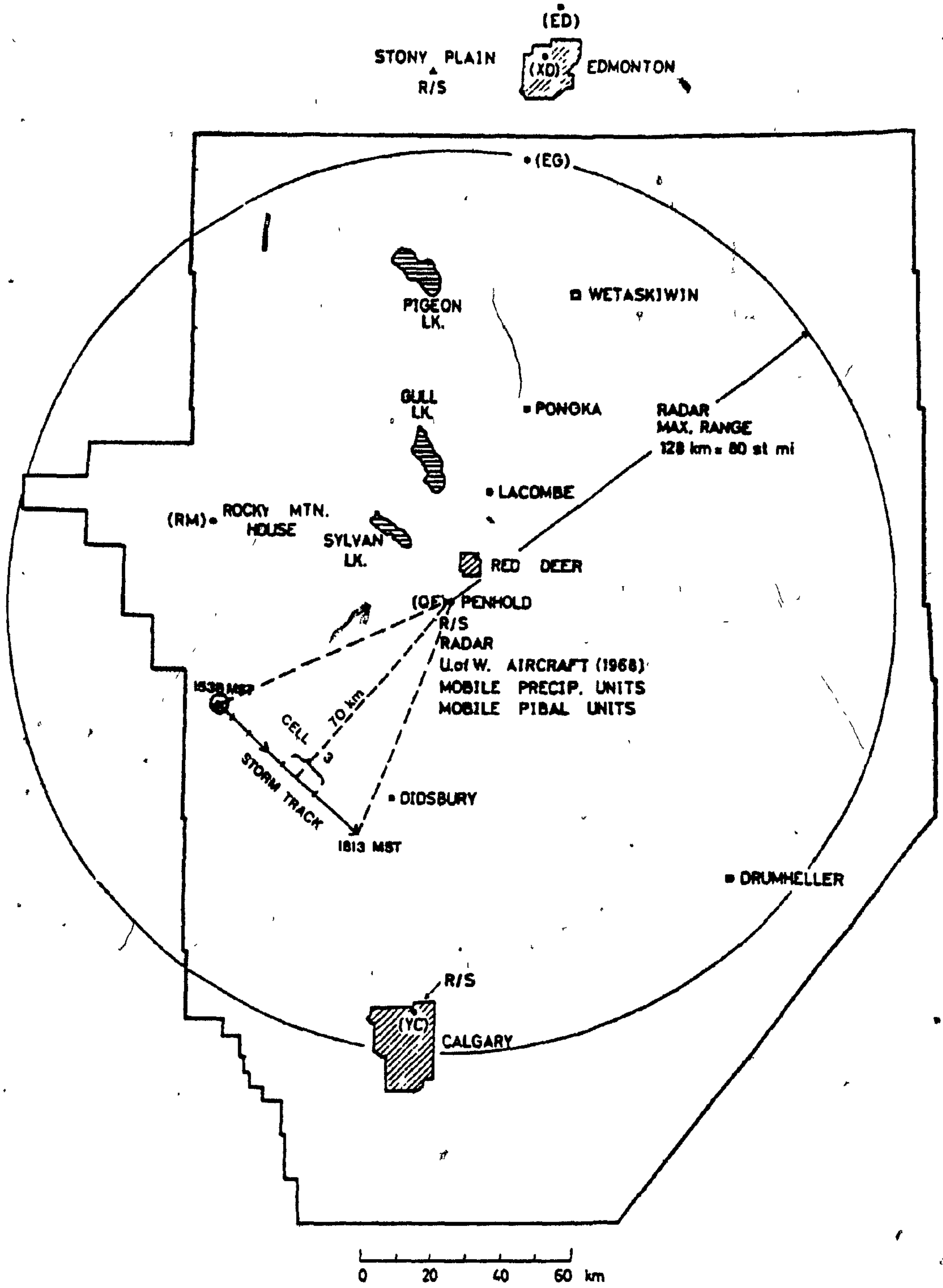

Figure 3. Map of Alberta Hail Studies (ALHAS) Project Area taken from Chisholm (1970), with the track of the observed storm of 27 June, 1967 added. Times at the beginning and end of the multicell storm are in Mountain Standard Time (M.S.T.). Note that the storm was well within radar range.

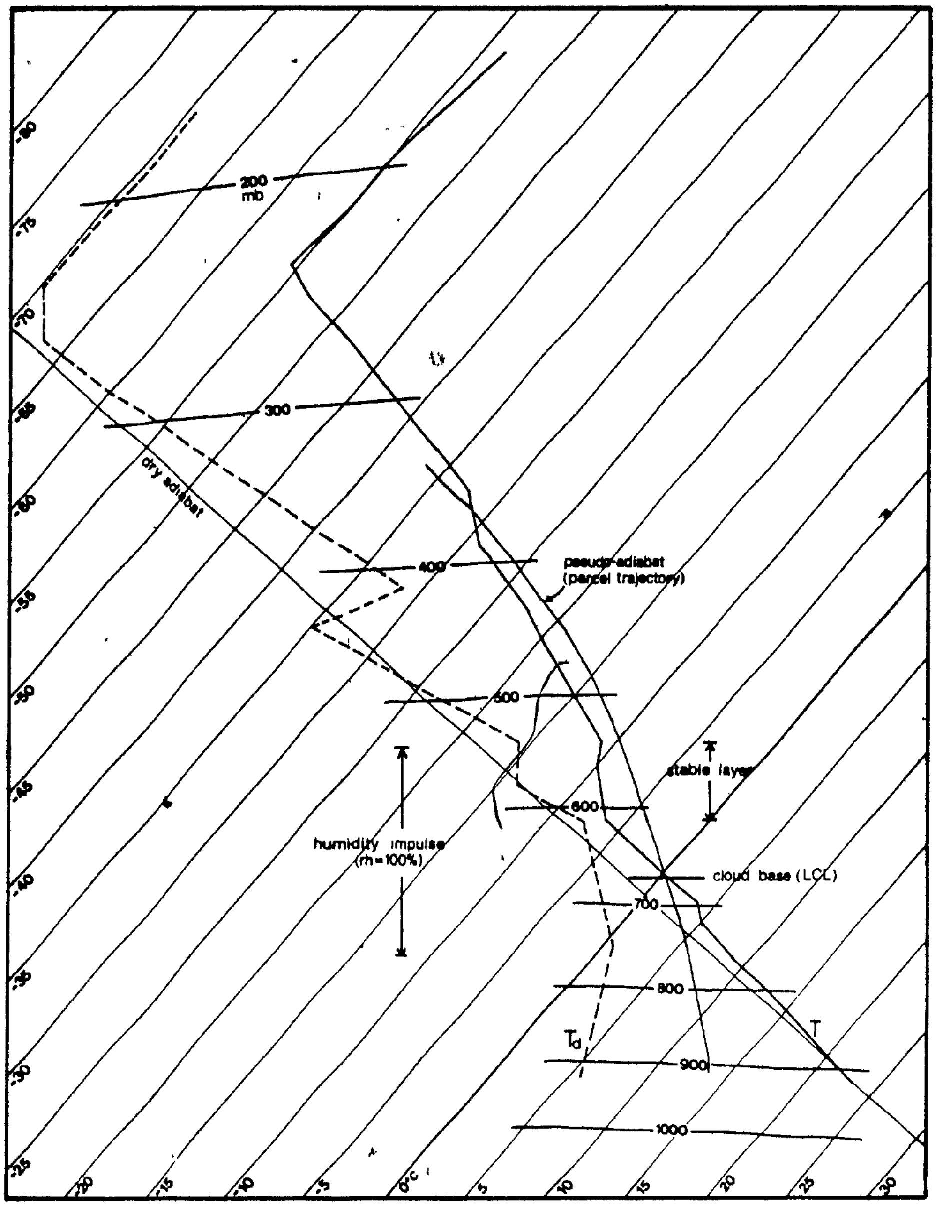

Figure 4. Sounding at 1617 M.S.T. -- 27 June, 1967 for Penhold. Indicated are a dry adiabat (for reference) and a pseudo-adiabat indicating a moist adiabatic parcel trajectory using cloud base conditions. Note the relatively small positive area and low (predicted) cloud top at about -32°C (7 km). Also shown is the vertical extent of the humidity impulse used to initiate convection in the model. (Based on Fig. 5.11 in Chisholm, 1970.)

indicative of a weak storm with weak updrafts. Observed maximum updrafts at cloud base were 5-6 m s^{-1} and no measurements were taken inside the cloud. However, Chisholm used an LMA model to predict maximum updrafts of 16.4 m s^{-1}, quite weak in comparison to the "medium" and "high" energy storms presented in his thesis. Due to uncertain and missing upper air data above 350 mb in the sounding presented by Chisholm (Figure 5.1.1 in his 1970 thesis), a sounding from Edmonton, 206 km away from the storm, was used to give the temperature profile above this level. The wind profile in the vertical is given in Figure 5 and shows a weakly sheared, ill-defined structure with a maximum horizontal velocity of 16 m s^{-1} at 3 km height. The wind flow relative to the storm, assuming a southeast storm motion of 7.4 m s^{-1}, is given in Figure 6 and is resolved into a component in the plane of storm motion and a component normal to the plane of motion shown in Figure 8. These components were used to initialize the u and v wind components, respectively, for the simulation.

4.3 Main features of storm (Cell 3: 1658 to 1731 M.S.T.)

Figure 7 shows the growing stage of cell 3 (1659 M.S.T.) in both vertical and horizontal (PPI) radar cross-sections. The vertical sections are taken along the lines indicated (on the PPI sections), one in the direction of storm motion, the other normal to the storm motion. A small notch-shaped UWER (unbounded weak echo region) is evident at 1 and 2 degree elevation. The cloud base is at 2 km above ground level (AGL) and at 3°C and some light precipitation has started to fall at the surface. Note the remaining precipitation from the dissipating stage of cell 2 on the left-hand flank of cell 3, most evident in Figures 7a and 7c. Maximum radar reflectivities in excess of 65 dBz are located at approximately 4.5 km and

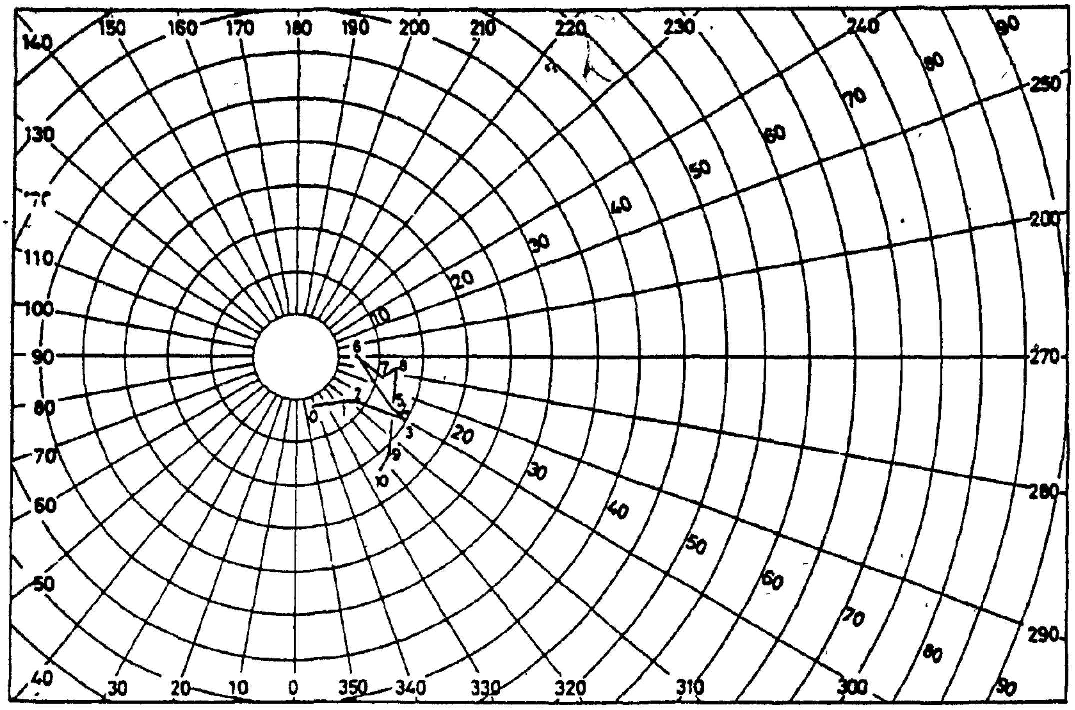

Figure 5. Wind hodograph at 1617 M.S.T. -- 27 June, 1967. Wind speeds are plotted in m s^{-1} and heights are indicated in km AGL (above ground level). From Chisholm (1970).

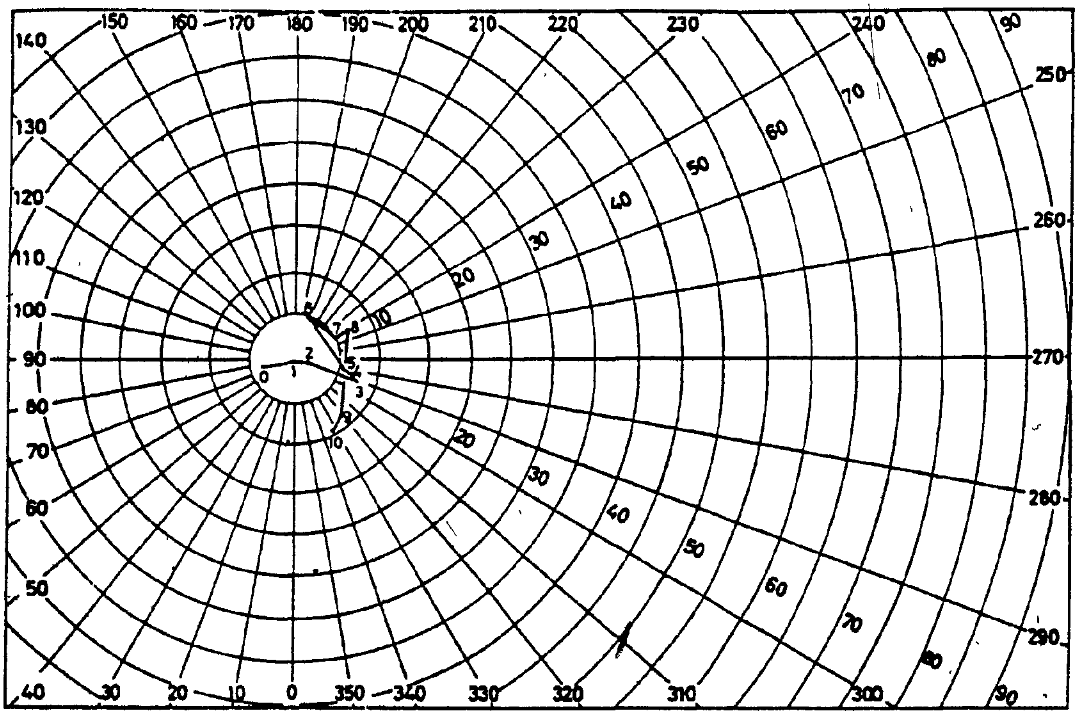

Figure 6. Same as Figure 5, but with wind speeds plotted relative to the storm (storm velocity 311 deg/7.4 m s^{-1}).

a

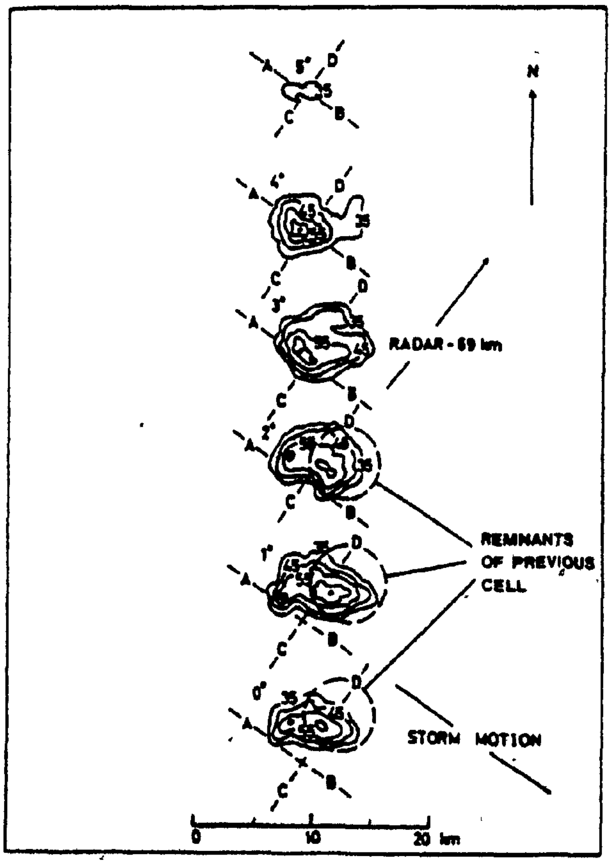

b

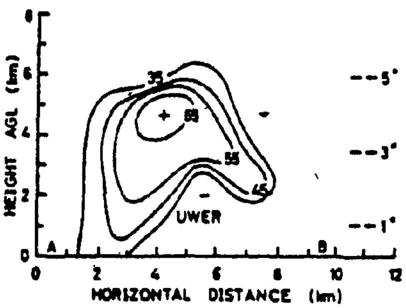

c

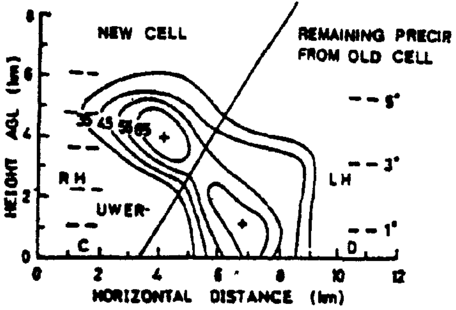

Figure 7a. PPI sections at 1659 M.S.T. -- 27 June, 1967. (Growing stage.) Contours of Z_e (equivalent radar reflectivity) are labeled in dBz. Note the remnants of the previous cell as indicated. Lines AB and CD indicate cross-section axes for Figures 7b and c. (From Chisholm, 1970.)

Figure 7b. Vertical cross-section in the direction of motion at 1659 M.S.T.-- 27 June, 1967. Contours of Z_e are labeled in dBz. Note the UWER and overhang. (From Chisholm, 1970.)

Figure 7c. Vertical cross-section normal to the direction of motion at 1659 M.S.T. -- 27 June, 1967. Contours of Z_e are labeled in dBz. Note the remaining precipitation from the previous cell on the LH side. (From Chisholm, 1970.)

a

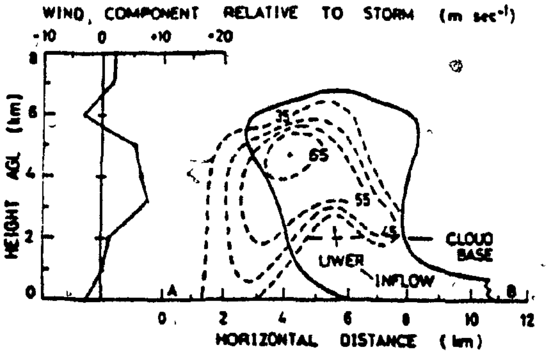

b

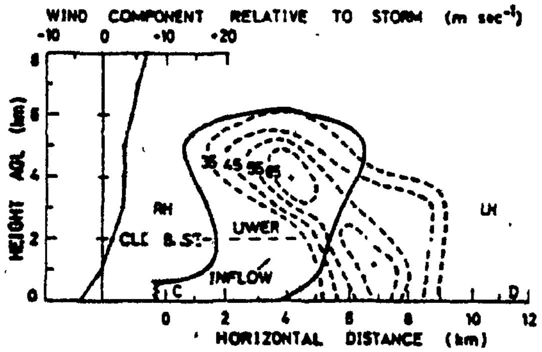

Figure 8a. Schematic airflow (deduced by Chisholm) in the plane of storm motion at 1659 M.S.T. Also shown are the wind components relative to the storm in this plane (derived from Figure 6) used to give the initial u velocity component for the model. Note the mid-level "jet" between 2 and 5 km height. The schematic airflow, over which the vertical radar cross-section of Figure 7b is superimposed, is deduced from the wind components in this plane, aircraft-measured updrafts at cloud base, and Chisholm's WER hypothesis. (From Chisholm, 1970.)

Figure 8b. Schematic airflow (deduced by Chisholm) normal to the plane of storm motion at 1659 M.S.T. Also shown are the wind components relative to the storm in this plane (derived from Figure 6) used to give the initial v velocity component for the model. The schematic airflow, over which the vertical cross-section of Figure 7c is superimposed, is deduced from the wind components in this plane, aircraft-measured updrafts at cloud base, and Chisholm's WER hypothesis. (From Chisholm, 1970.)

the "storm top", defined as the maximum height of the 35 dBz contour, is 6.5 km and rising. A derived initial airflow, using sub-cloud winds, cloud base updrafts (measured by aircraft), the weak echo region (WER) hypothesis, radar reflectivity, and mid- to high-level winds, is superimposed on the vertical cross-sections in Figure 8. (Recalling from Chapter 2, the WER hypothesis assumes that a weak echo region is composed of freshly formed minute cloud droplets in the region of the maximum sub-cloud updraft.) This figure shows a low-level inflow from the south and a relatively vertical updraft with little or no outflow.

Nine minutes later (1708 M.S.T.), cell 3 (now separate) is in its mature stage and is shown in Figure 9. The storm top has reached its maximum height (7.5 km AGL) and maximum radar reflectivities in excess of 65 dBz have extended to the surface with corresponding reports of grape-sized hail (2.0 cm in diameter). Maximum reflectivities can be found at about 2.5 km height and are estimated to be between 65 and 79 dBz. Note the large, elliptical precipitation area at the surface and the verticality of the storm. Also note the strong reflectivity gradient on the rear (upwind) side and right-hand flank (RH) of the storm, due to the inflow of air at these sides, and the relatively weak gradient on the opposite sides. The vertical section in the direction of motion (Figure 9b) shows the strongest gradient on the left (rear) side of the storm at 3 to 4 km height corresponding to the maximum inflow at this level (see Figure 8a) and the hydrometeor motion in response to this flow. This same flow creates the radar "overhang" at 1.5 km height on the opposite or front side of the storm by advecting hydrometeors over the sub-cloud inflow/updraft from the right (front) where the heavier particles can fall into this inflow region

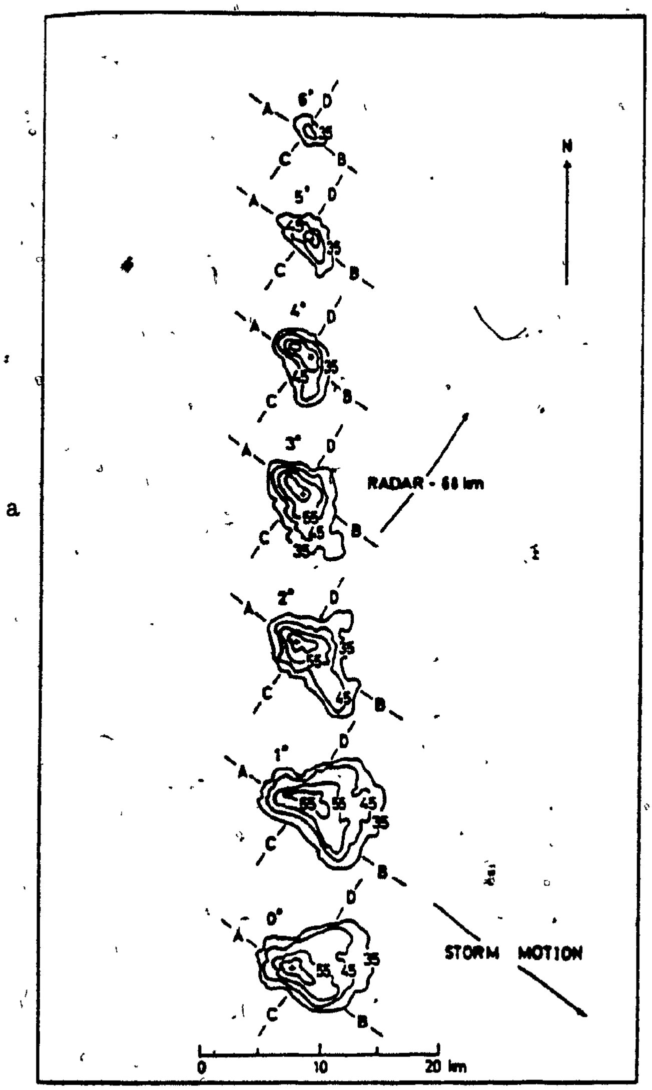

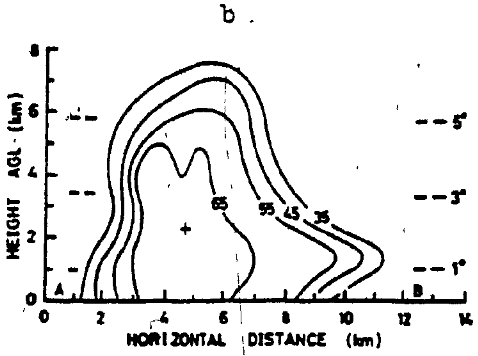

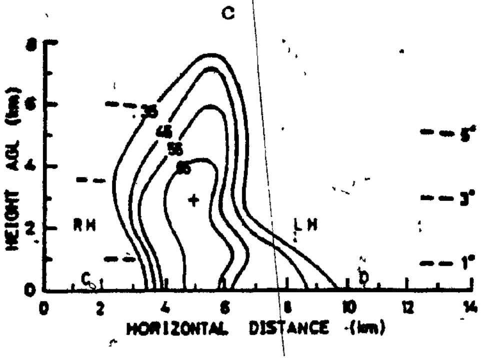

Figure 9a. PPI sections at 1708 M.S.T. -- 27 June, 1967. (Mature stage.) Contours of Z_e are labeled in dBz. Lines AB and CD indicate cross-section axes for Figures 9b and c. (From Chisholm, 1970.)

Figure 9b. Vertical cross-section in the direction of motion at 1708 M.S.T. -- 27 June, 1967. Contours of Z_e are labeled in dBz. Note the overhang on the right-hand side. (From Chisholm, 1970.)

Figure 9c. Vertical cross-section normal to the direction of motion at 1708 M.S.T. -- 27 June, 1967. Contours of Z_e are labeled in dBz. Note that the storm in this plane is narrower and lacks a substantial overhang. (From Chisholm, 1970.)

and either fall to the ground or be recycled back into the updraft core, depending on their size.

The cross-section normal to the storm motion (Figure 9c) shows areas of high reflectivity gradient at the RH flank near the surface and on the left-hand (LH) flank above 2.5 km corresponding to regions of inflow at these levels in this plane. The maximum dimensions of the storm are approximately 10 km in the direction of motion and 7 km in the normal direction.

By 1722 M.S.T., 23 minutes after the birth of cell 3, dissipation has begun. The storm top has subsided to 5 km AGL as illustrated by Figure 10 and the top of the 65 dBz contour has descended to only 1 km above the surface indicating the end of precipitation formation and growth in the cloud above. The high surface reflectivities are indicative of the last heavy downpour or precipitation gush associated with the decay of the storm. Note the still essentially elliptical shape of the surface precipitation area with a bulge in the northeast direction. The major axis lies in the direction of motion of the storm.

In summary, the storm chosen for comparison purposes was a relatively small, vertical cell which produced grape-sized hail, embedded in a continental air mass in central Alberta. The cell existed in a weakly sheared environment, its resultant verticality allowing precipitation to fall through the updraft, which ultimately brought about its decay after 23 minutes. By using the atmospheric conditions at the time of the storm to initialize the 3D Steiner-Yau cumulus cloud model, modified to include graupel, it was hoped that a similar storm could be generated numerically. In the next chapter, the results of a full 3D simulation will be presented

a

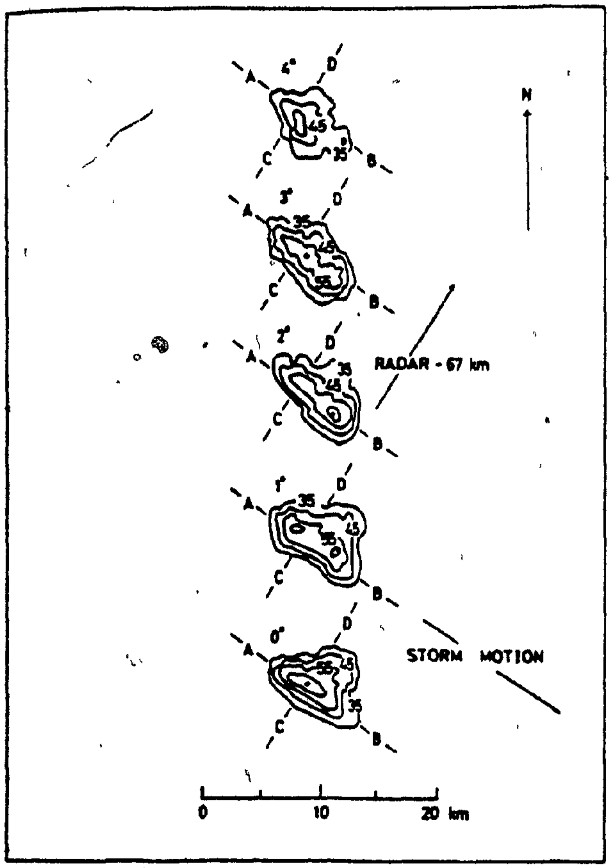

b

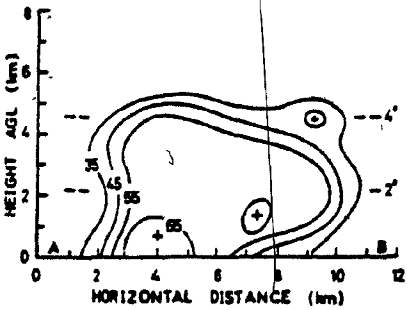

c

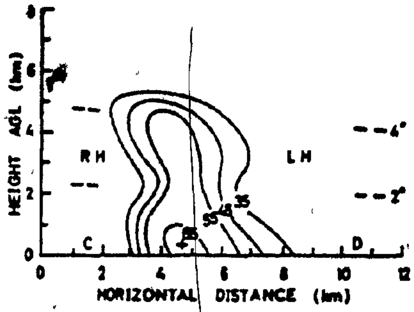

Figure 10a. PPI sections at 1722 M.S.T. -- 27 June, 1967. (Dissipating stage.) Contours of Z_e are labeled in dBz. Lines AB and CD indicate cross-section axes for Figures 10b and c. (From Chisholm, 1970.)

Figure 10b. Vertical cross-section in the direction of motion at 1722 M.S.T. -- 27 June, 1967. Contours of Z_e are labeled in dBz. Note the collapse of the region of high reflectivity ($Z_e > 65$ dBz) towards the surface. (From Chisholm, 1970.)

Figure 10c. Vertical cross-section normal to the direction of motion at 1722 M.S.T. -- 27 June, 1967. Contours of Z_e are labeled in dBz. Note the narrower, "pinched" structure in this plane. (From Chisholm, 1970.)

and in Chapter 6 the results will be discussed and compared with those from the observed storm outlined in this chapter and from a 2D test run. Particular emphasis will be placed on the comparable features such as radar structure, precipitation size and type, and airflow.

CHAPTER 5

RESULTS

5.1 Introduction

In this chapter, the results of a fully three-dimensional numerical hailstorm simulation with complete ice-phase microphysics are presented. Given an initial basic state from the sounding of June 27, 1967 at Penhold, Alberta (Figures 4 and 8), convection is initiated by using a parabolic humidity impulse and the following fields are obtained at fixed time intervals for the duration of the run (53 minutes simulated time): potential temperature perturbation θ', pressure perturbation π_p', vapor q_v, cloud q_c, rain q_r, ice/snow q_1, graupel q_g, combined rain and graupel (total) radar reflectivity Z_e, turbulent diffusion (eddy) coefficient ν_m, and buoyancy B. Horizontal and vertical velocity components are combined to give vector flow fields. Both horizontal x-y slices and vertical x-z (W-E), y-z (N-S) sections are presented, as illustrated in Figure 11. The vertical sections are taken in the plane containing the updraft maximum while several horizontal sections at different levels are displayed. Note that vertical radar sections used by Chisholm in presenting the observed storm (Chapter 4) run parallel (line AB) and perpendicular (line CD) to the storm motion

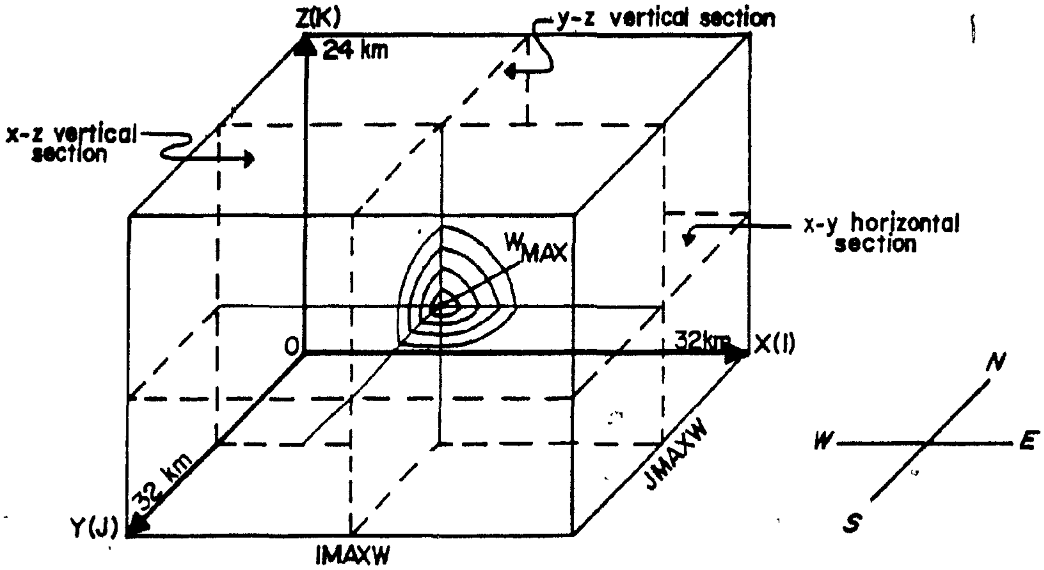

Figure 11. Three-dimensional model domain. The vertical (x-z, y-z) sections are taken in the plane containing w_{max} (which is located at the point (IMAXW, JMAXW, KMAXW)).

(i.e. NW-SE and SW-NE), whereas the corresponding model vertical sections run W-E and N-S. Also note that, in Chisholm's CD sections, the left-hand side (C) corresponds to south with distance increasing to the north, while in the corresponding model (y-z) section, north is to the left and south is to the right, with distance increasing in the south direction. The sections are of equivalent orientation if one of them is reversed. Three representative times are presented in detail: 21, 31, and 46 minutes, corresponding to the three stages of the observed storm described by Chisholm (growing (or "cumulus" stage), mature, and dissipating, respectively). Occasionally another time will be used to illustrate an important feature most evident at that time. For each of the three times, the following are displayed:

(i) cloud, rain, ice/snow, and graupel mixing ratio fields (x-z vertical section only). All fields (except the rain) are contoured as follows: the outermost contour represents a mixing ratio of 0.01 g kg^{-1}; the other inner contours start at 0.5 g kg^{-1} and increase in intervals of 0.5 g kg^{-1} in an inward direction. Where possible, maximum values are indicated by a plus sign (+). For graupel, it is indicated if the maximum content corresponds to light graupel, heavy graupel or hail. For rain content, only the outermost and innermost contour (surrounding the rain maximum) are shown. Ice/snow arising from nucleation is indicated simply by an asterisk placed on the point where ice or snow content is present. These asterisks represent small ice contents of not more than 0.2 g kg^{-1}. Ice contents larger than this are generally converted into graupel. Rain, graupel, and ice/snow content arising from frozen cloud water (above -35°C isotherm), are contoured and shaded as indicated in the diagram key. Note that horizontal and vertical axes are of different scales corresponding to the higher resolution in the vertical. Also, the closest grid points to the surface (0 km) are 0.25 km <u>above</u> the surface. Thus, in the following discussion, the 0.25 km level is referred to as "the surface" as this is the lowest level where information is available.

(ii) radar reflectivity and vector flow (horizontal and both vertical sections). The total equivalent radar reflectivity (in dBz) is contoured in 10 dBz intervals and superimposed on the vector flow. The vector scale is determined by the magnitude of the longest vector which is given for each diagram.

(iii) potential temperature and pressure perturbations (x-z vertical section only). Potential temperature perturbation (θ') in K or °C is contoured using solid lines and a contour interval of 0.5. Dashed contours of 0.2×10^{-4} interval represent the dimensionless perturbation pressure (π_p') with the letters H and L representing the maximum and minimum pressure perturbations respectively. When the contour spacing becomes too small the contour interval is changed or the contours are simply omitted, as indicated.

In addition, θ' and π_p' horizontal fields at 26 minutes and an updraft (w) horizontal section at 31 minutes are included.

Several graphs will also be used to illustrate the evolution of the storm. Figure 12 is a graph of various terms in the water budget versus time. The curves labeled SCLD*, SRAIN*, SSNOW*, SHAIL* represent the instantaneous total cloud water, rain water, ice/snow and graupel contents respectively, summed over the entire domain. The remaining curves represent the cumulative sums of the various source/sink processes with an "S" (signifying <u>sum</u>) placed before the process names as given in Chapter 3 and in the List of Symbols. Exceptions are RCUM and RCUMH, which represent

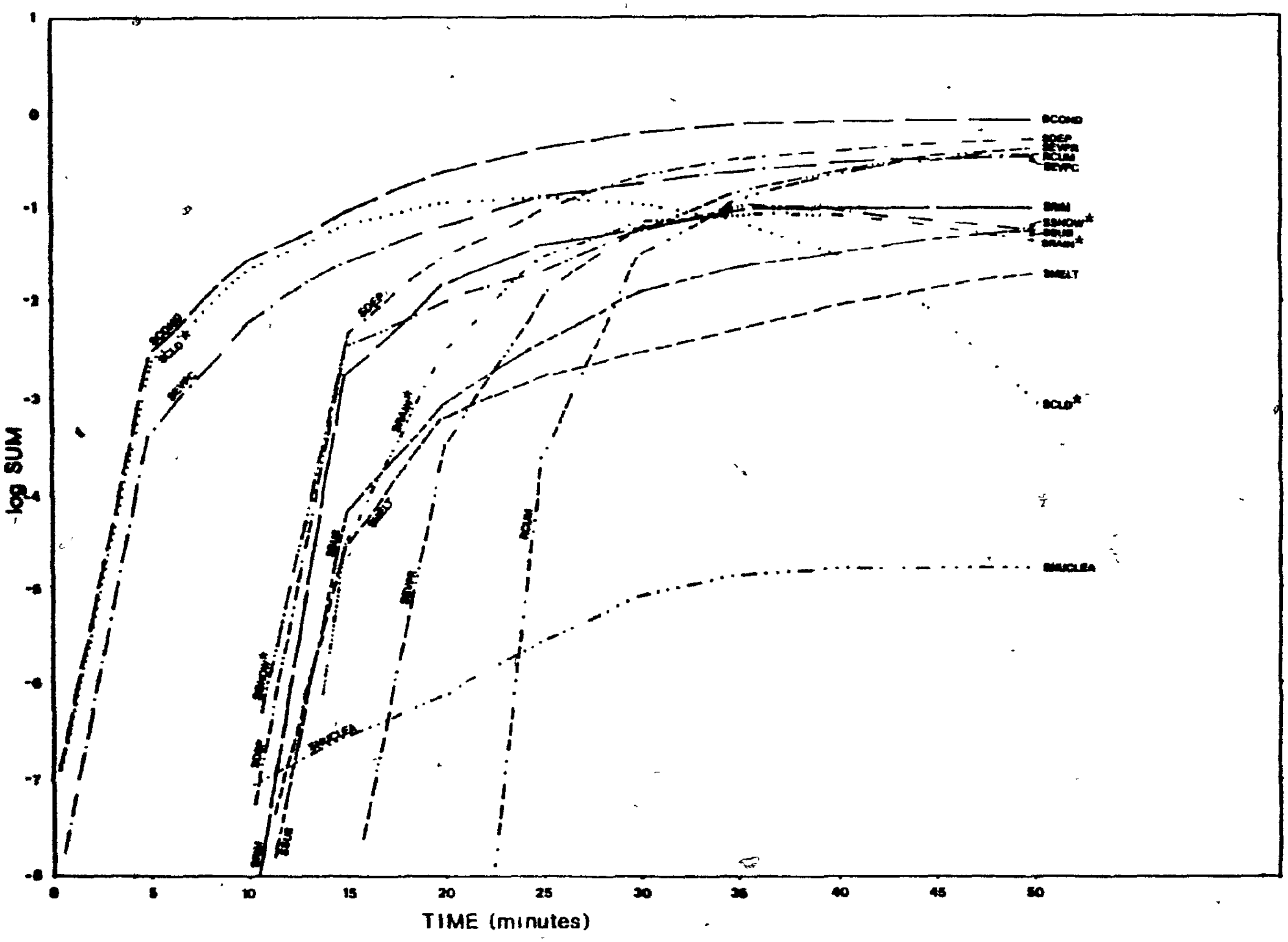

Figure 12a. Water budget terms for cloud, rain and ice/snow. Sums of condensate indicated with an asterisk (*) are instantaneous, while the process sums are cumulative. The log of the sums (in kg m^{-3}) is plotted versus time. To get the total mass summed over the whole domain in kg, the sum must be multiplied by the grid volume, $\Delta x \Delta y \Delta z$ (m^3), which is 5×10^8 m^3.

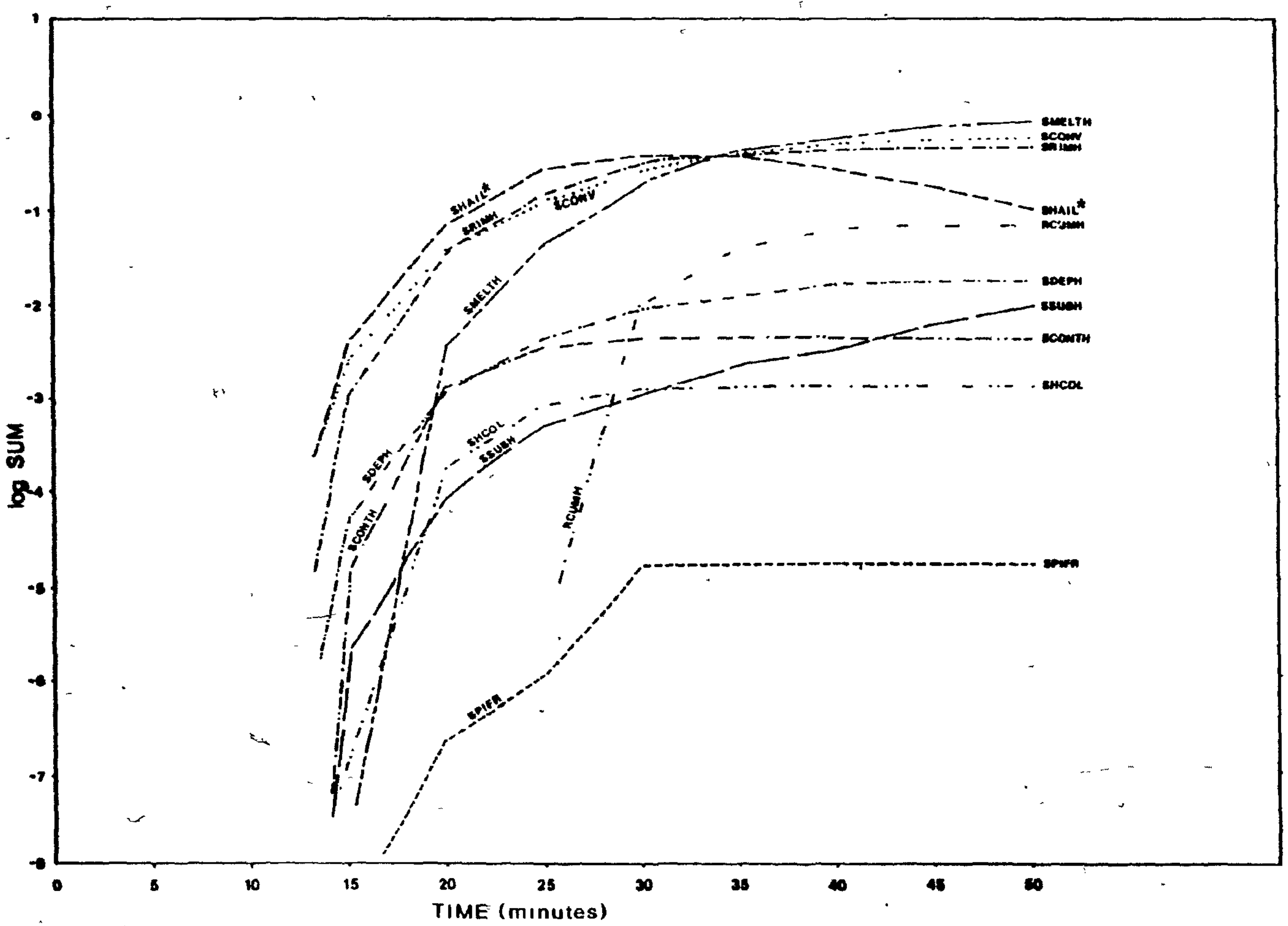

Figure 12b. Same as Figure 12a except for graupel.

the cumulative fallout of rain and graupel, respectively. The log of the sums is plotted. Note that a constant value of a cumulative sum in a given time interval indicates that that particular process has terminated and is no longer active.

Figure 13 shows the variation of the maximum updraft w_{max}, associated maximum downdraft $|w_{min}|$, precipitation-induced maximum downdraft $|w_{minp}|$, graupel and rain maximum "surface" (250 m) mixing ratios ($QGSFC_{max}$ and $QRSFC_{max}$ respectively) with time. The numbers associated with the w_{max} curve indicate the level (in km) of w_{max} and, in general, $|w_{min}|$. $|w_{minp}|$ generally occurs around the 1 km level in connection with the precipitation there. The variation with height of the vertical velocity at several times is shown in Figure 14. The vertical profile is taken along the axis containing w_{max}.

5.2 Simulated hailstorm (3D)

5.2.1 0 - 10 minutes

Convection arises after the introduction of the saturated humidity impulse. A cloud quickly develops at the center of the domain. This cloud is then advected towards the southeast by the mid-level environmental winds. The cloud base is at approximately 2.0 km height and the cloud top rises with the maximum updraft which increases in height and magnitude, as shown in Figure 13. Figure 12a shows that, for this period, the main process is condensation while evaporation is the only sink of cloud water. During this time a small amount of nucleation occurs at each time step to create a minute amount of ice/snow content (too small to be indicated on the graph).

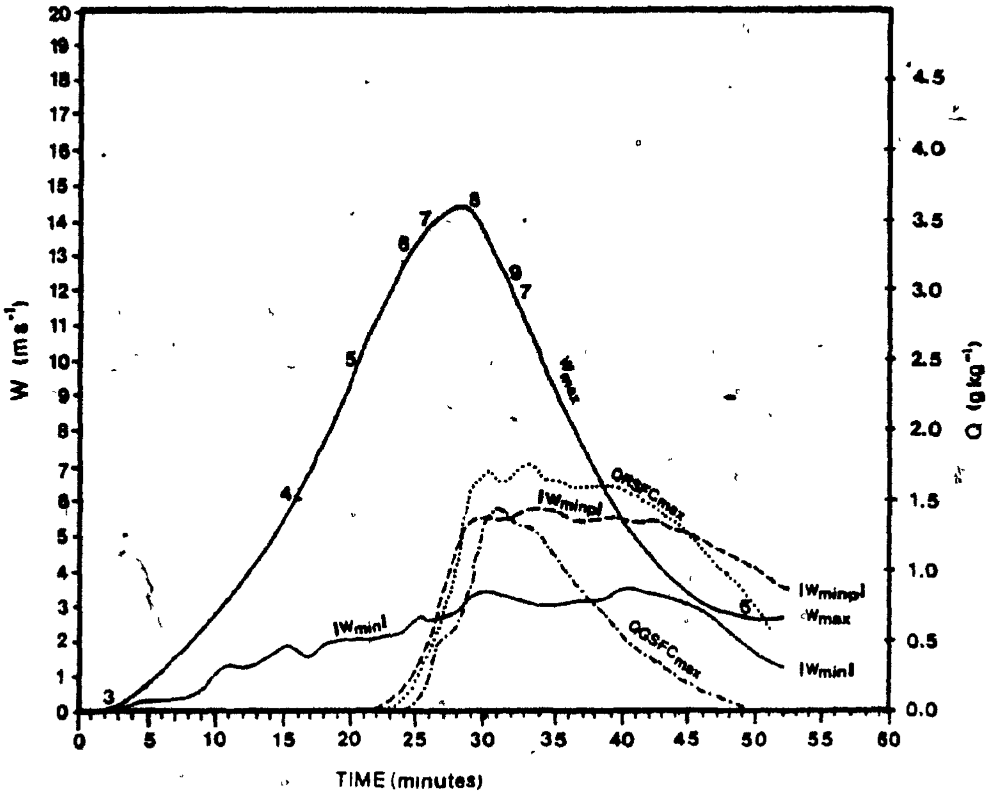

Figure 13. Maximum updraft (w_{max}), downdraft $|w_{min}|$, precipitation-induced downdraft $|w_{minp}|$, surface rain mixing ratio $QRSFC_{max}$ and surface graupel mixing ratio $QGSFC_{max}$ versus time. Numbers above the w_{max} curve indicate the level of w_{max} in km.

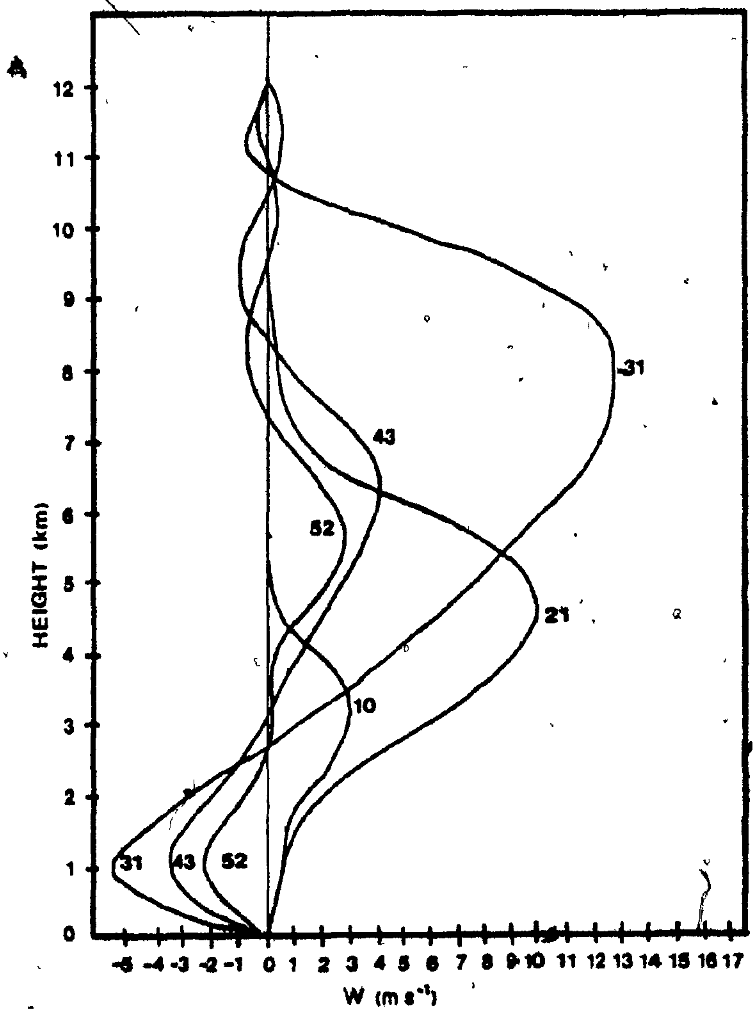

Figure 14. Vertical velocity (w) profiles in the vertical (z) direction at 10, 21, 31, 43 and 52 minutes taken along the w_{max} axis.

5.2.2 10 - 20 minutes

At about 10 minutes, the cloud breaks through the relatively moist stable layer (see Figure 4) resulting in a large increase in nucleation at this level (3 to 4 km) and thereby substantially increasing the ice/snow content as indicated in Figure 12a. This snow content grows mainly by deposition and riming with melting and sublimation contributing almost equally to ice/snow depletion. The breakthrough eventually allows the updraft maximum to accelerate up (along with the cloud top) and grow in magnitude, producing a tall, vigorous hailstorm. Also, the resulting nucleated ice/snow is eventually converted into graupel which initiates the graupel field. Thus the breakthrough at 10 minutes is a crucial factor in the subsequent development of the storm. Both rain and graupel are initiated at 13 minutes near the cloud water maximum at the center of the cloud (3 km height). Autoconversion of cloud (not shown in Figure 12) initiates the rain field while conversion from snow crystals initializes the graupel field (see Figure 12b). The supercooled initial rain field (above the 0°C isotherm) is quickly depleted by freezing upon contact with ice crystals (which adds to the graupel) and, to a lesser extent, through evaporation and collection by graupel. The graupel content grows mainly through the riming of cloud water and the continued conversion of snow crystals. The riming of cloud water, combined with evaporation, now becomes a major sink of cloud water. At first, sublimation is the main sink for graupel until the graupel begins to fall below the 0°C isotherm and melt into rain (at 16 minutes). Thus, by 20 minutes, melting has become the dominant graupel sink while becoming the major source of rain (which is now below the 0°C isotherm). The updraft maximum reaches 5 km and 9.5 m s^{-1} by 20 minutes and continues to accelerate upward with the continual release of latent heat from condensation and freezing (Figure 13).

5.2.3 Sections at 21 minutes -- growing stage

Figure 15a shows a vertical slice (x-z plane) through the storm at 21 minutes in its growing or cumulus stage. The small cloud on the left (west) side of the main development formed between 10 and 16 minutes in response to a slight horizontal oscillation in the buoyancy/updraft field. This smaller cloud, which acquires small quantities of ice/snow, rain and graupel, eventually merges with the main cloud between 35 and 40 minutes. From this point on, all references will be to the main storm cell as the influence of the small cell is negligible.

As shown in Figure 15a, cloud, ice/snow, rain and graupel are all present at this time. The cloud has the general appearance of a cumuliform cloud and has a base around 2 km and a top around 6.5 km height. Note the area of rain from melted graupel below the 0°C isotherm which is falling towards the surface and the smaller region of rain above extending towards the center of the cloud. This latter region arose mainly from autoconversion and is being rapidly depleted by contact freezing and collection by graupel (as mentioned above). The graupel field, with a maximum of 1.87 g kg^{-1} (heavy graupel) just below the cloud water maximum (1.75 g kg^{-1}), extends over the entire cloud field. The regions without ice/snow (asterisks) in the cloud result from the complete conversion of the ice/snow content at these points into graupel.

Figure 15b shows the radar reflectivity associated with the precipitation (rain and graupel) regions of Figure 15a superimposed on the vector flow field in the x-z (W-E) plane. Inflow into the storm in this plane

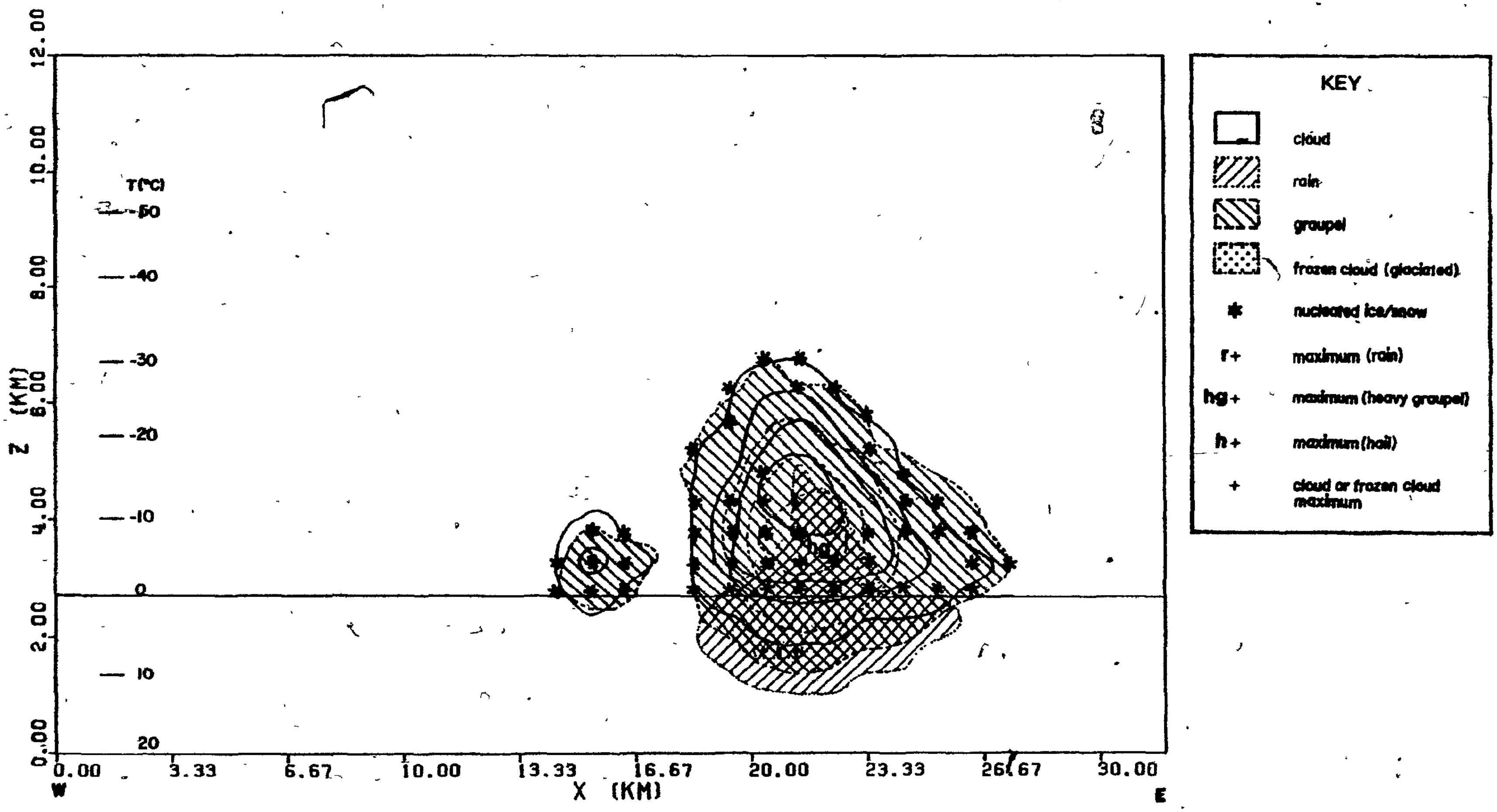

Figure 15a. Vertical x-z section of cloud (solid contours), rain (dotted contours, right-slanting shading), ice/snow (asterisks), and graupel (dashed contours, left-slanting shading) at 21 minutes (growing stage) taken at y = JMAXW = 19 km. More information in key and text.

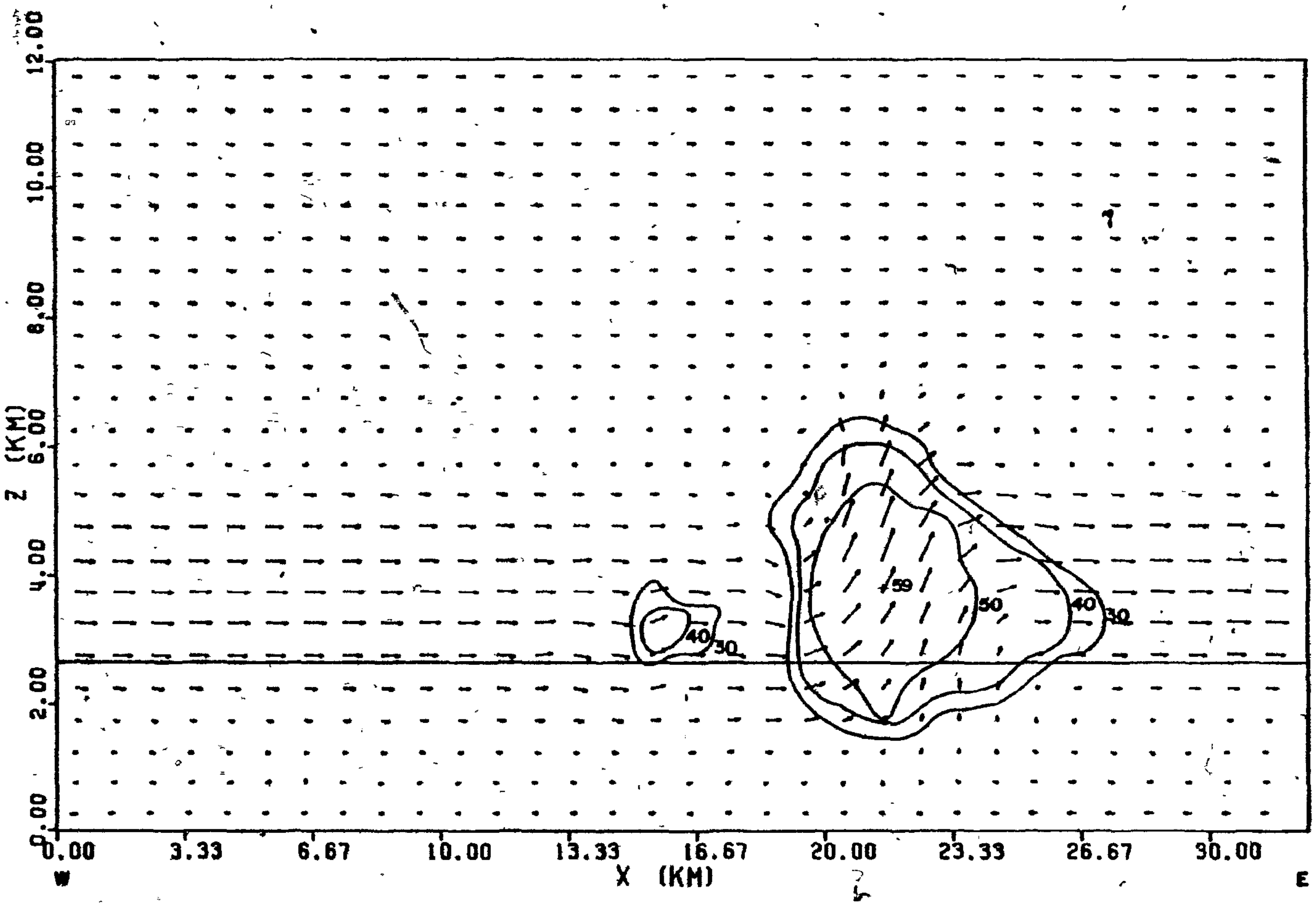

Figure 15b. Vertical x-z section of radar reflectivity (contours labeled in dBz) and flow at 21 minutes taken at y = JMAXW = 19 km. Solid horizontal line is the 0°C level. The magnitude of the longest vector is 7.65 m s^{-1}.

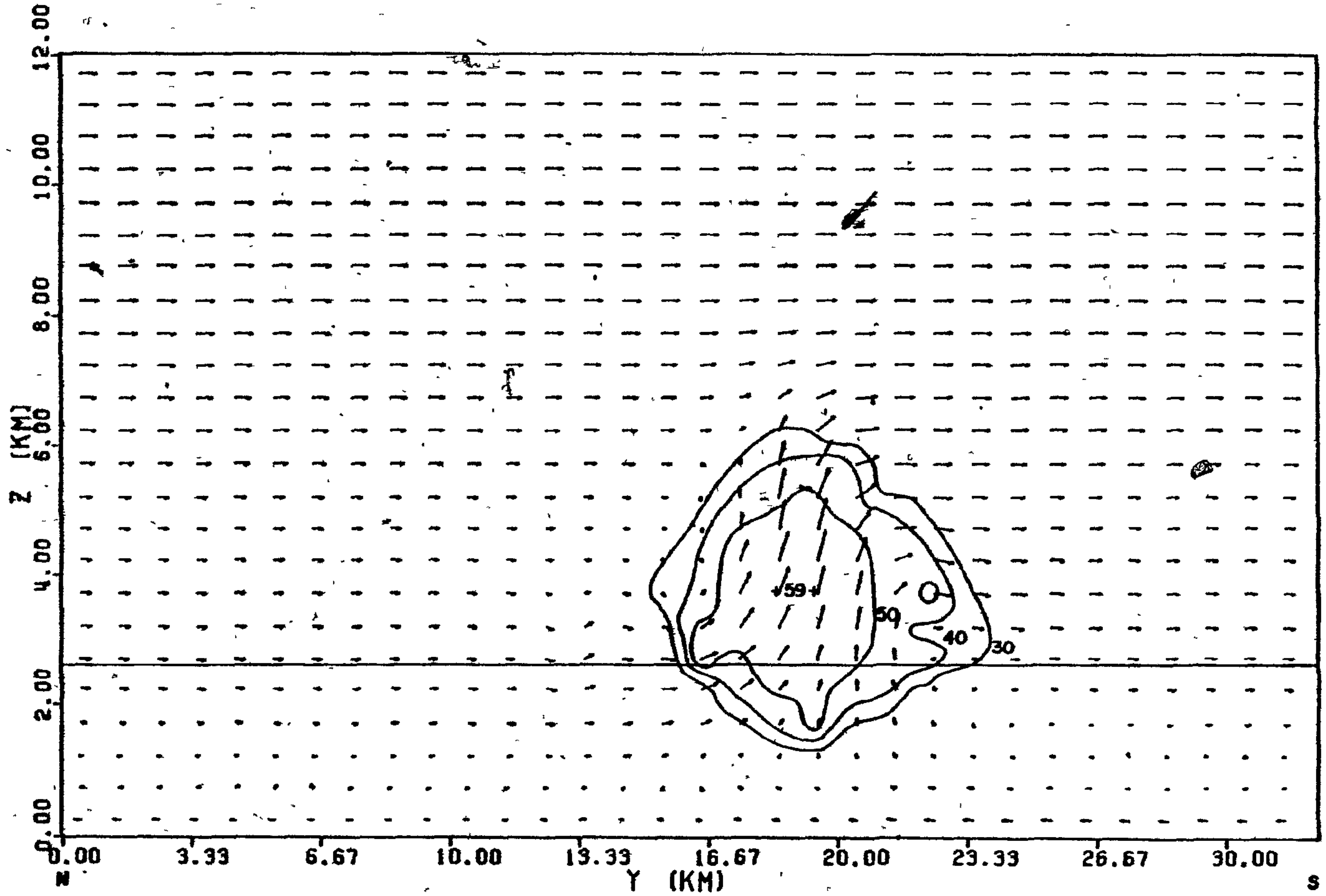

Figure 15c. Vertical y-z section of radar reflectivity (contours labeled in dBz) and flow at 21 minutes taken at x = IMAXW = 22 km. Solid horizontal line is the 0°C level. The magnitude of the longest vector is 10.4 m s^{-1}.

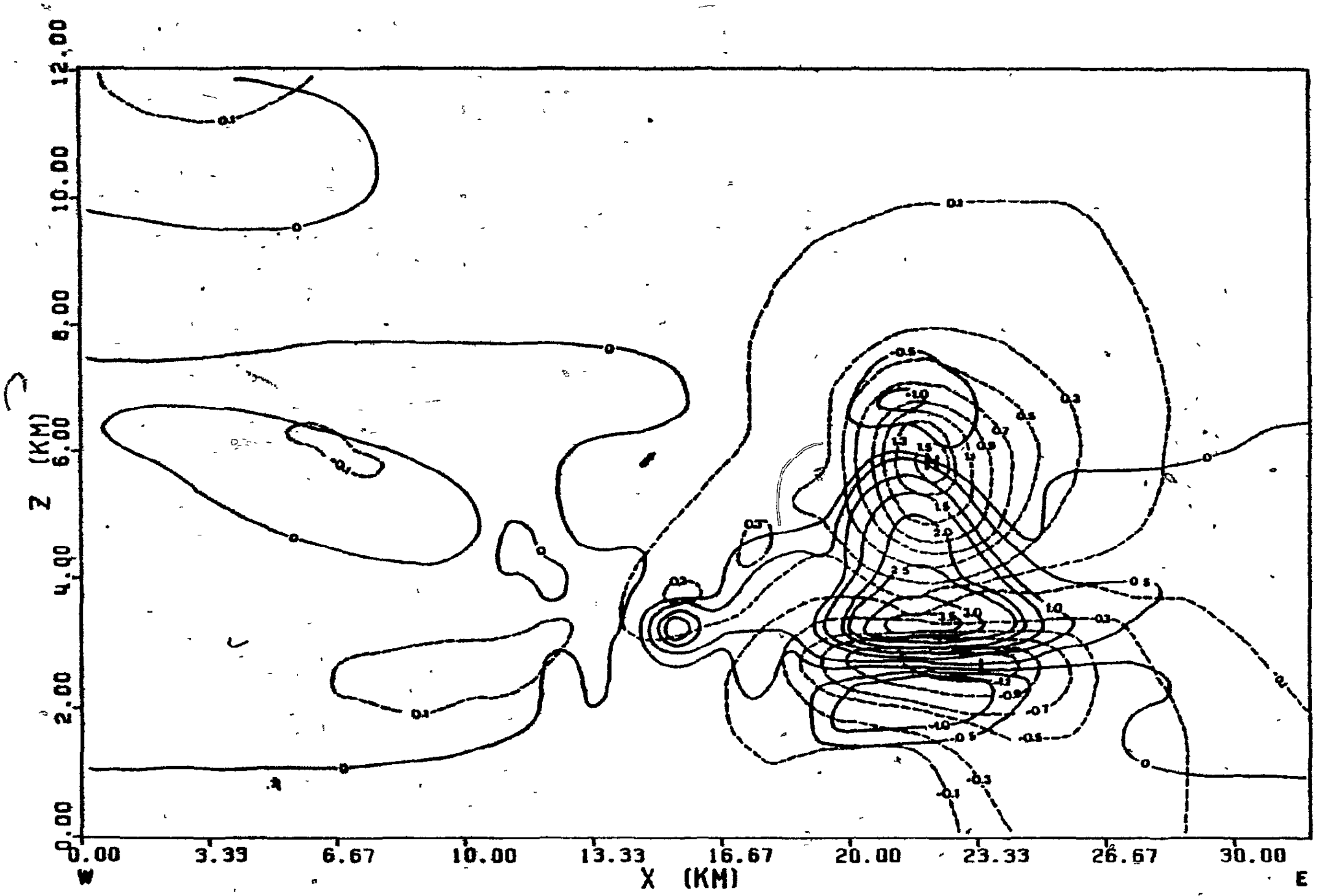

Figure 15d. Vertical x-z section of dimensionless perturbation pressure (π_p') x 10^4 (dashed lines) and potential temperature perturbation (θ') in °C or K (solid lines) at 21 minutes and at y = JMAXW = 19 km. Contour intervals are 0.2 and 0.5 for π_p' and θ' respectively. "H" and "L" represent points of maximum and minimum π_p' respectively.

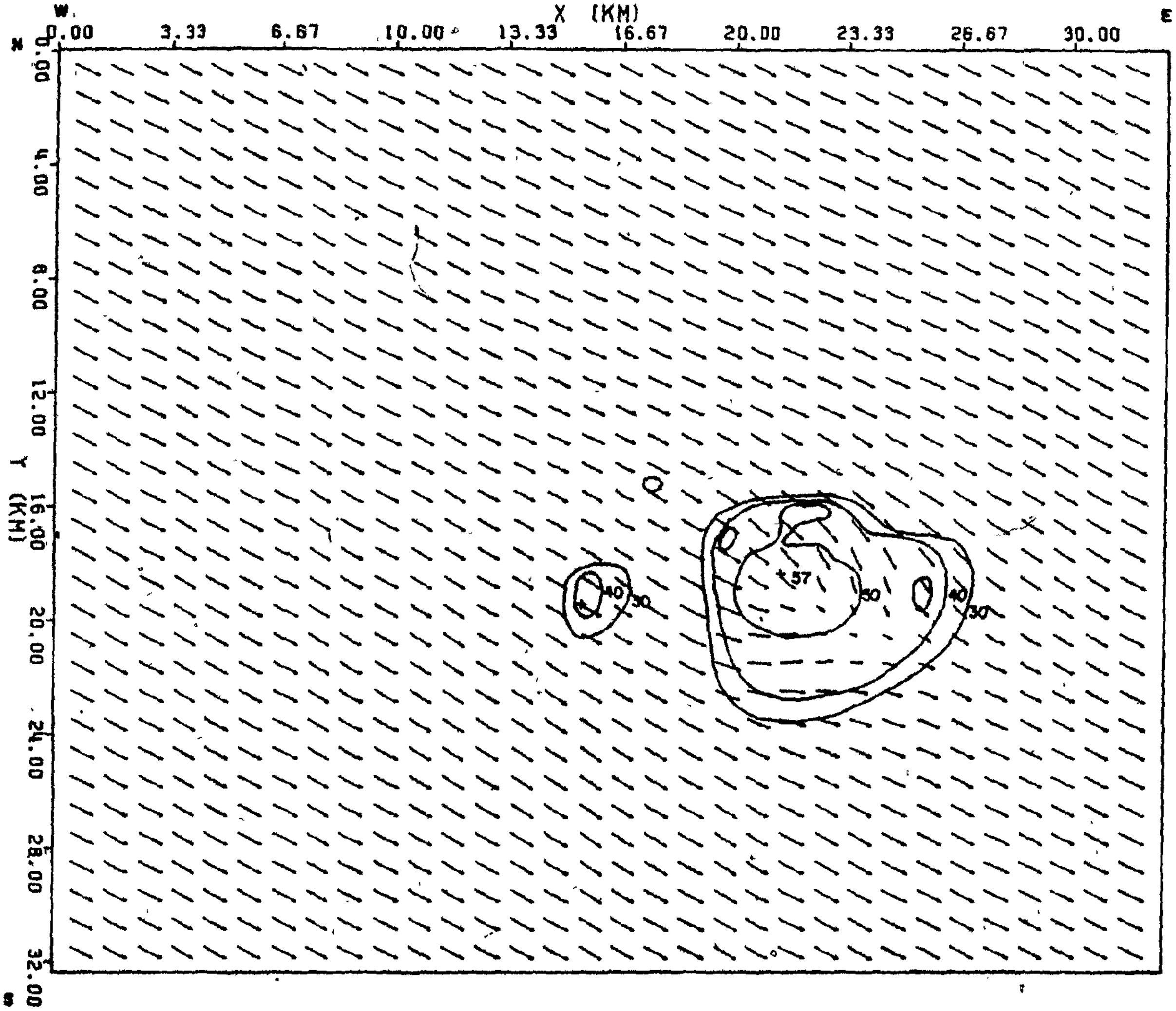

Figure 15e. Horizontal x-y section of radar reflectivity (contours labeled in dBz) and flow at 21 minutes taken at z = 2.75 km. The magnitude of the longest vector is 7.75 m s^{-1}.

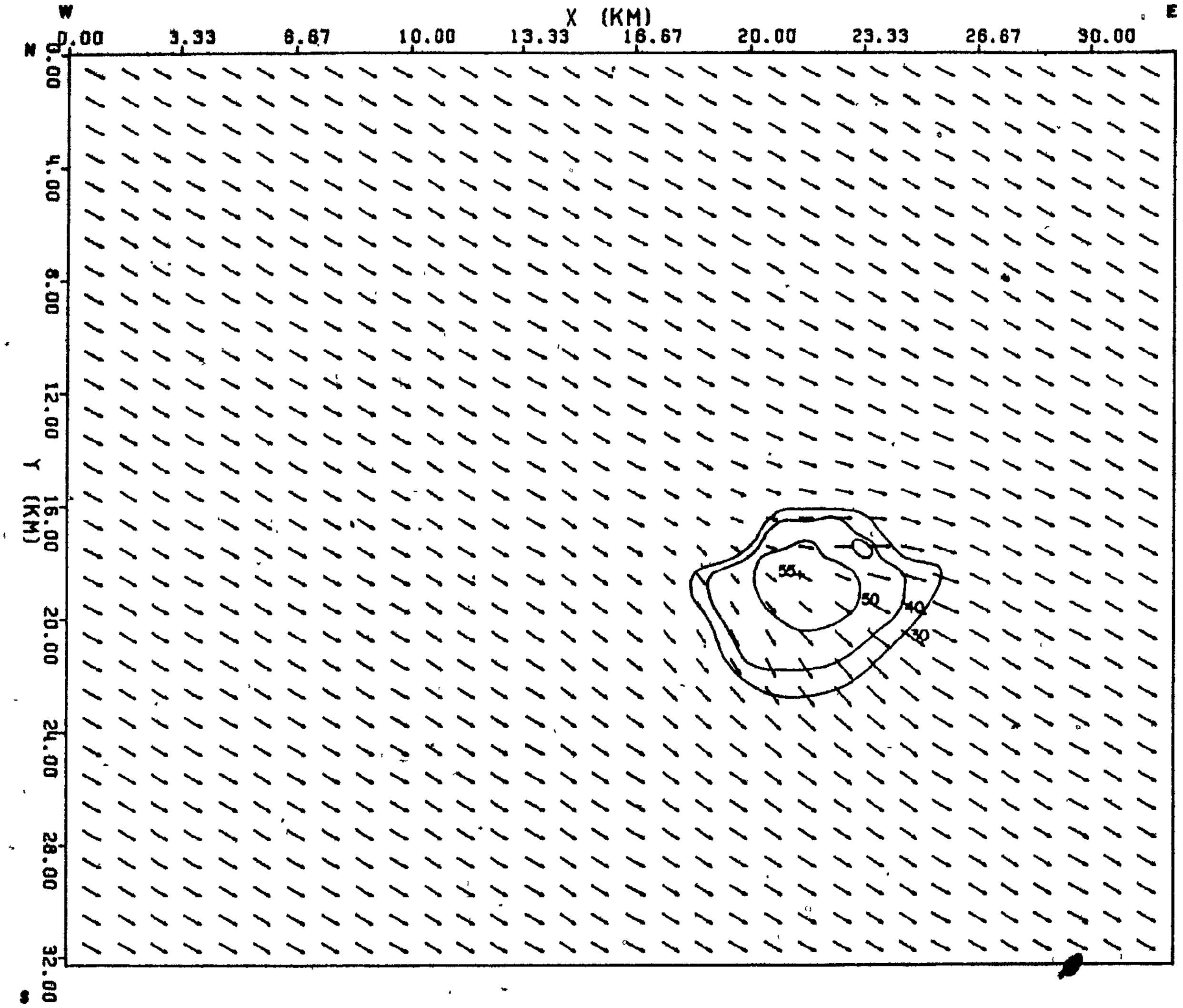

Figure 15f. Same as Figure 15e, except at $z = 4.75$ km, and the magnitude of the longest vector is 9.75 m s^{-1}.

comes from two regions: from the mid-level westerly "jet" between 2 and 5 km height and from the relatively weaker inflow of warmer surface air from the east which slopes up into the storm. The two regions of inflow combine in a slightly tilted updraft. Note the precipitation overhang on the east side of the storm caused by the advection by the westerly flow of condensate over the region of surface inflow and updraft on this side (east). Note also the "compression" of contours on the west inflow side. The point of maximum reflectivity (59 dBz) is located in the updraft core near the center of the storm in connection with the graupel maximum there. The slight oscillation in the flow around the 0°C (solid line) level is also evident in connection with the small cloud on the west side of the main cell (as mentioned above). The reflectivity and flow in the y-z (N-S) plane is shown in Figure 15c. An oscillation in the flow in this plane on the north side of the storm, similar to that in Figure 15b, is evident in this figure as well, although there is no associated cloud. A weak low-level inflow from the south is evident while a mid-level inflow from the north, much weaker than the westerly "jet" in the x-z plane, creates a less obvious radar overhang.

Figures 15e and f are horizontal (x-y) slices through the storm at the 2.75 and 4.75 km levels respectively. They give the horizontal flow and reflectivity structures at these levels. Evident in these figures are the overhang and the inflow side contour compression as well as the position of the core of maximum reflectivity. By combining the information of Figures 15b, c, e and f, a picture of the storm and flow in three dimensions can be obtained. It can be seen that a relatively strong west-northwest mid-level inflow combines with a weaker low-level inflow from the southeast in a slightly tilted updraft. The result is an almost vertical storm with an overhang extending towards the southeast over the low-level inflow.

The perturbation pressure (π_p') and potential temperature perturbation (θ') fields in the same plane as Figures 15a and b (the x-z vertical plane) are given in Figure 15d. Note the region of high-pressure perturbation (H) centered above the storm and the low (L) near the cloud base resulting in a pressure gradient force in a direction opposed to the updraft. This feature is typical of numerical cloud simulations (e.g. Schlesinger, 1975, 1978). Also typical is the area of positive potential temperature perturbation in the cloud (and in the small cloud) corresponding to the latent heat released from condensation and freezing and the areas of negative potential temperature perturbation above and below the cloud. The area above the cloud is cooled by evaporation and sublimation while the sub-cloud region is cooled mainly by the melting and evaporation processes. The proximity of the in-cloud θ'_{max} and the sub-cloud θ'_{min} centers gives rise to a high potential temperature perturbation gradient. These temperature perturbation effects are enhanced by the presence of the ice phase, which can be a significant source and sink of latent heat through the associated phase transitions such as melting, freezing, and sublimation (see thermodynamic equation (57) in Chapter 3). Thus larger perturbations from the basic state temperature are to be expected in cloud simulations that include active ice phase processes when compared with models which simulate only warm rain processes.

5.2.4 20 - 30 minutes

Rain (from melted graupel) reaches the surface first at approximately 22 minutes while graupel follows soon after at 24 minutes (Figure 13). The effect of the precipitation on the pressure and potential temperature perturbation fields is shown in Figures 16a and b. These figures show π_p' (dashed lines) and θ' (solid lines) fields in the horizontal at 25 minutes at the surface (16a) and at 2.25 km (16b), shortly after the surface precipitation has started. At the surface, an area of high pressure is spreading out, in response to precipitation loading, which is replacing the former surface low. The evaporation of rain and melting graupel results in a region of cooling near the center of this high. Two km above this level (Figure 16b), just below the cloud base, a low is found above the surface high with a precipitation-induced area of cooling evident here as well. The surface high and cool region evident in these and later figures are often-observed features of storms with moderate precipitation. (The dome of cooled surface air often creates a "mini cold front" which can trigger new convective cells.)

The maximum rain content ($QRSFC_{max}$) and graupel content ($QGSFC_{max}$) at the surface both rise rapidly to maximum values of 1.7 and 1.45 g kg^{-1} ($\overline{D}_{max}$ = 0.195 cm) respectively at 30 minutes, the time of maximum storm intensity. During this time, maximum graupel contents in the cloud reach 2.9 g kg^{-1} ("hail" with $\overline{D}_{max}$ = 0.2 cm) around the 4 km level in the updraft core. Also shown in Figure 13 is the rapid acceleration of the updraft maximum (w_{max}) from 5 km height to over 8 km in this time period, giving an average rate of rise of 2.5 m s^{-1} for the w_{max} center. By 30 minutes, the updraft maximum has reached its maximum magnitude (14.4 m s^{-1}) but is still rising. Note also the creation of a precipitation-induced downdraft $|w_{minp}|$ which increases rapidly with the increasing precipitation content to about 5.5 m s^{-1} by 30 minutes to surpass the magnitude of the upper-level, updraft-associated downdraft $|w_{min}|$.

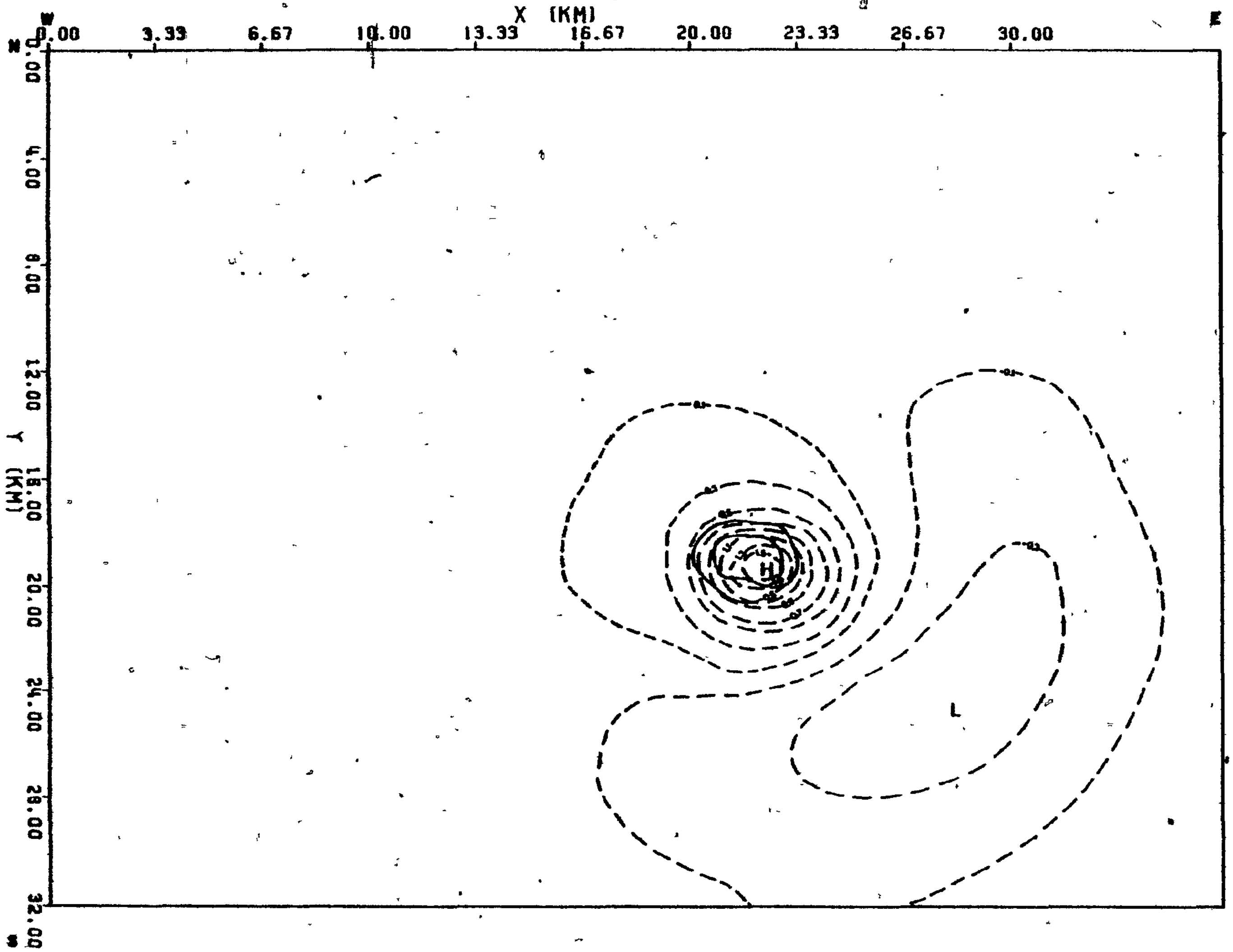

Figure 16a. Horizontal (x-y) section of π_p' (dashed) and θ' (solid) at 25 minutes and taken at z = 0.25 km (the "surface"). Contour intervals are as in Figure 15d.

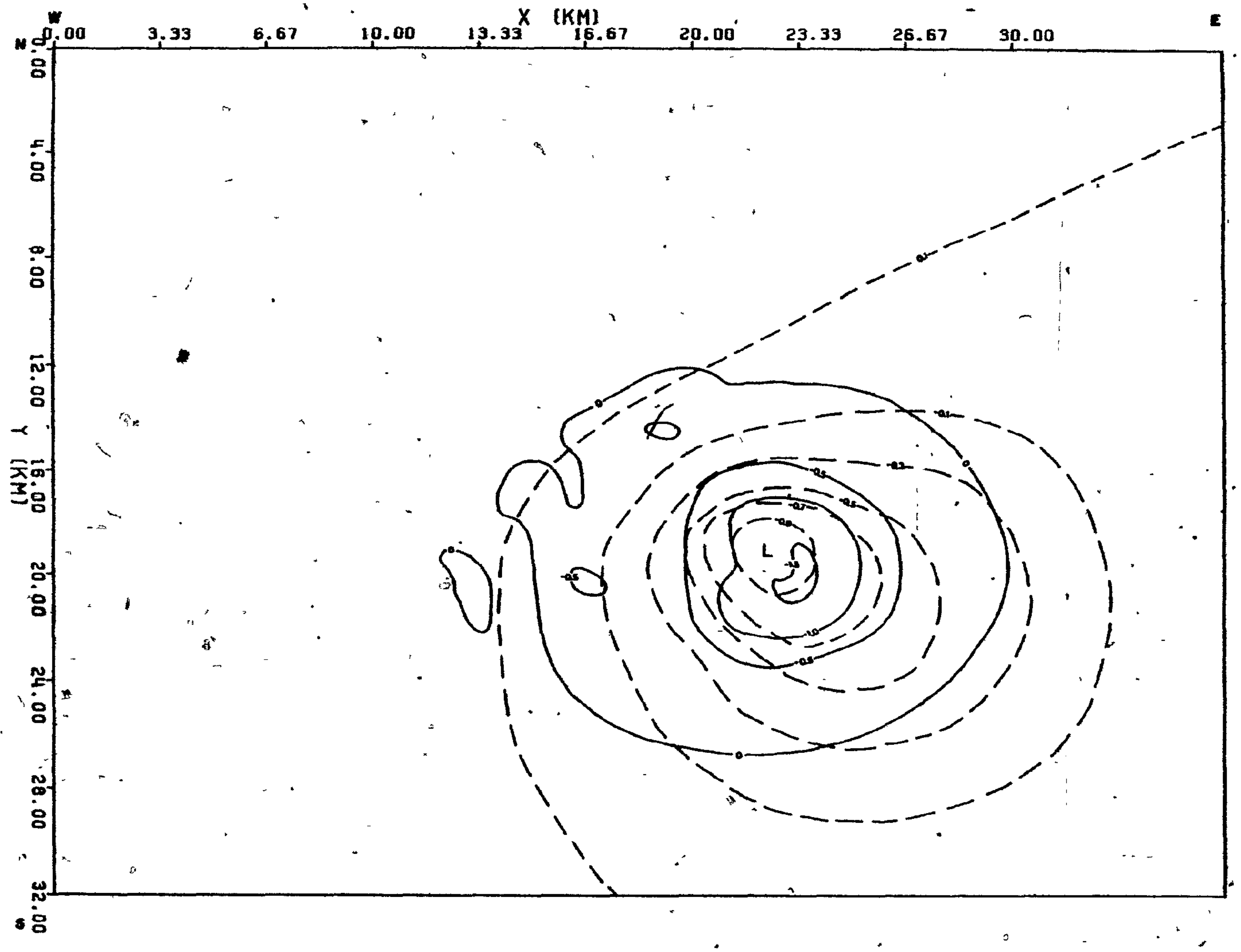

Figure 16b. Same as Figure 16a, except at z = 2.25 km.

By 25 minutes, the storm has penetrated the -35°C level, above which all the cloud water advected into this region is frozen, or glaciated, creating an "ice cap" on the storm. Glaciation thus becomes an important sink of cloud water and source of ice/snow. The increase in ice/snow content due to glaciation can be seen in the SSNOW curve of Figure 12a from 25 to 30 minutes. Continuing to refer to Figures 12a and b, it can be seen that by 30 minutes all processes are active. The fallout of rain (RCUM) and graupel (RCUMH) become significant sinks for both types of precipitation. Cloud water continues to be condensed but the total cloud water begins to decrease due to evaporation, glaciation (above the -35°C level) and riming by ice/snow and graupel. Melting graupel, the main graupel sink, is the major source of rain below the 0°C isotherm with very little rain above this level (which accounts for the relatively low rates of contact freezing, collection of rain by graupel and especially Bigg's freezing -- all dependent on supercooled rain). Fallout and evaporation are the main processes tending to deplete the rain. Deposition and riming both continue to be major contributors to the ice/snow content which is being depleted by conversion to graupel and sublimation. By 30 minutes, the rate of increase to the graupel content by conversion and riming is nearly balanced by the loss of graupel from melting and fallout.

5.2.5 Sections at 31 minutes -- mature stage

The storm, at this time, is near its peak of development. Figure 17a shows the storm in the vertical x-z plane. It has moved farther east and has grown into a large storm of 10 km width which has penetrated to the height of the tropopause (about 10 km). Note the large "ice cap" above the -35°C isotherm referred to above. Maximum ice/snow contents in the cap,

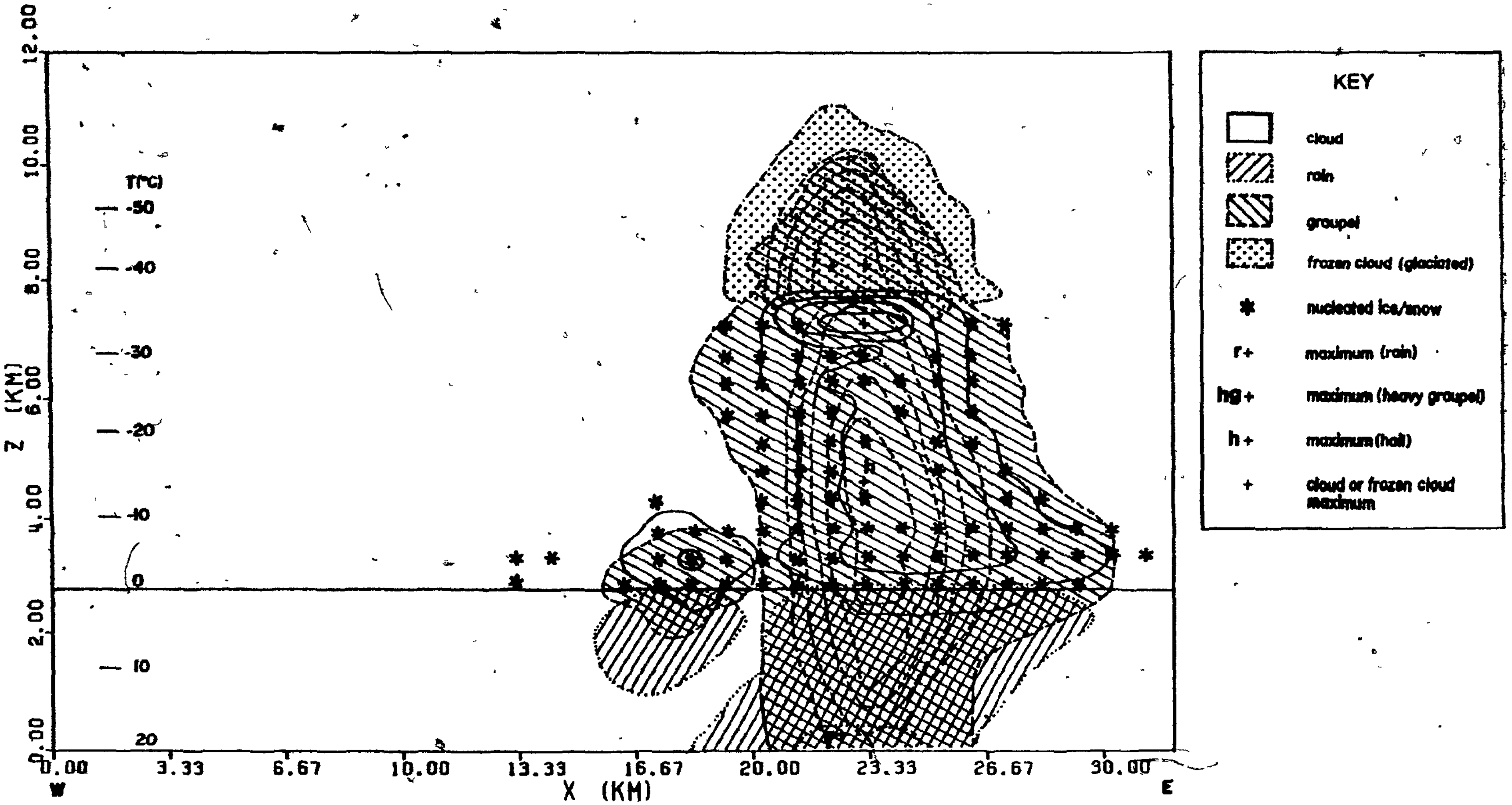

Figure 17a. Same as Figure 15a, except at 31 minutes (mature stage) and taken at y = JMAXW = 21 km.

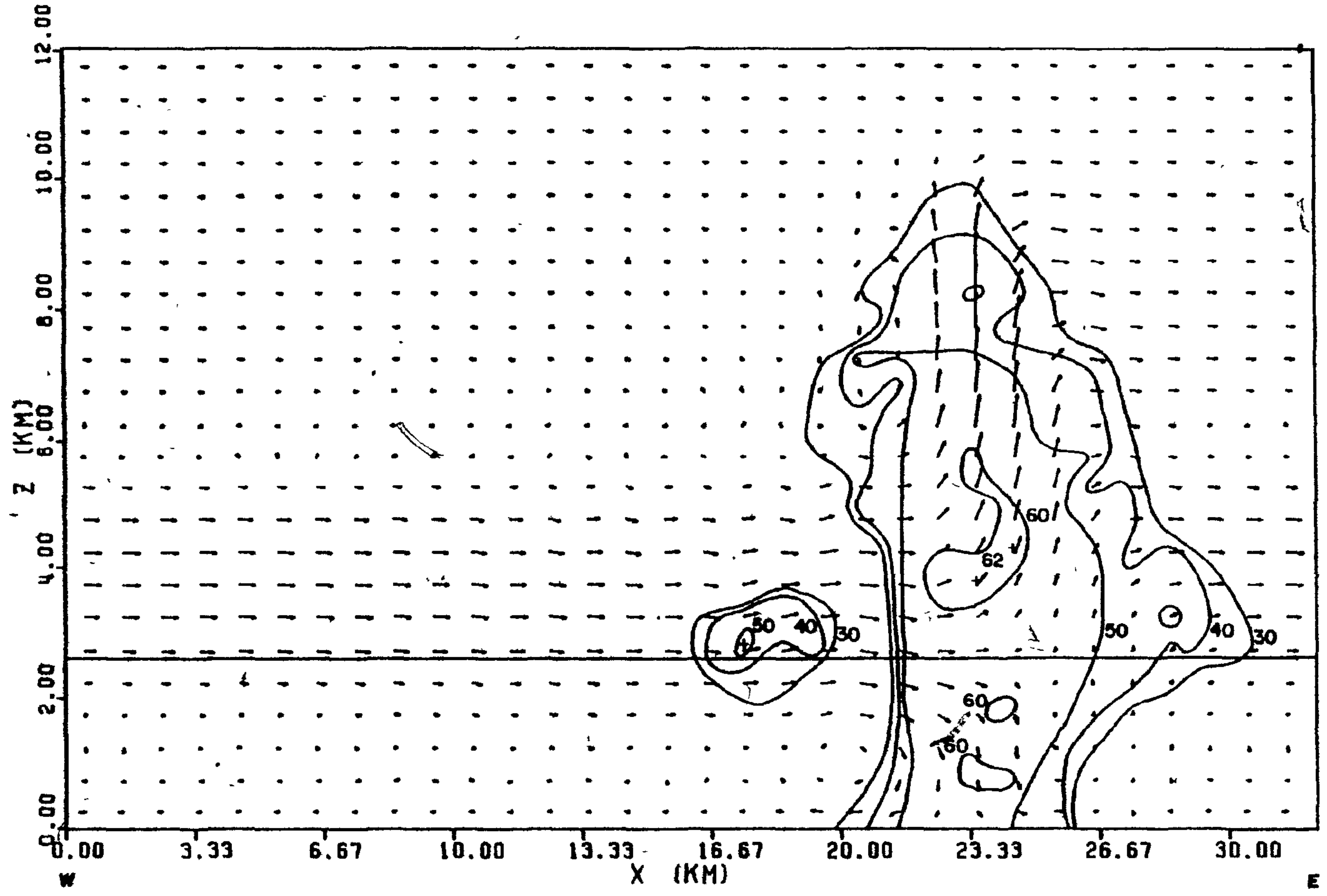

Figure 17b. Same as Figure 15b, except at 31 minutes and taken at y = JMAXW = 21 km. The magnitude of the longest vector is 13 m s^{-1}.

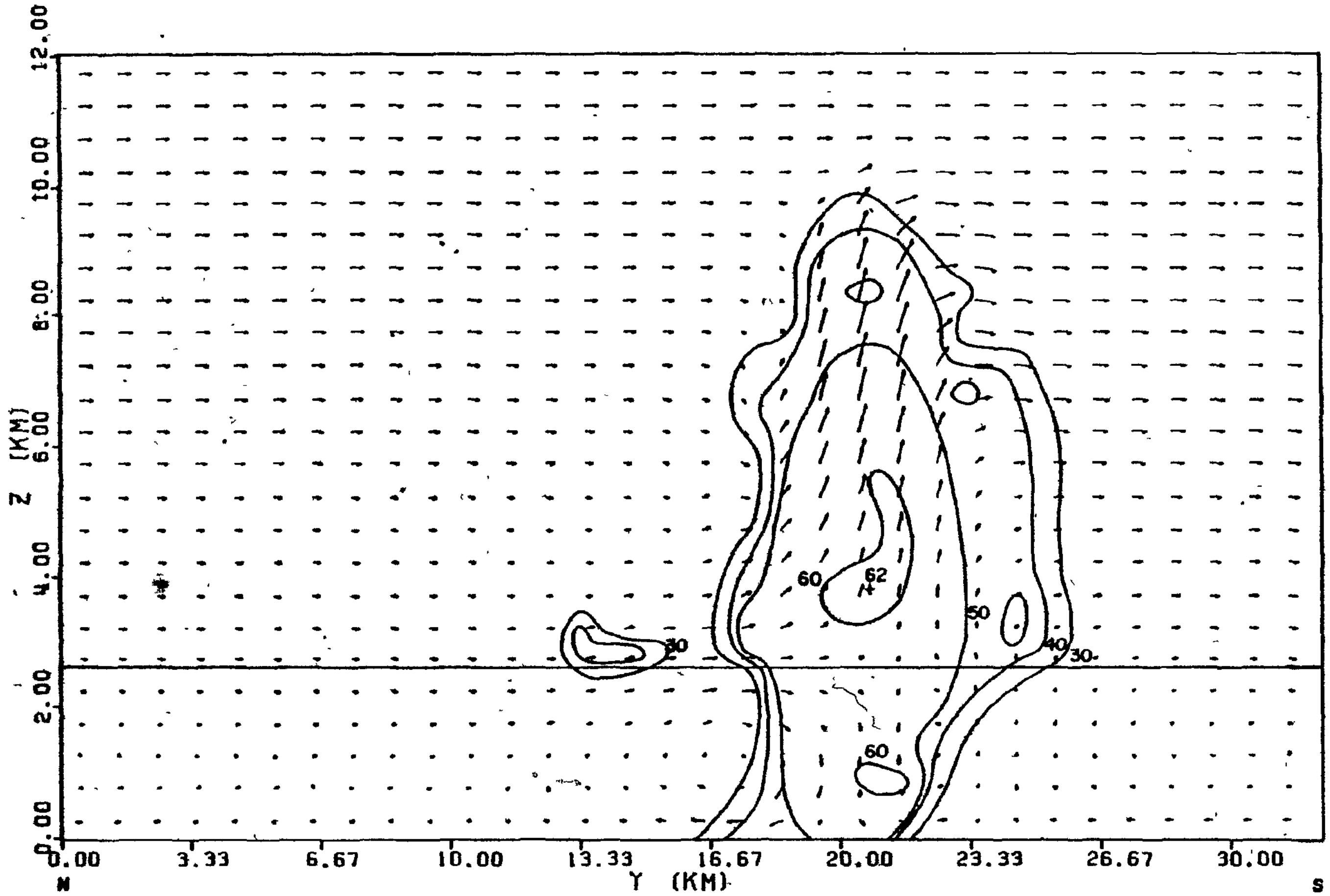

Figure 17c. Same as Figure 15c, except at 31 minutes and taken at x = IMAXW = 24 km. The magnitude of the longest vector is 13.6 m s^{-1}.

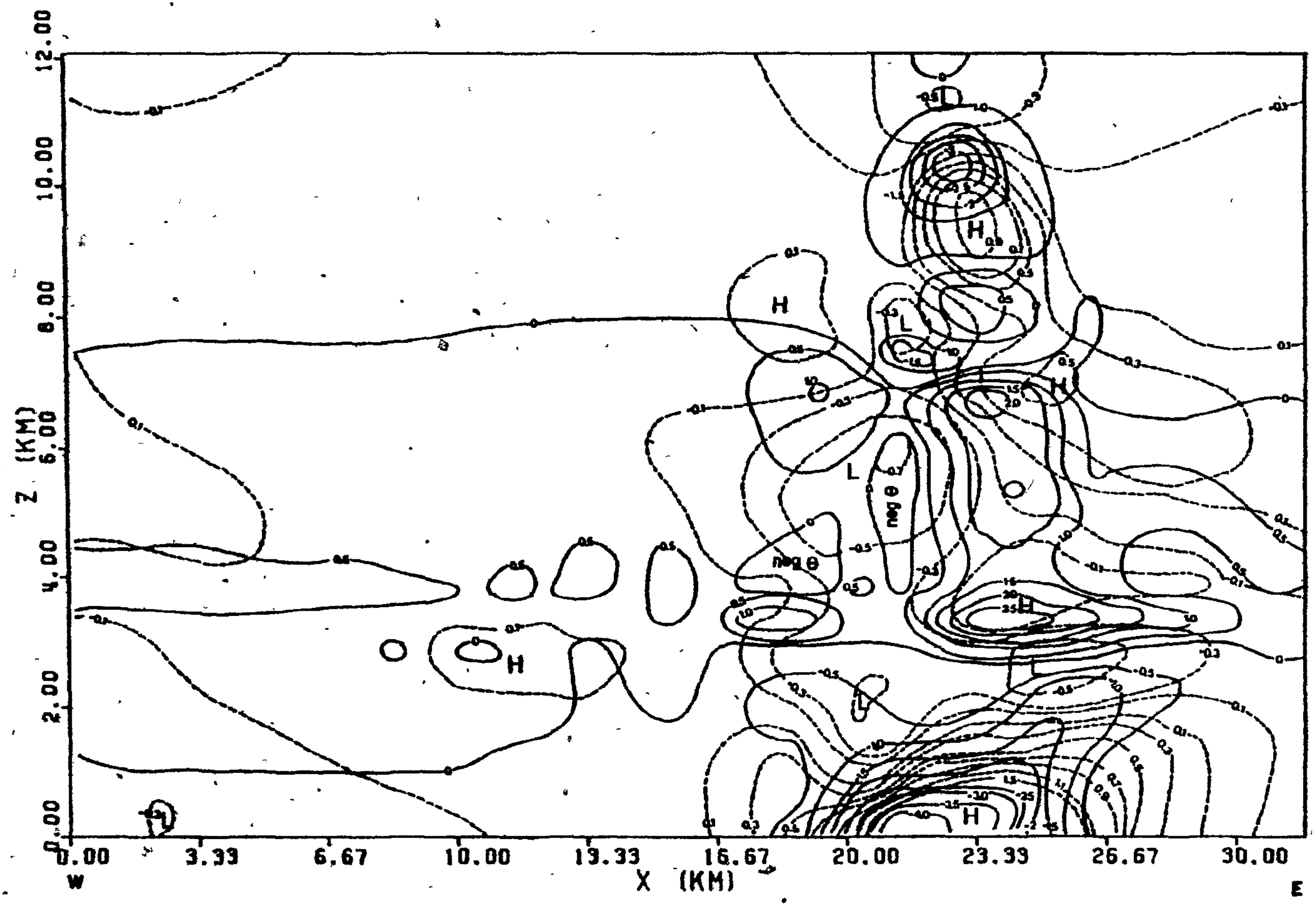

Figure 17d. Same as Figure 15d, except at 31 minutes and at y = JMAXW = 21 km. π_p' contours greater than 1.5 near the surface were too closely spaced to indicate as $\pi_p'{}_{max}$ at the surface (H) was 3.3 (x 10^{-4}).

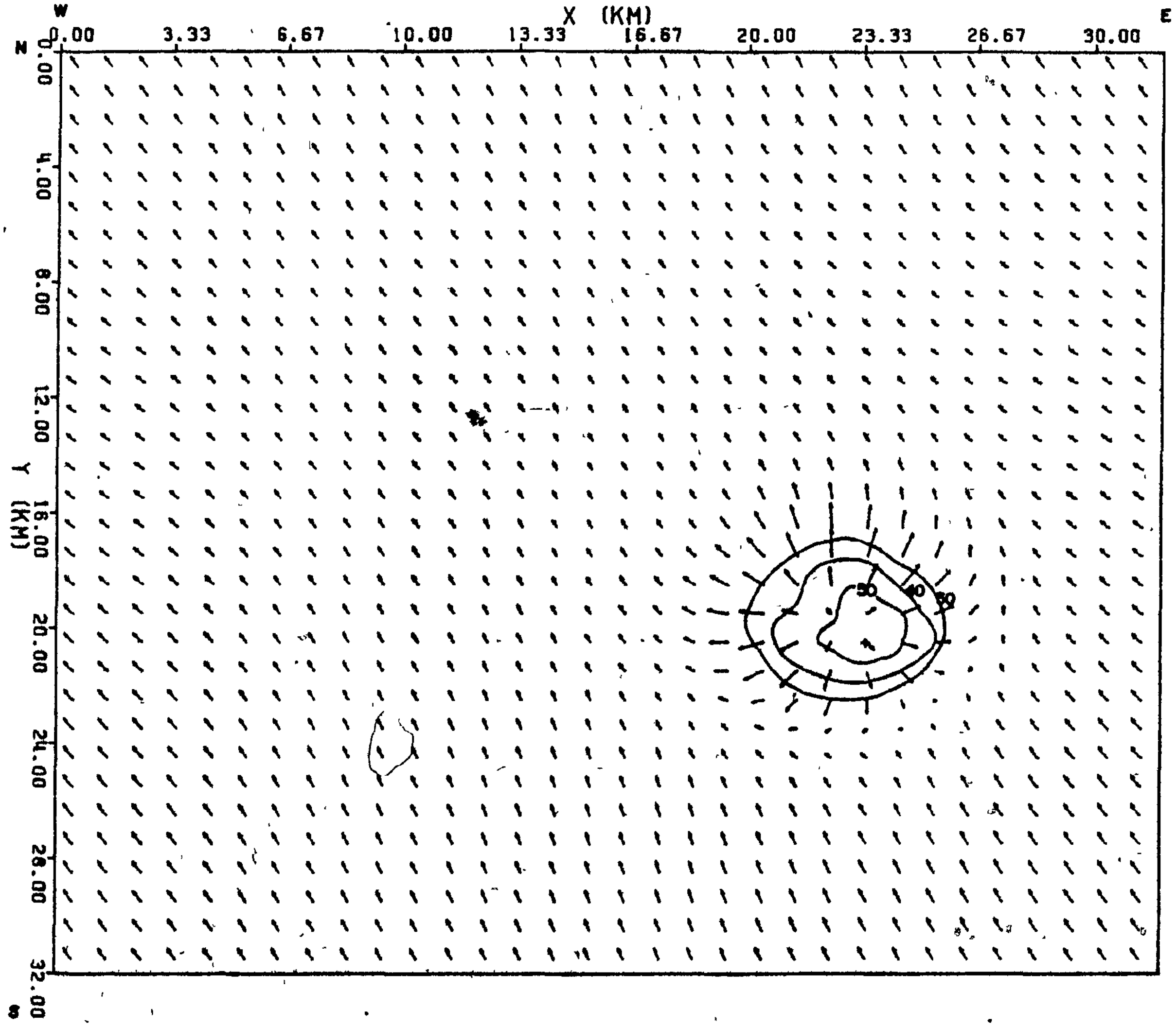

Figure 17e. Same as Figure 15e, except at 31 minutes and at z = 0.25 km. The magnitude of the longest vector is 7.1 m s^{-1}.

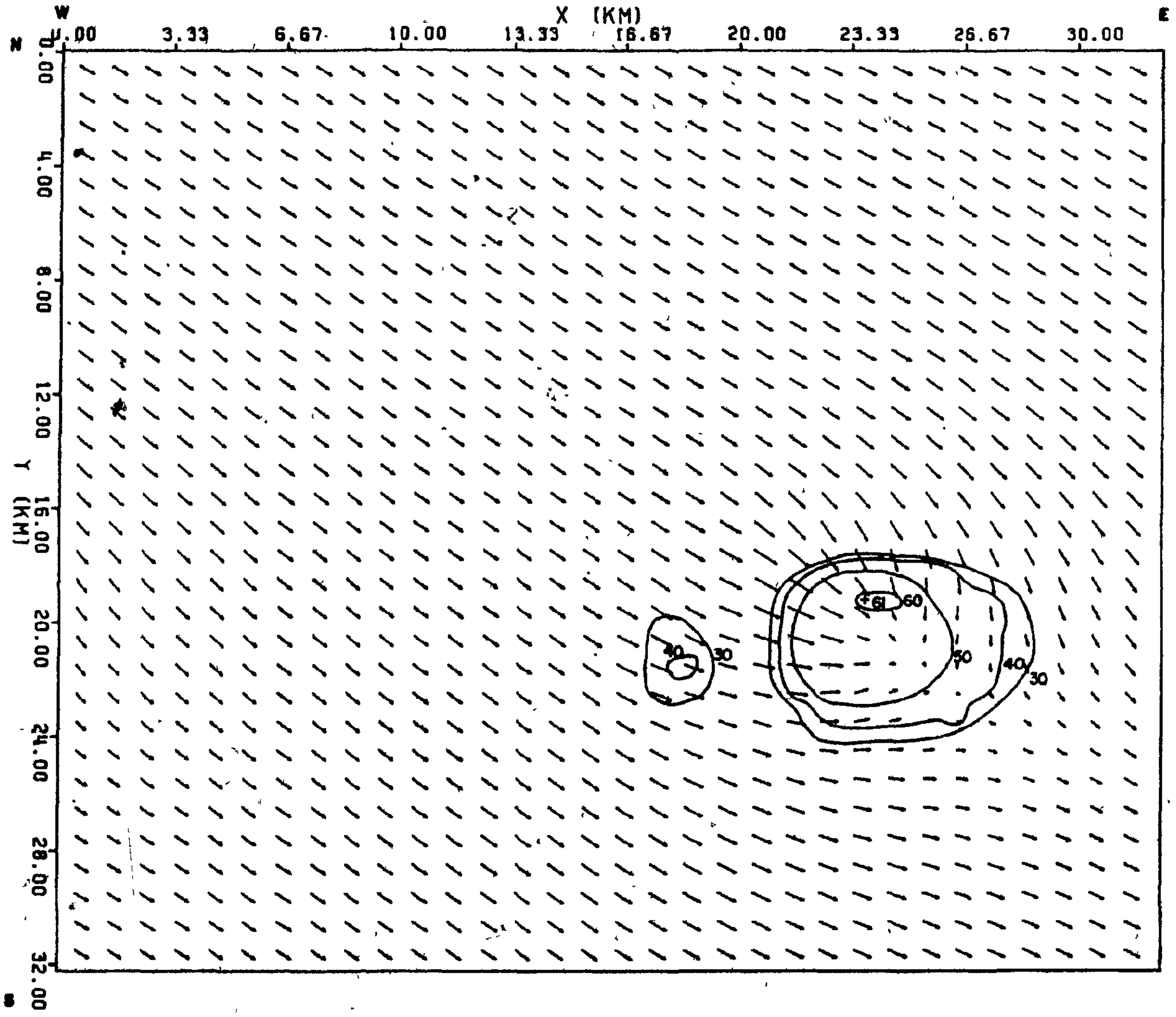

Figure 17f. Same as Figure 15e, except at 31 minutes and at z = 2.25 km. The magnitude of the longest vector is 7.9 m s^{-1}.

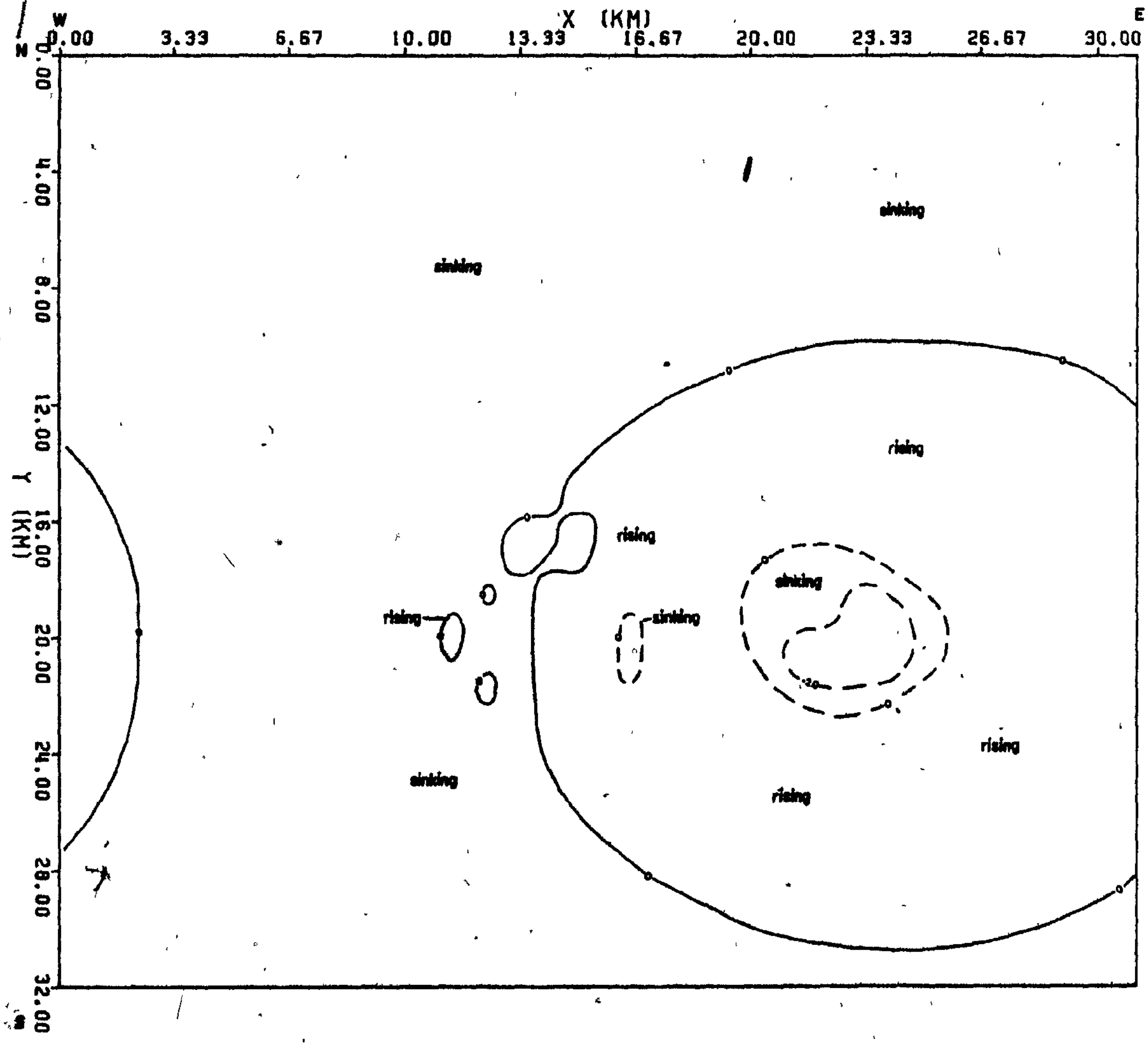

Figure 17g. Horizontal (x-y) section of vertical velocity (w) at 31 minutes and at z = 2.25 km. Regions of updraft are contoured with solid lines while dashed lines are used to indicate downdraft regions.

indicated by a plus sign (+), are 2.35 g kg^{-1}. The updraft maximum has risen to the level of the ice/snow maxima. Just below the ice cap is the center of maximum cloud water (1.85 g kg^{-1}). Ice crystals nucleated near this area rime substantial amounts of available cloud water and are advected along with cloud water by the strong updraft above the - 35°C level. The cloud water is immediately frozen (isobarically) and added to the ice/snow content to create the ice cap. Small amounts of graupel and rain are also advected into the ice cap. Precipitation has reached the surface in the form of both rain (from melted graupel) and graupel ("heavy graupel"). The rain maximum, 1.6 g kg^{-1}, at the surface corresponds to a rainfall rate of approximately 33 mm hr^{-1}. The in-cloud and surface maxima for graupel at this time have reached their maximum values of 2.9 and 1.45 g kg^{-1} respectively, as quoted above. Note the major area of graupel formation, growth, and fallout, all near the central (updraft) axis of the essentially vertical storm. Note also the depletion of cloud water below the area of maximum cloud water (the -35°C level) by the riming of ice particles.

The radar structure/flow in the x-z plane is shown in Figure 17b. The region of maximum reflectivity near the center of the storm is associated with the major area of graupel growth. The reflectivity contours now extend to the surface in connection with the rain and graupel fallout. The point of maximum reflectivity is 62 dBz in the central region inside the cloud with two local maxima located below it in the center of the precipitation "shaft". Referring to both Figure 17b and the y-z vertical section 17c, the radar overhang on the southeast side of the storm is still evident. A small cell has now formed on the north side (Figure 17c) of the main development in response to a weak oscillation in the updraft evident in this plane.

The vector flow field shows the updraft region in the cloud above the 0°C isotherm with the region of maximum updraft in the top section of the storm. A slight divergent flow results (Figure 17b) at the storm top as the updraft hits the tropopause. However, the divergence is too weak and the mixing of dry air too strong (which encourages sublimation of the ice/snow) to create an "anvil", a common feature of most storms which reach the tropopause. Below the 0°C line is the precipitation-induced downdraft which diverges at the surface, creating small circulation cells which can be seen on the west and north sides of the storm. The main updraft core is essentially cut off from the surface by this downdraft and is thus mainly fed by the westerly "jet". This "jet", along with the continued weak surface flow from the southeast, continues to maintain the radar overhang. The high reflectivity gradient on the west (inflow) side is still evident.

The effect of evaporation and mixing at the cloud edges produces a slight sinking motion (from evaporative cooling) particularly evident on the inflow side where the strongest mixing occurs. The outflow on the western edge of the ice cap, which results from the upper-level divergence referred to above, combines with cooling/subsidence from sublimation on this edge to produce a circulation cell, evident in Figure 17b.

The horizontal sections in Figures 17e and f show radar reflectivity and flow at the surface and 2.3 km level respectively. At the surface, the maximum reflectivity, corresponding to the point of maximum surface graupel content, is 57 dBz and is located directly below the upper center of maximum updraft (i.e. on the same axis). The surface outflow (from the precipitation-induced downdraft) deflects the low-level environmental flow around the slightly elliptically-shaped precipitation zone, while higher up (Figure 17f), flow from the northwest continues to flow into the storm (note the convergence), compressing reflectivity contours on the inflow side and maintaining the overhang on the opposite side.

Figure 17d shows the θ' and π_p' fields in the x-z plane. The pattern has become quite complex at this intense stage of the storm's development. The surface low, still evident in Figure 16a, has now been completely replaced by the precipitation-induced dome of high pressure. Cooling at the surface, from evaporation and melting of precipitation, is also evident. Maximum cooling (θ'_{min}) reaches -4.0°C. Areas of warming can still be found in the clouds with cooling near the cloud edges due principally to evaporation. The large region of cooling in the upper ice cap (9 to 11 km height) is probably due to oscillations aloft.

The vertical velocity field in a horizontal plane at 2.3 km, the same level as Figure 17f, is shown in Figure 17g. The region of sinking motion within the center of the circular zone of rising air represents the precipitation-induced downdraft. To the left of this main core of sinking air, successive regions of rising and sinking reflect the oscillation of the updraft and the small cloud on the west side of the storm.

5.2.6 30 - 45 minutes

The intensity of the storm begins to diminish shortly after the 31-minute mark. The updraft maximum, which begins to decrease in magnitude, reaches its maximum height (9 km) at 33 minutes and then falls rapidly to the 7 km level (Figure 13). The maximum graupel content at the surface, $QGSFC_{max}$, plotted in Figure 13, begins to decrease as well. However, a substantial amount of graupel above the 0°C isotherm continues to melt, maintaining the rainfall at the surface (indicated by $QRSFC_{max}$). The maximum rain content at the surface reaches a peak value of 1.74 g kg^{-1} at 33 minutes and begins to decrease after 40 minutes. The precipitation-induced downdraft $|w_{minp}|$ follows a similar pattern, reaching a maximum value of 5.8 m s^{-1} at 34 minutes and then slowly diminishes at a much slower rate than w_{max}. By 40 minutes, $|w_{minp}|$ becomes larger than w_{max}.

Referring to Figure 12, it can be seen that by 40 minutes, all forms of condensate are being depleted faster than they are being produced. The cloud water is depleted at the fastest rate, due to continued evaporation, riming and glaciation and the termination of the condensation process. Rain continues to be produced by melting graupel, but increasing evaporation and fallout deplete the rain content at a fast rate. Nucleation of ice/snow has terminated and deposition onto the existing ice/snow crystals is outweighed by the sink processes of conversion, sublimation and melting. All processes involving supercooled rainwater, which is completely depleted, are totally inactive. The only significant source of graupel left is conversion from ice/snow with melting the main sink, resulting in a decrease of the entire graupel content. By 45 minutes, the melting of graupel becomes the most active process.

5.2.7 Sections at 46 minutes -- dissipating stage

Figure 18a shows the x-z vertical section through the storm near the end of the simulation as the storm is dissipating. Notice the few remaining areas of cloud, which contain only small quantities of cloud water. Graupel, rain, and ice now comprise the bulk of the storm. Conversion of ice/snow to graupel has diminished but continues to maintain the center of

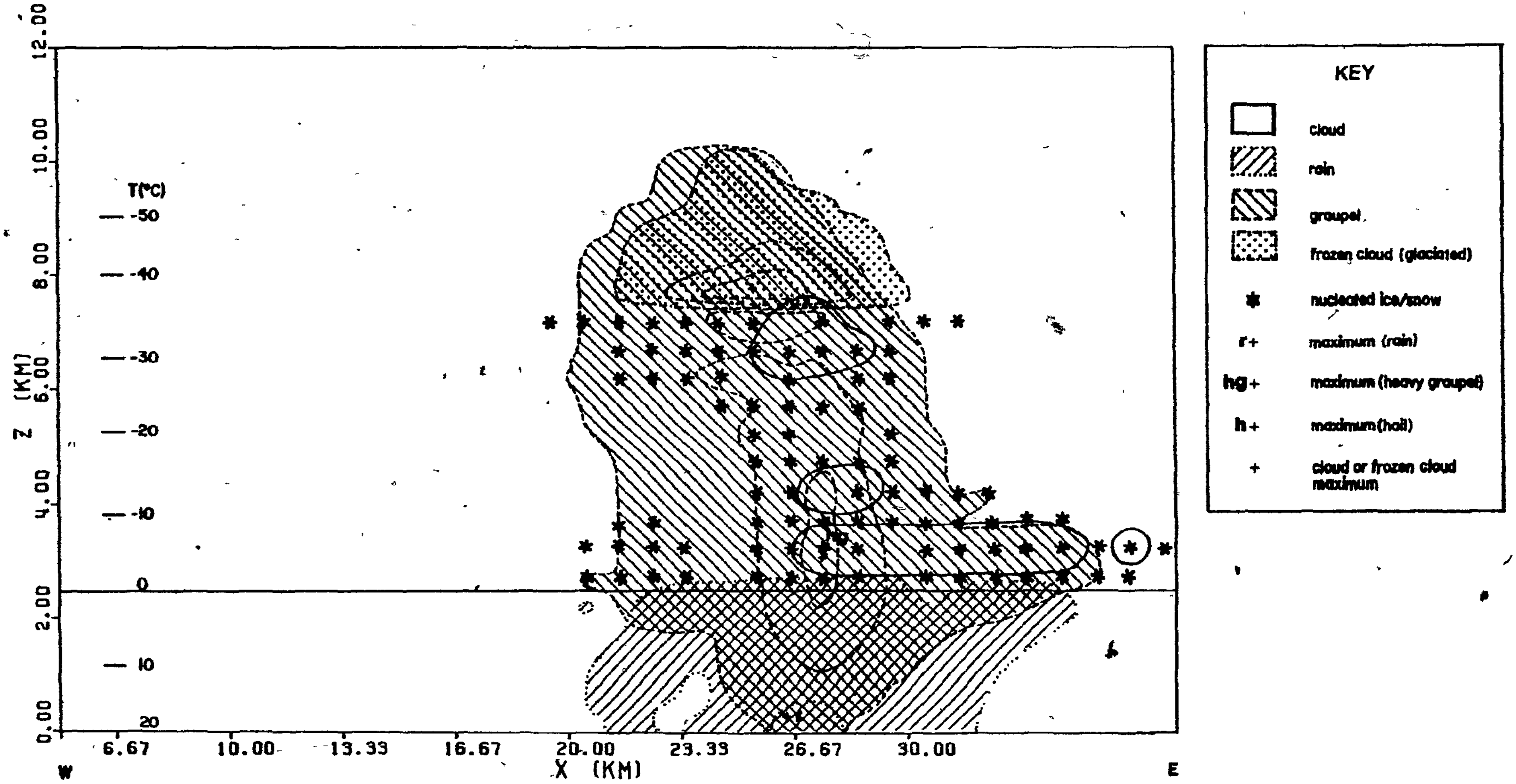

Figure 18a. Same as Figure 15a, except at 46 minutes (dissipating stage) and taken at y = JMAXW = 23 km. Note that the x-axis does not begin at 0 km, as the storm has moved into the next domain.

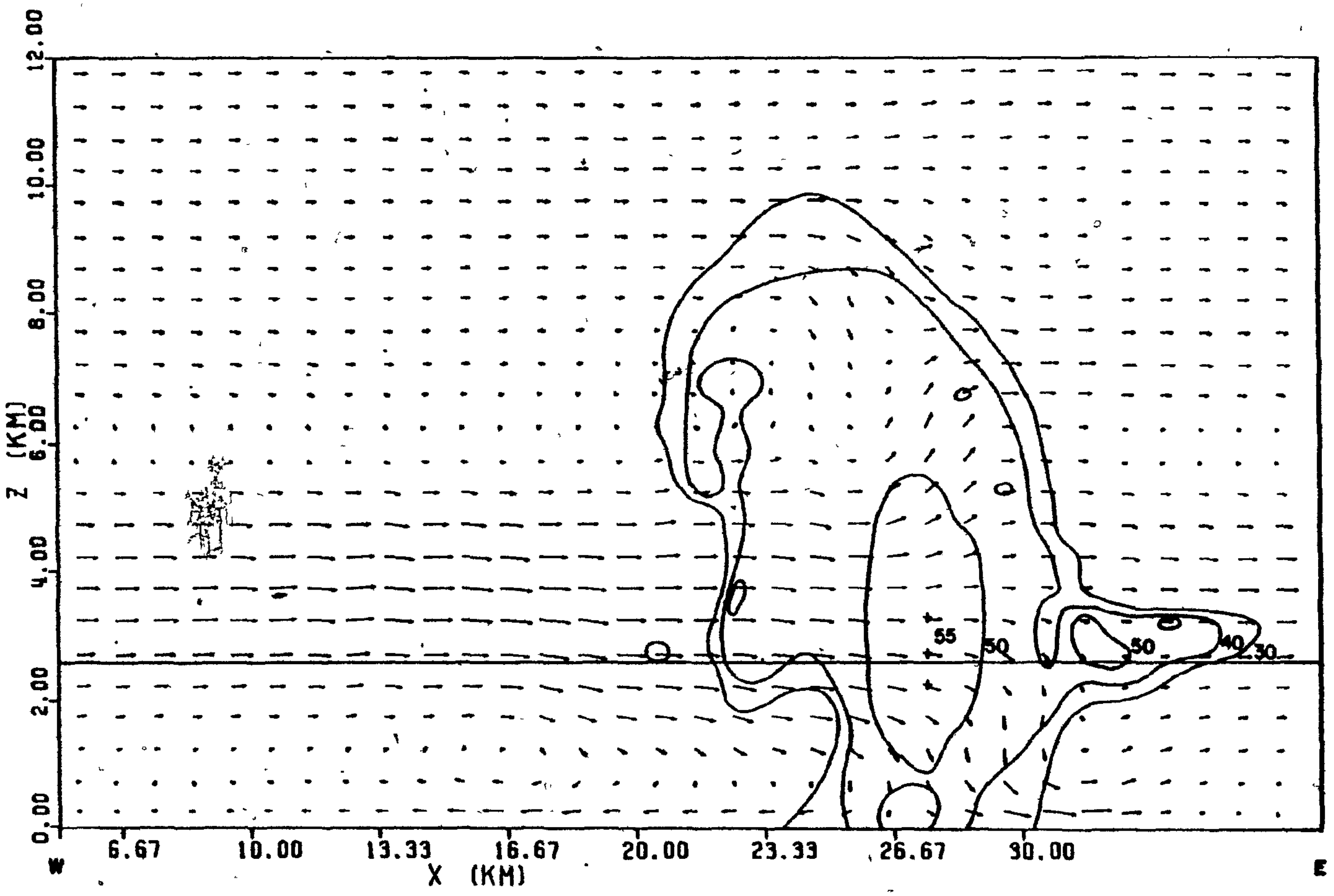

Figure 18b. Same as Figure 15b, except at 46 minutes and taken at y = JMAXW = 23 km. The magnitude of the longest vector is 7.9 m s^{-1}. Note that the x-axis does not begin at 0 km, as the storm has moved into the next domain.

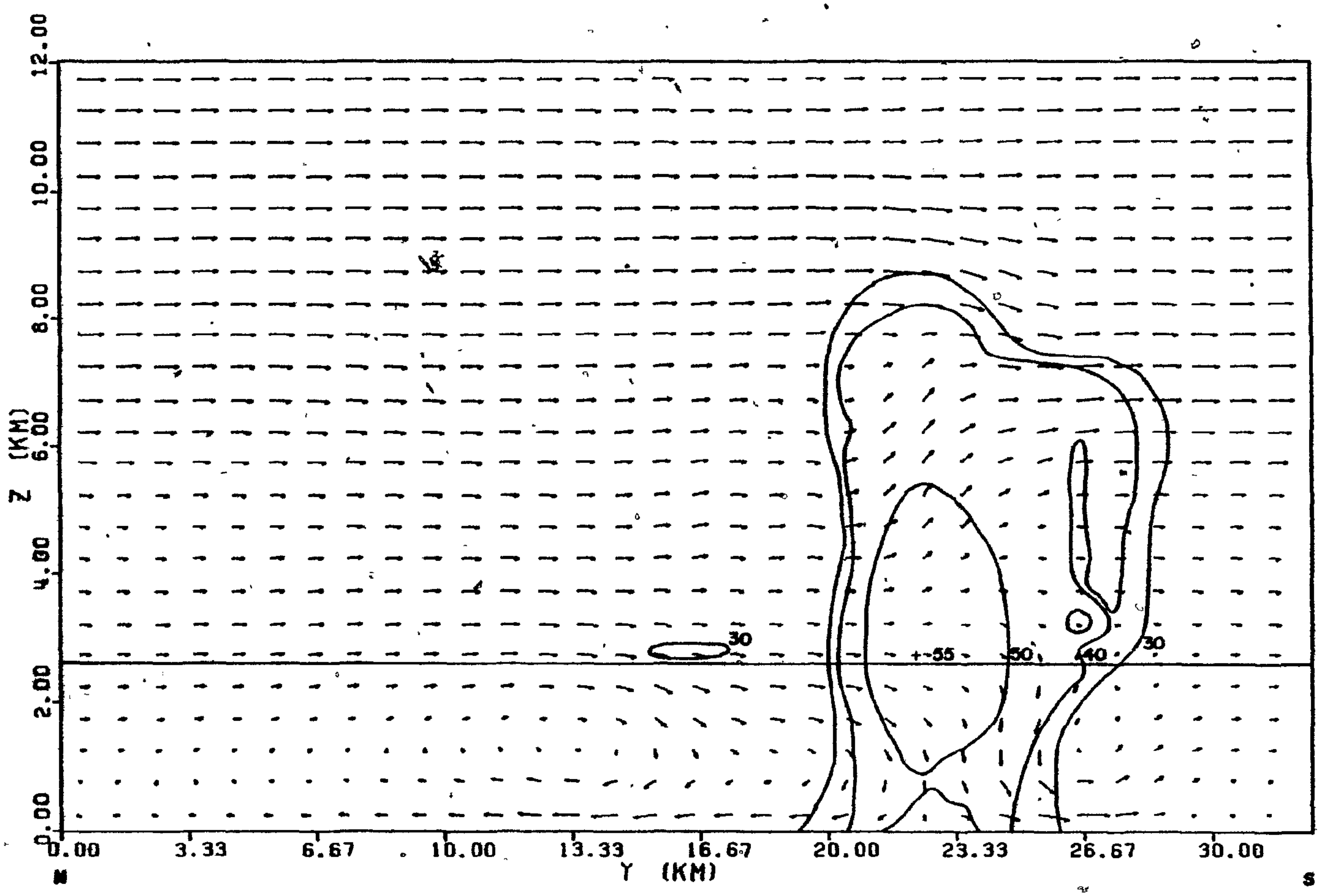

Figure 18c. Same as Figure 15c, except at 46 minutes and taken at x = IMAXW = 27 km. The magnitude of the longest vector is 7.6 m s^{-1}.

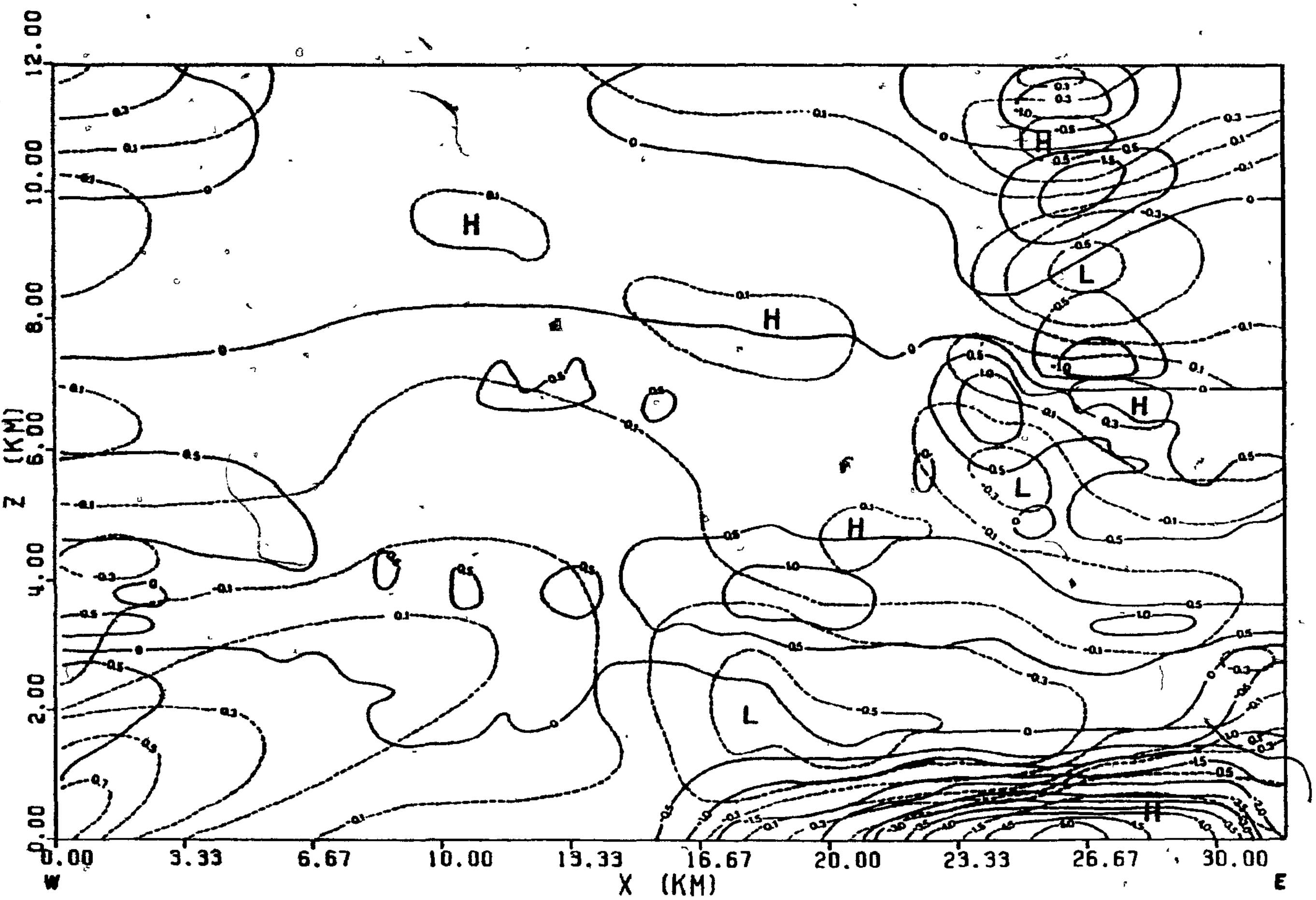

Figure 18d. Same as Figure 15d, except at 46 minutes and taken at y = JMAXW = 23 km. π_p' contours greater than 1.5 near the surface were too closely spaced to indicate as $\pi_p'_{max}$ (H) was 2.8 (x 10^{-4}).

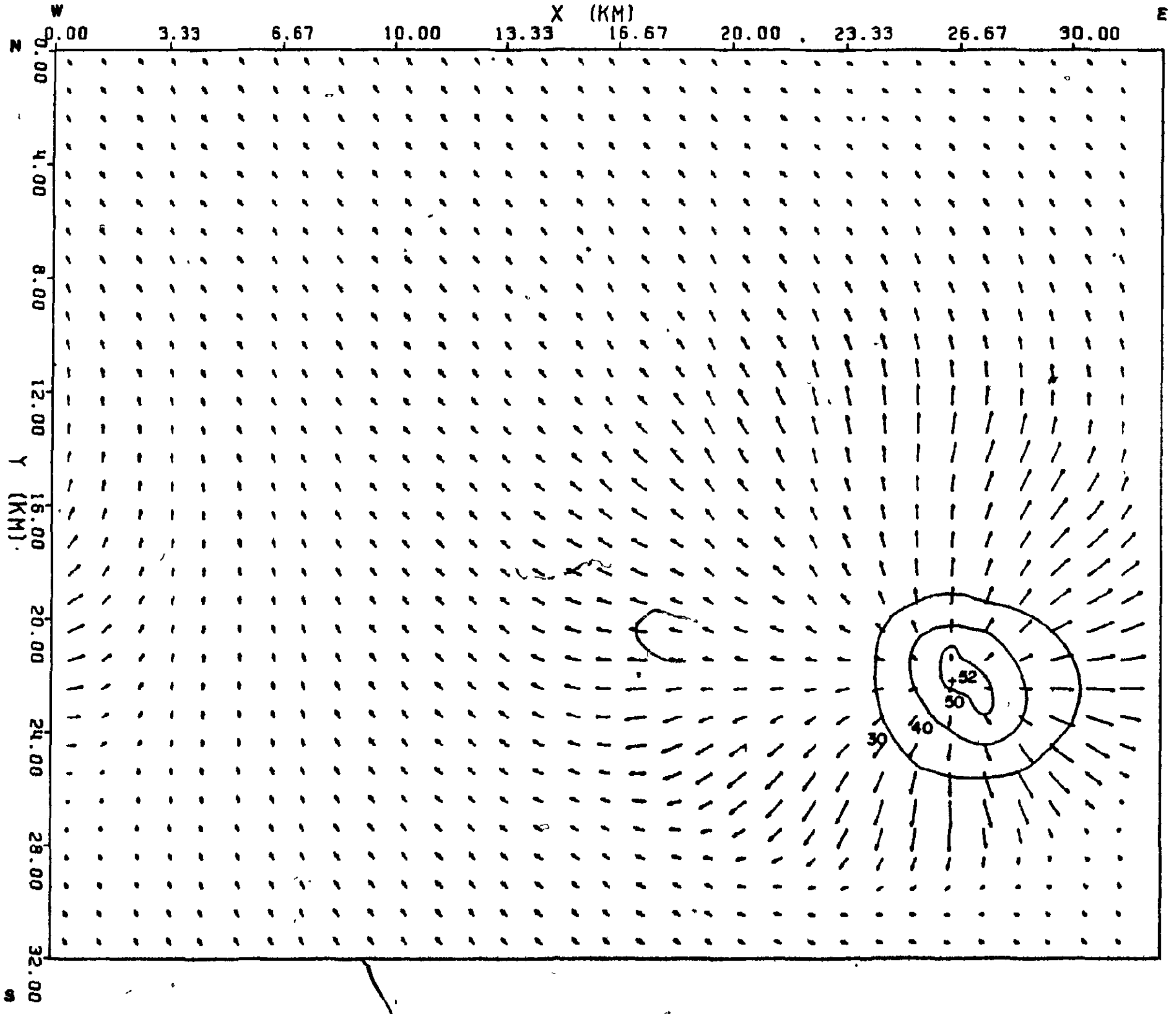

Figure 18e. Same as Figure 15e, except at 46 minutes and at z = 0.25 km. The magnitude of the longest vector is 8.2 m s^{-1}.

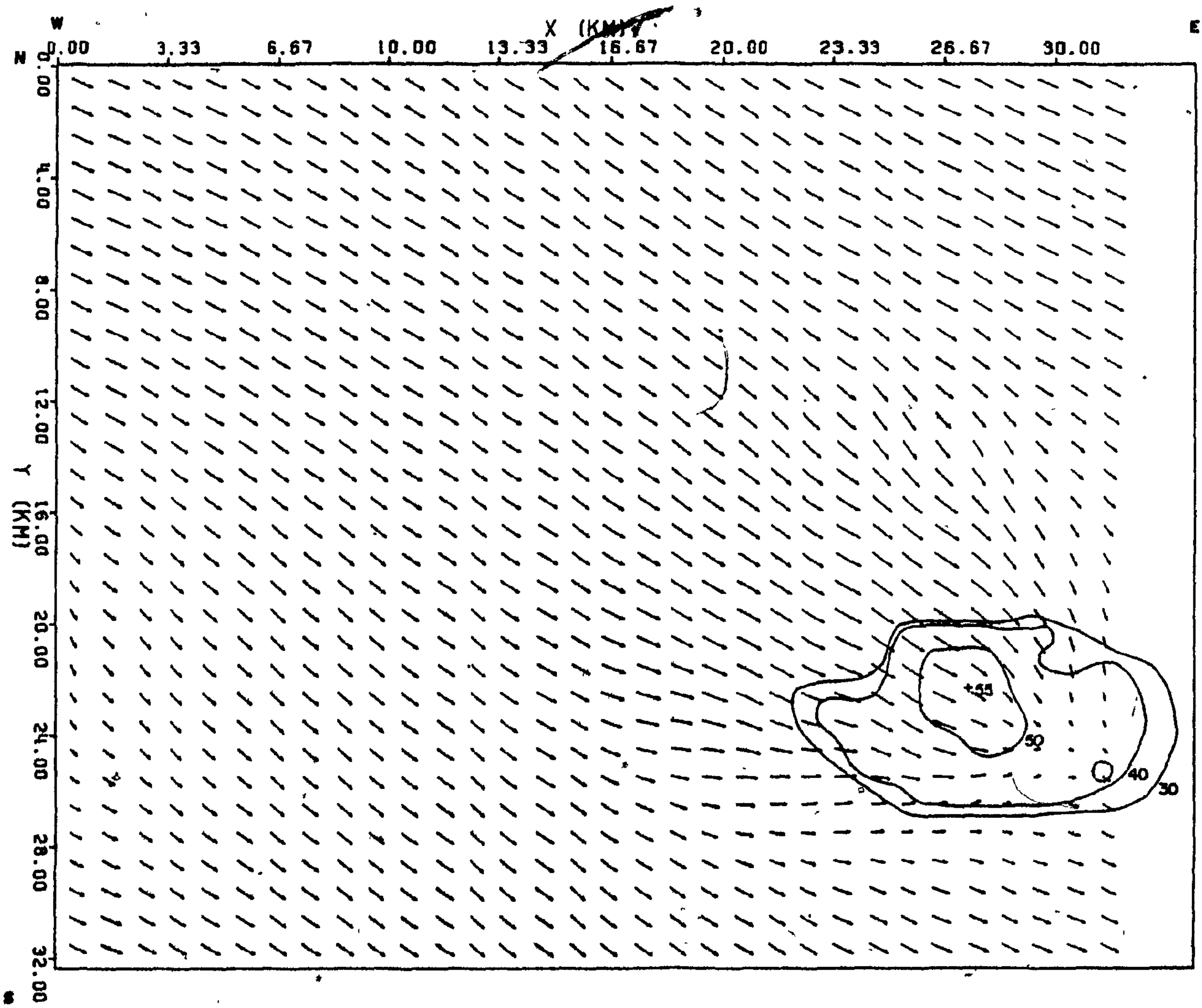

Figure 18f. Same as Figure 15e, except at 46 minutes and at $z = 2.25$ km. The magnitude of the longest vector is 6.9 m s^{-1}.

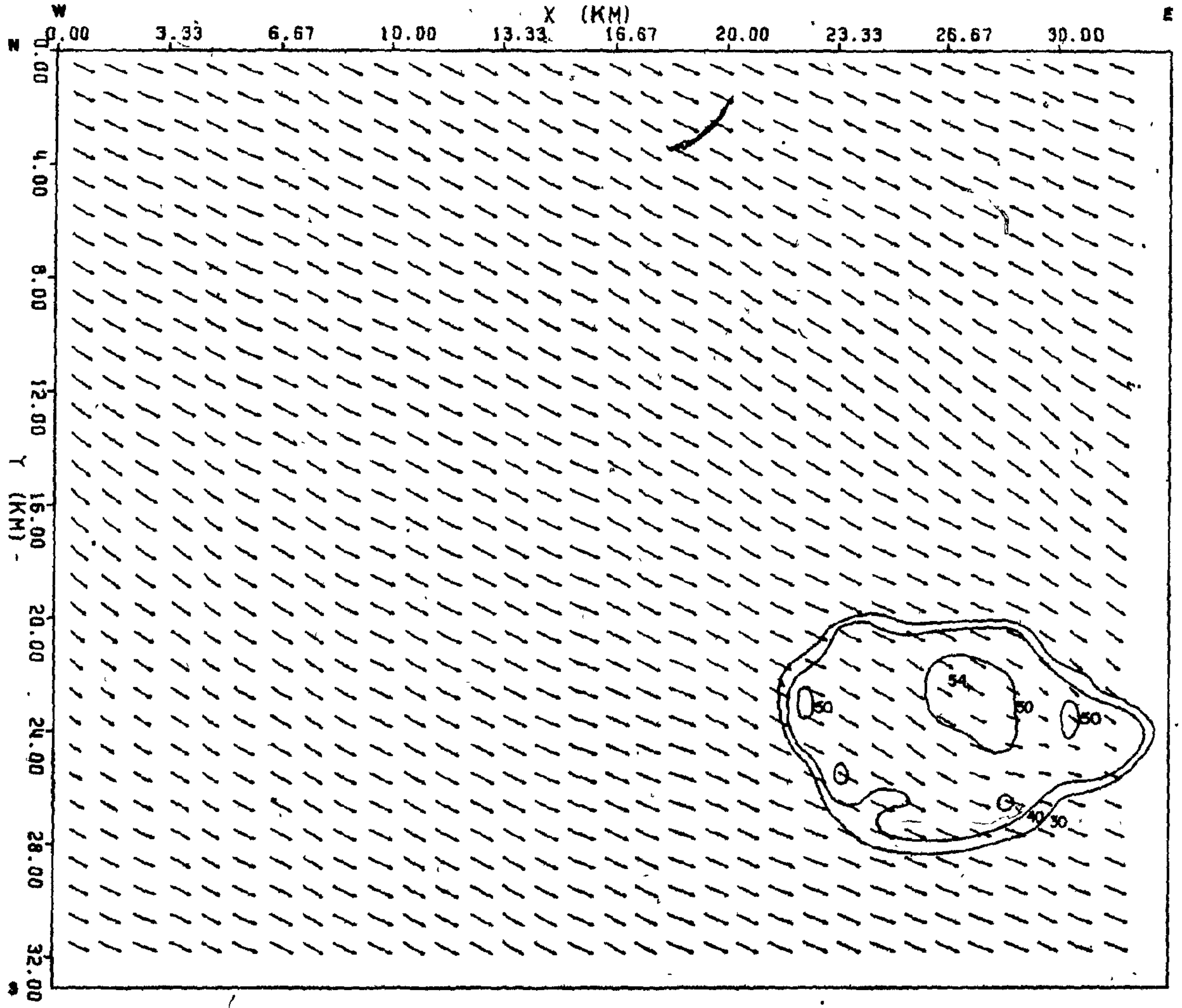

Figure 18g. Same as Figure 15e, except at 46 minutes and at z = 3.75 km. The magnitude of the longest vector is 8.34 m s^{-1}.

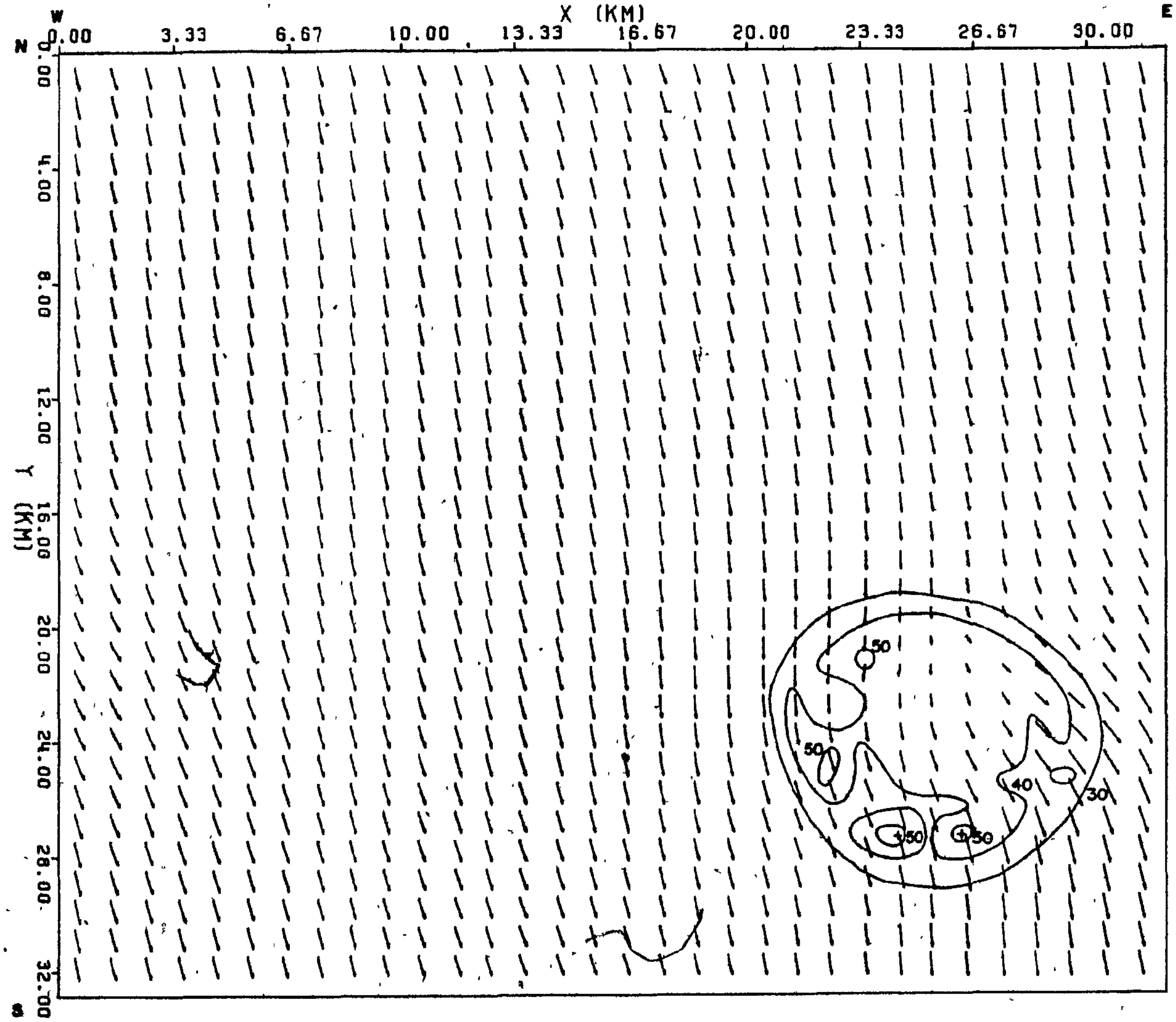

Figure 18h. Same as Figure 15e, except at 46 minutes and at z = KMAXW = 6.75 km. The magnitude of the longest vector is 7.4 m s^{-1}.

maximum graupel content (1.17 g kg^{-1}), now representing "heavy graupel", above the 0°C isotherm. Melted graupel continues to fall as rain and the maximum rain content is still located at the surface (1.13 g kg^{-1}). The small cell which followed the storm on its west flank has merged with the main storm, which has penetrated the eastern edge of the domain (and moved into the adjacent domain corresponding to the lateral boundary conditions). The top of the storm remains quite high (10.5 km) and the ice cap is slowly dissipating.

The corresponding reflectivity and flow are shown in Figure 18b. Some subsidence is noticeable in the upper regions of the storm while the precipitation continues to maintain a substantial downdraft and outflow near the surface. There is no region of substantial updraft evident at this time ($w_{max} = 3$ m s^{-1}). The westerly flow moves through the region of maximum reflectivity (graupel content) and maintains the overhang on the east side of the storm. The outflow below the freezing level has obliterated the surface inflow from the southeast. The wind shear in this plane has tilted the storm to the west, although the core of the storm, represented by the region of reflectivity greater than 50 dBz, remains vertical.

Some differences between the x-z (W-E) section, Figure 18b, and the y-z (N-S) section, are indicated in Figure 18c. As a result of weaker flow and shear, the storm in the y-z plane (18c) appears more vertical and lacks a substantial overhang. Also, no smaller cell has merged with the storm in this plane as in the x-z plane (which widened the storm in that plane).

The horizontal sections at the surface, 2.25 km, 3.75 km and 6.75 km (Figures 18e,f,g and h respectively) further illustrate the features mentioned above -- the large area of outflow at the surface, the radar overhang on the east side, the extension of the storm on the west side from the merging cell, and the verticality of the storm core.

Figure 18d shows the flattening surface high pressure and cooling area spreading out with a maximum dimensionless pressure perturbation of 2.8×10^{-4} and a maximum cooling (θ'_{min}) of -5.04°C at about 27 km in the x-direction. As there are few latent heat-releasing processes still in operation, few areas of strong warming can be found. On the upper-right-hand side of the diagram, the oscillation with height of the π_p' and θ' fields, which are approximately 90° out of phase, extends to the top of the domain. This phenomenon is often found in or near a stable layer such as exists at this height.

5.2.8 45 - 52 minutes

In the last seven minutes of the simulation, the storm continues to decay. Figure 12 shows that the total cloud water content has greatly diminished by 50 minutes. Graupel, although diminishing as well, comprises the majority of the total condensate (46%) with ice/snow, rain, and cloud comprising 32%, 21% and 0.18% respectively. The only processes still active are mostly depletion terms -- evaporation, sublimation, and melting. The processes most important in the water budget and distribution for the run were melting of graupel and condensation, while the least important were nucleation (important initiator of ice/snow, however) and Bigg's freezing. Table 2 summarizes the main initiating processes, sources and sinks for each type of condensate.

Table 2

Condensate	Main Initiation Process(es)	Main Sources	Main Sinks
cloud water	condensation	condensation melting snow	evaporation glaciation riming by graupel
rain	autoconversion melting graupel	melting graupel	contact freezing (early) evaporation } (later) fallout
ice/snow	nucleation glaciation	deposition riming	conversion to graupel sublimation
graupel	conversion from ice/snow	riming conversion	melting fallout

To conclude this chapter, the vertical velocity profile with height, $w(z)$, at different times in the storm's development, will be examined. Figure 14 shows $w(z)$, taken along the axis containing w_{max}, at five different times. At 10 and 21 minutes, in the developing stage of the storm, the updraft maximum rises and increases in magnitude. Along the entire vertical axis, there is mainly updraft. By 31 minutes, the maximum updraft is near its maximum magnitude and height with updraft extending high to 10.7 km and down to the 0°C level (about 2.7 km). Below the 0°C level a strong downdraft has formed due to the fallout of precipitation isolating the updraft from the surface. Near this time, the precipitation at the surface reaches its maximum intensity. The profiles at 43 and 52 minutes show the slow descent of w_{max} and the decrease in the maximum downdraft at the 1 km level as the storm decays.

CHAPTER 6

DISCUSSION

In this chapter, the results of the 3D simulation presented in the previous chapter will be compared to the observed storm outlined in Chapter 4. Also, the 3D run will be compared to a 2D run to illustrate the important effects of including the third dimension in a numerical simulation of a storm. The performance of the microphysical parameterization of graupel in the model will be examined and improvements will be suggested which might lead to better agreement with observations.

6.1 Comparison with observed storm

The reflectivity structures at the three stages of the observed storm presented in Chapter 4 will be compared with those of the three corresponding times in the simulation.

6.1.1 Growing stage (Figures 7 and 8 and Figures 15b, c, e and f)

It is difficult to compare the radar reflectivity structure of the observed storm (Figure 7) with the model results (Figures 15b, c, e and f) during this early stage. As indicated in Figure 7, the remains of the previous cell are still evident on the eastern (right) side of the new cell, particularly evident in Figures 7a and 7c. The region of remaining precipitation from the decaying cell, located near the surface, is connected to the region of new precipitation formation and growth higher up in the new cell. Only those portions of the echoes connected with the newly developing cell will be considered in the following discussion while the small adjacent cloud in the model results (Figure 15b) will be disregarded, as there is no counterpart in the observation. Recall that the model y-z (north-south) vertical cross-section (Figure 15c) corresponds to the observation vertical cross-section normal to the direction of storm motion along line CD (Figure 7c) except that each is reversed with respect to the other (because north is to the left in Figure 15c and to the right in Figure 7c). In other words, the right-hand flank (RH) on the left side of Figure 7c actually corresponds to the right side of Figure 15c.

One of the similarities between the observed and model reflectivity structures is the evidence of an overhang on the southeast side of the storm. A notch-shaped unbounded weak echo region (UWER) is located under the overhang in the observed storm, but is not evident in the model storm. From Figure 7a, it appears possible that the overhang and UWER (evident at the 2° elevation) are simply due to the remnant of the dying cell. However, assuming that the overhang and UWER are genuine, they are caused by a strong surface updraft/inflow (see Figure 8) according to Chisholm's WER hypothesis (see Chapter 2). In the simulation, though, the overhang is simply caused by the blowing out of precipitation particles by the westerly mid-level inflow over the area of weak surface updraft inflow. Note that Chisholm, in Figure 8, does not indicate a mid-level inflow. In any case, the UWER is the smallest and shortest-lived encountered by Chisholm in his case studies of several hailstorms and soon disappears (although an overhang remains). The overhang, which is most obvious in the model storm at later times, is an often-reported feature of storms (for example, the Wokingham storm reported by Browning and Ludlam, 1960) and appears as well in the 2D simulation of Orville and Kopp (1977) for reasons similar to those given above for the model overhang.

The observed maximum reflectivity (over 65 dBz) is found near the top of the storm at 5 km in Figure 7b and lower down, near 4 km height, in Figure 7c, while in the model storm, the maximum reflectivity (59 dBz) is located near the center of the storm in the updraft core at the 4 km level in each section, and is smaller in magnitude. Precipitation has not yet reached the surface in the model simulation but does so two minutes later. Both observed and model storms have storm tops, defined as the maximum height of the 35 dBz contour, near 6 km.

Comparison of the horizontal radar structures is very difficult due to the interference from the decaying cell (Figure 7a). However, there appears to be some similarity in the echo outlines of Figure 7a (3° or 3.5 km elevation) and Figure 15f (4.75 km level).

6.1.2 Mature stage (Figure 9 and Figures 17b, c, e and f)

The model and observed storms at the mature stage are similar in several respects. It should be remembered that the scale of the horizontal axes (x and y) is not the same as that of the vertical (z) axis in Figures 17b and c due to the difference in resolution, while the scales are equal in Figures 9b and c. Equalizing the vertical to the horizontal scale in Figures 17b and c would give the model storm a vertically compressed, squat appearance, more like the observed storm in Figures 9b and c.

The radar overhang, or bulge on the southeast side of each storm, is still evident. The observed storm has grown to a height of 7 km, is wider in the direction of storm motion (Figure 9b), and has a large area of precipitation at the surface -- 9 km wide in the direction of motion. Some remaining precipitation from the previous cell may still be contributing to low-level reflectivity. The model storm top has reached 9.5 km while the precipitation area at the surface is smaller and more circular than that of the observed storm, roughly 6 km wide in the x direction. The maximum reflectivity in the observed storm is higher (>65 dBz) than that of the model storm (62 dBz) and the region encompassed by the 65 dBz contour in the observed storm covers a large area, equivalent to the area enclosed by the 50 dBz contour in the model results.

Other similar features include the verticality of the storms and high reflectivity gradients on the mid-level inflow side with weaker gradients on the opposite (overhang) side (most evident in Figures 9b and 17b). The maximum model storm width (10 km) agrees well with observation. Reflectivity values at the surface are greater than 65 dBz for the observed storm, but only greater than 50 dBz for the model storm with several zones of higher reflectivity (>60 dBz) located between the surface and the 6 km height. The level of the point of maximum reflectivity is slightly lower in the lower model storm, indicating that perhaps Figure 9 represents a more advanced, dissipating stage (i.e. later than the time of maximum updraft).

6.1.3 Dissipating stage (Figure 10 and Figures 18b, c, e, f, g, h)

Both observed and model storms are now decaying, although their reflectivity structures have become quite dissimilar. The appearance of the observed storm at this time (Figures 10b and c) indicates a more "classical" dissipation. The storm top has fallen to 5 km and has flattened out. The region of maximum reflectivity (>65 dBz) has descended to the surface as the last of the heavy precipitation falls out (the remaining updraft, if any, is too weak to support the remaining precipitation, while precipitation formation and growth have ceased). There is a large area of low reflectivity gradient and the overhang on the right side in Figure 10b is less evident. Note the small bulge in the storm top (on the right in Figure 10b) enclosing a reflectivity maximum, and two more maxima are present at lower levels. The storm in the vertical plane perpendicular to the storm motion (Figure 10c) appears "pinched" around the 2 km level and is much narrower and more vertical in this plane.

In contrast, the model storm depicted in Figures 18b and c still has a tall, rounded top at about 9 km (which eventually descends to 7.8 km at 53 minutes). Although the maximum vertical velocity for the storm has decreased to only 3 m s^{-1}, updrafts still extend quite high into the storm, with w_{max} between 6 and 7 km in height. This, combined with the continued conversion (at a reduced rate) of ice/snow to graupel at higher levels, maintains the main region of reflectivity ($Z_e > 50$ dBz) above the surface and covering an extended depth in the atmosphere. There is, however, a smaller area of $Z_e > 50$ dBz at the surface evident in Figures 18b and c.

The model storm in the x-z plane (Figure 18b) still has an overhang on the east side, which contains a reflectivity maximum. The "overhang" on the west side is caused by the incorporation of the precipitation from the smaller cell and thus has no counterpart in the observed storm (Figure 10b). The y-z vertical section of the model storm (Figure 18c) shows no mid-level "pinching" of the contours as in Figure 10c, but the storm is narrower and more vertical in this plane than in the x-z plane (Figure 18b).

Similar differences between the model and observed storms are also evident in the horizontal sections (Figure 10a and Figures 18e, f, g, h). The precipitation area at the surface in the model is smaller and more circular than the elongated, elliptical zone of surface precipitation associated with the observed storm. At higher levels, though, both observation and model results indicate rather elliptical patterns of radar reflectivity with the major axis oriented closer to the direction of storm motion.

It appears, then, that at this time, as at 31 minutes, the observed storm is at a later stage of dissipation than the model storm. If this is the case, the simulation could be extended past 53 minutes to provide sections at later times which might compare better with observations of decaying storms. Another possibility is that the dissipation process in each storm was different. This could be due to the microphysical parameterization or other factors discussed later which might lead to significant differences between the model and observed storms.

The observed storm produced hail at the surface between 0.5 cm (pea size) and 2.0 cm (grape size) in diameter, while the mean graupel diameter produced by the model at the surface was only 0.195 cm. Possible reasons for this difference are discussed later.

6.2 General comments and additional comparisons

In general, the model managed to simulate a realistic hailstorm with features found in both observed storms and other numerical cloud models. The features which agreed with the observed storm have been mentioned above --

the overhang, certain aspects of the reflectivity contours and the vertical structure of the storm. There are other features as well, which cannot be compared with the observed storm (as the data was not available), that were well-simulated. Among these are the important microphysics-dynamics interactions such as the influence of the condensate and the associated phase-change processes on the flow, pressure and temperature fields. For example, the evaporative cooling, downdraft, and surface high pressure in connection with the falling precipitation were realistically simulated. The vertical velocity profiles generated in the simulation, with the updraft eventually overlying the downdraft, were similar to those found in actual storms and used in simple 1D (kinematic) cloud models.

Many of these model features were also found in the two-dimensional simulation of a hailstorm by Orville and Kopp (1977), referred to in Chapter 2. Among these were a substantial overhang, evaporative cooling and the orientation of the updraft and downdraft. The breakthrough of a mid-level inversion in their sounding, as in the present study, proved to be an important turning point in the development of the storm. Their simulation as well failed to produce a weak echo region (WER).

One of the goals of this research was to give added realism to a numerical simulation of a hailstorm by using three dimensions. To see the effect of the third dimension, the 3D run will now be compared to a 2D run which used the same data (i.e. the only difference was its two-dimensionality).

6.3 Comparison with a 2D run

Figures 17b and 19 show equivalent vertical cross-sections of radar reflectivity and flow (in the x-z plane) for the 3D and 2D simulations respectively at 31 minutes. Both storms developed in a similar manner,

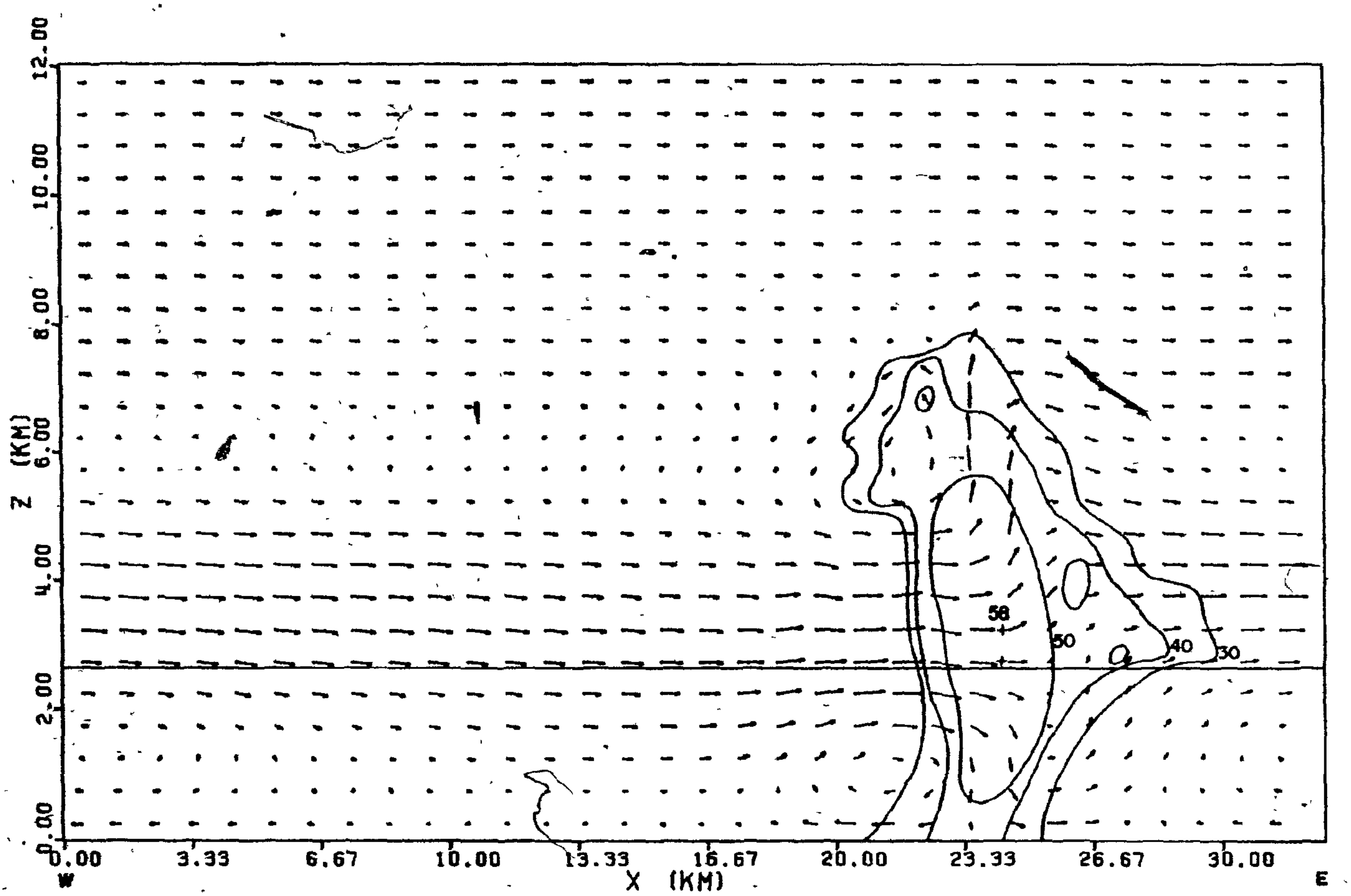

Figure 19. 2D simulation vertical (x-z) section of radar reflectivity (contours labeled in dBz) and flow at 31 minutes (at y = 0). Solid horizontal line is the 0°C level. The magnitude of the longest vector is 9.1 m s^{-1}. The effect of restricting the simulation to two dimensions can be seen by comparing this figure to Figure 17b.

both being essentially vertical, moving in a southeasterly direction, and exhibiting the radar overhang on the east (outflow) side and a high reflectivity gradient on the opposite (inflow) side. However, the 2D storm is smaller than both the 3D and observed storm and less vigorous, reaching only 7.5 km (closer to the observed storm top) compared to 9.5 km for the 3D storm. Maximum vertical velocities in the 2D storm reached only 7.1 m s^{-1} at 28 minutes and at 5.8 km height while the maximum for the 3D simulation occurred at a similar time, but was higher (7.8 km) and more than twice the magnitude (14.4 m s^{-1}), a more realistic value. (Chisholm, using a loaded moist adiabatic (LMA) parcel theory, calculated w_{max} to be 16.4 m s^{-1} for the sounding used.) This difference had a large influence on several important storm features and parameters in the 2D simulation. For example, there is only a slight oscillation in the flow and no correspondingly small cell is evident in Figure 19. The 3D storm was able to penetrate the -35°C (glaciation) level, creating a substantial ice cap and thereby releasing latent heat high in the storm, allowing the storm top to reach a high level. The 2D storm, however, was not able to significantly penetrate the level of glaciation.

The connection between the maximum updraft (w_{max}) and the graupel/hail size (or content) at the surface has been mentioned in Chapter 2 with reference to the work of Danielson <u>et al</u> (1972) and Dennis and Musil (1973). A strong updraft creates more liquid condensate which, along with the ice content, is suspended for a longer time aloft, allowing ice/snow and graupel to grow to larger sizes through liquid water accretion before they become heavy enough to fall through the updraft. There appears to be a definite connection between w_{max} and the maximum graupel (and rain) content at the surface in both the 2D and 3D runs. In both runs, the maximum graupel and rain contents at the surface (and hence the maximum graupel mean diameter $\overline{D}$) occurred near or at the time of w_{max} (see Figure 13 for the 3D run). Also, the point at the surface where the graupel maximum occurred was located directly below the point of w_{max}. The 3D storm, with $w_{max} = 14.4$ m s^{-1}, produced a maximum graupel content at the surface of 1.45 g kg^{-1} ($\overline{D} = 0.195$ cm) while the 2D storm, with $w_{max} = 7.1$ m s^{-1}, only produced graupel of 0.25 g kg^{-1} ($\overline{D} = 0.01$ cm) maximum content at the surface. The maximum rainfall rate at the surface was 36 mm hr^{-1} for the 3D run and only 21 mm hr^{-1} for the 2D run. Thus the third dimension is seen to give a higher, more realistic w_{max} which affects the maximum precipitation content and size.

In conclusion, although the 2D storm was closer to the maximum height of the observed storm, the 3D simulation produced a larger, more vigorous storm which came closer to simulating such important (observed) storm features as storm width, maximum radar reflectivities, and maximum graupel size at the surface.

Table 3 summarizes the comparison of the features of the observed storm, the 2D storm, and the 3D storm.

Table 3

Feature	Observed Storm	2D Run	3D Run
Motion	southeast	southeast	southeast
Max. horiz. dimensions (length x width)	10 km x 6 km	8 km	10 km x 8 km
Max. storm top (35 dBz) and temp.	7.8 km (-37°C)	7.5 km (-35°C)	9.5 km (-50°C)
Orientation	vertical	vertical	vertical
Cloud base height and temp.	2.1 km (3.1°C)	2.3 km (3.5°C)	2.3 km (3.5°C)
Max. cloud water	--	1.5 g kg^{-1}	1.8 g kg^{-1}
Max. graupel content	--	1.6 g kg^{-1}	2.9 g kg^{-1}
-- at surface	--	0.25 g kg^{-1}	1.4 g kg^{-1}
Max. graupel diameter (and type)	--	0.19 cm (hg)	0.2 cm (h)
-- at surface	grape (2.0 cm)	0.01 cm (lg)	0.195 cm (hg)
Max. rainfall rate	--	21 mm hr^{-1}	36 mm hr^{-1}
Max. radar reflectivity	65-79 dBz	58 dBz	62 dBz
Precipitation area and shape	63 km^2 elliptical	--	30 km^2 slightly elliptical
Max. updraft	16.4 m s^{-1} (calc. from LMA model)	7.1 m s^{-1}	14.4 m s^{-1}
Radar overhang	yes	yes	yes
Weak Echo Region (WER)	possible*	no	no

* very small and only evident in developing stage when previous cell interferes

6.4 Differences between model results and observation: possible reasons and suggested improvements

So far the emphasis has been on the similarities between the results of the 3D numerical simulation and the observed storm. In this section, the differences mentioned in Section 6.1 will be examined and improvements suggested. In the first part of this section, the microphysical parameterization of graupel will be critically examined while the second part will focus on reasons apart from the parameterization which could be responsible for discrepancies between model results and observation.

6.4.1 Microphysical parameterization of graupel

The method of modeling graupel in a cloud model ultimately influences the transfer rates (processes), the other forms of condensate (cloud, rain, and ice/snow), and the model storm features. It is natural, then, to examine the assumptions inherent in the graupel parameterization when investigating the failure of the model to simulate certain features of an actual hailstorm, and to suggest possible improvements.

Assumptions, sometimes gross, must be made when employing bulk water microphysics. As described in Chapter 3 (Section 3.2.3.1), graupel is assumed to follow an inverse exponential size (diameter) distribution, characterized by several distribution parameters (λ, N_{og}, N_{tg}) from which such "characteristic" parameters as mean mass ($\overline{m}$), mean diameter ($\overline{D}$), and fallspeed can be calculated. These parameters are then used to calculate the different graupel processes. Thus, for each grid volume, a distribution of many particles in that volume is represented by "mean" quantities and a set of slope parameters derived from the graupel mixing ratio. To specify the distribution at a point, one of the parameters (N_{og}, N_{tg} or λ) must be specified externally (set constant) and in the scheme used here, the total number concentration of graupel particles (N_{tg}) is specified. Of course, in a real storm, graupel particles do not follow an exact exponential distribution, but if they did it would be unrealistic to assume that one of the slope parameters would not vary with time. Thus, difficulties are encountered when a particular parameter is assumed constant. First of all, there is the problem of choosing a value for this parameter based, hopefully, on observation. Often, as is the case for graupel, there are few measurements of these parameters and the few available give different values for different storms. Faced with this dilemma, the best that can be done is to use an average value or a value appropriate for the storm to be modeled. In choosing the latter, the results can be made to be in better agreement with observation simply because an assumption was made based on the observation.

For example, in the scheme used here, N_{tg} was set to 10^{-4} cm^{-3}, the highest value in the ~~range of~~ values given by observation. From equations (22) and (23) it can be seen that for a given graupel content, the mean diameter $\overline{D}$ and mean mass $\overline{m}$ will be much smaller than those obtained if we had chosen a lower N_{tg} such as 10^{-6} cm^{-3} (still within the range of observed values). By choosing a high N_{tg}, the size and mass of the particles are being limited to low values. Quantitatively, using $N_{tg} = 10^{-4}$ cm^{-3} (high) and a graupel content of 3 g kg^{-1} at the 2 km level will give a mean diameter of 0.2 cm, while using $N_{tg} = 10^{-6}$ cm^{-3} (low) the same graupel content yields a mean diameter of approximately 1.0 cm. Of course, depending on the value of N_{tg} chosen, the representative fall velocity, radar reflectivity and graupel transfer rates would vary considerably as well. Thus it would seem that a high N_{tg} would be appropriate for modeling highly concentrated light graupel particles and a low N_{tg} would be more appropriate for representing more disperse, larger, heavier hailstones, as mentioned in Chapter 3. Both types of particles are present, however, in most hailstorms. Stephens (1979) attempted to model both graupel and hail in his "graupel" classification scheme (see Figure 2) by simply using different particle densities, but, by specifying a constant N_{tg}, he was essentially limiting himself to one or the other.

In addition to the assumptions inherent in choosing a value for N_{tg} is the assumption that N_{tg} remains constant. There are processes in nature that would tend to significantly alter N_{tg} as well as the graupel mixing ratio at a point. Such processes as melting and horizontal advection should reduce the number concentration of graupel particles by eliminating the smaller particles first while fallout of the heaviest particles should leave fewer (smaller) particles behind and perhaps increase N_{tg} at a point below.

One way to improve this aspect of the scheme would be to allow N_{tg} to vary. An obvious choice would be to change N_{tg} to a value appropriate for hail (10^{-6} cm^{-3}) when the mean mass ($\overline{m}$) puts the graupel content in the "hail" sub-class while using the higher value (10^{-4} cm^{-3}) for the "light" and "heavy" graupel sub-classes. This would give much higher fallspeeds, mean diameters, and reflectivities for the "hail" points, which should better simulate the observed storm reports of large hail. This was attempted but the results were not successful. This is because two different types of particles with very different characteristics were being modeled in the one "graupel" class. This meant that a "hail" point, with the associated high terminal fallspeed ($\simeq 30$ m s^{-1}), could be located directly above a point with a similar graupel mixing ratio but falling into the "heavy graupel" sub-class with a much lower fallspeed ($\simeq 10$ m s^{-1}). When the program attempted to vertically advect the graupel content, the discontinuity in the graupel fallspeeds with height led to localized centers of very high graupel content and the result was time-decoupling of the solution. (The graupel content at a level would oscillate drastically with each time step as the solution at the even time steps had separated from the solution at odd time steps.) Thus it was decided that N_{tg} should remain constant for each sub-class. Due to the high fallspeeds (which made small time steps necessary to avoid numerical instability) and the excessive reflectivities ($\approx$80 dBz) associated with the "hail" value of N_{tg} (10^{-6} cm^{-3}) it was decided to use the higher "graupel" value (10^{-4} cm^{-3}), keeping in mind that this would give much lower maximum (mean) graupel diameters and reflectivities. This explains why the model maximum mean diameter is only 0.2 cm ("hail" sub-class) compared to observed stone diameters of 0.5 to 2.0 cm. It is simply the choice of N_{tg} as discussed above which limits this parameter. (A choice of 10^{-6} cm^{-3} for N_{tg}, given the same maximum graupel content, would have given a maximum mean diameter closer to 1 cm.)

Another alternative would be to allow N_{tg} to vary internally, i.e. let N_{tg} be a continuous function of the graupel processes (such as melting and advection) that would alter the particle concentration. However, this would involve carrying N_{tg} and recalculating it at each point and time step (as done by Koenig and Murray, 1976), adding to the complexity of the scheme and to the execution time. Carrying N_{tg} would, though, allow such N_{tg}-altering processes as ice multiplication (splintering) to be incorporated into the model. The three graupel sub-classes could then be eliminated or kept. If they were kept, the number concentration as well as the graupel content would determine the mean mass or the appropriate sub-class.

Another improvement would be to use a bulk water scheme similar to that employed for snow; i.e. assume an inverse exponential distribution where all the slope parameters (N_{og}, N_{tg}, λ) are functions of the graupel content. To do this, however, more information is required such as a relationship between the graupel fall rate and the graupel content (like equation (11) for snow) but no such relationship for graupel was available.

Probably the best choice would be to make two or three separate and distinct classes from the three subclasses to model both graupel and hail. Each class would contain a unique ice particle distribution which could be distinguished by a different particle density and/or number concentration (either constant or varying). The means of initiation could determine into which class the graupel content at a point would fall. For example, ice particles initiated from ice crystals might be classified as low-density graupel while particles arising from drop freezing would fall into the higher-density heavy graupel or hail class. Thus, light graupel, heavy graupel and hail could all be present at a given point, an impossibility in the present scheme.

The alternatives suggested above would all add complexity to the scheme and increase execution time (already very long). However, the added realism of the results achieved by one of these modifications might justify the extra work and time involved. It is clear, though, that the bulk water aspect must be retained for the graupel parameterization in this cloud model if execution time is to be kept within reasonable limits.

In general, the graupel-related processes were well simulated. Of all the processes, the conversion of snow crystals to graupel is probably the most important, as it is the main source of graupel which, in addition to depleting large amounts of cloud water, is the main source of rain water.

It is this process, however, that could use some modification (as suggested in Chapter 3). In the present formulation of this process, the entire ice/snow content at a point is transferred to graupel when the median volume diameter, D_{oi} (calculated from the ice/snow content), reaches a specified threshold value. Thus initial graupel contents at conversion points tend to be quite large. This is perhaps too gross an approximation of the actual conversion of ice/snow crystals into graupel particles in clouds. Consideration should be given to the mode of crystal growth. For example, a crystal can grow to conversion size through vapor deposition while retaining its crystal nature (i.e. it cannot be called graupel), while ice crystals that have mainly grown by the riming of cloud water could be called "graupel" even before they reach conversion size. Thus, a distinction similar to that made by Stephens (see Chapter 3) should be made when transferring ice/snow mass to graupel mass. He made this distinction by using a rate of conversion based on the rate of crystal riming. If the amount of crystal-rimed mass exceeded a pre-specified fraction of the snow mixing ratio, the entire snow crystal content at a point was converted into graupel. In addition, a "mass conversion threshold" for the ice/snow content was set and any ice/snow content in excess of this threshold was converted into graupel (regardless of the method of ice/snow growth).

Another alternative would be, given a snow distribution, to convert only the mass contained in those crystals whose diameters are greater than the conversion diameter (as suggested by Stephens). However, with the present ice/snow scheme, this would alter the distribution in such a way as to unrealistically increase the number of smaller snow crystals (see equation (12)). Other possibilities include experimenting with the value of the conversion diameter or using separate classifications for rimed crystals and large, insignificantly rimed crystals or crystal aggregates (snow). With improvements to the conversion process, which was partly responsible for the differences between the model and observed storms in the dissipating stage referred to in Section 6.1.3, it is expected that the model results will be in better agreement with observation.

To conclude, the microphysical parameterization used in this cloud model gave acceptable results but with some modifications and "fine-tuning", especially those mentioned above, it could be improved.

6.4.2 Additional suggested reasons for model-observation differences

The most likely cause, apart from the microphysics, for the differences between the model and observed storm is the model storm environment. To begin with, the limited domain combined with the somewhat unnatural (lateral) periodic boundary conditions already places unrealistic restrictions on storm growth. A way to improve this is suggested in Chapter 7 as a possibility for further work. In addition, there are uncertainties in the initial conditions as given by the sounding (Figures 4 and 5). The sounding, taken 70 km away from the storm site, may not be entirely representative of the actual conditions at the storm site. Also, due to uncertainties in the sounding above the 350 mb level in the closest radiosonde sounding available (given by Chisholm,1970), a sounding from Edmonton, 206 km away from the storm, had to be used to give the temperature and humidity profiles above that level. The atmospheric sounding is used to give the initial (basic) state for the model and is thus very important in determining subsequent convective development (as is, to a lesser extent, the humidity impulse used to initiate convection). Therefore, any uncertainty in the sounding should be considered.

It is possible as well that the environmental conditions at the dissipating stage of the storm's development were significantly altered from the initial state by both the storm processes and the motion of the storm into a new environment. The basic state environment for the model storm, however, does not change for the duration of the simulation.

Finally, it should be remembered that Chisholm (1970) gave only three radar "snapshots" of the observed storm and these were only from one cell of a multicell storm. Thus, an attempt was made to pick three corresponding times from the model results. It is conceivable, though, that other times from the observed storm may have compared better with the model sections. It should also be recalled that the orientation of the vertical cross-sections presented for the model results was not exactly equivalent to that used by Chisholm (as explained in Chapter 5). This could give rise to apparent differences between the model and observed storms.

CHAPTER 7

SUMMARY AND CONCLUSION

7.1 Summary

For the realistic simulation of a hailstorm, a 3D numerical cloud model with full ice-phase (ice, snow, graupel and hail) is necessary. By necessity, the microphysics should be as simple, yet comprehensive, as possible to keep complexity and execution time to a minimum. The purpose of this research was to simulate a hailstorm by adding a graupel parameterization to complete the microphysics of the Steiner-Yau cumulus cloud model. The bulk water parameterization of graupel suggested by Stephens (1979) was considered adequate, and so, with some minor modifications, it was added to the cloud model.

This parameterization scheme assumed that graupel originated as frozen raindrops and rimed ice crystals and followed an inverse exponential size distribution characterized by a constant number concentration. The graupel content at a point determined what sub-class particle represented the graupel distribution: light graupel, heavy graupel, or hail. The assumed particle density and fallspeed varied accordingly. The graupel content could grow by vapor deposition and collection of cloud and rainwater, and was depleted by melting, sublimation and fallout.

A hailstorm was simulated in a 32 x 32 x 12 km domain with grid lengths of 1 km in the horizontal and 0.5 km in the vertical. The vertical boundaries were rigid and free-slip, while lateral boundaries were assumed periodic. Initial conditions (basic state) were given by a real sounding taken near the observed storm used for comparison purposes and given by Chisholm (1970). A saturated parabolic humidity impulse at the center of the domain initiated convection and 53 minutes of storm life were simulated.

A large, essentially vertical storm with ice/snow, rain and graupel was produced which reached its maximum intensity at the 31-minute mark. Graupel arose mainly from ice/snow conversion and grew by riming and deposition. The main region of graupel growth and formation was oriented vertically along the main updraft (w_{max}) axis. Melting of graupel produced a large amount of rain below the 0°C level. The fallout of rain and graupel produced a downdraft which cut off the updraft higher up and this, along with the depletion of cloud by ice particle riming and evaporation, caused the storm to dissipate. The interaction of the flow with the storm created a marked overhang on the outflow side of the storm, a feature which persisted for the duration of the run. The effects of condensate on the temperature and pressure fields and on the flow (i.e. the microphysics-dynamics interactions) were particularly well simulated, such as the region of cool sinking air and high pressure below the cloud base associated with the evaporation (and melting) of precipitation as it falls to the surface. Maximum graupel contents reached 2.9 g kg^{-1} in the storm and 1.45 g kg^{-1} at the surface at the time of maximum storm intensity (w_{max}). A maximum rainfall rate of 36 mm hr^{-1} was produced by the melting graupel at the same time. The maximum reflectivity of 62 dBz was connected with the graupel maximum. The storm grew to maximum dimensions of 10 km by 8 km by 9.5 km. Restricting the simulation to two dimensions resulted in a smaller, less vigorous storm with correspondingly smaller maxima (w, graupel, rain, etc.).

The results were compared to a storm reported by Chisholm which produced hail of up to 2.0 cm in diameter and maximum reflectivities between 65 and 79 dBz. Both model and observed storms were essentially vertical and exhibited radar overhangs. They were both of similar (horizontal) dimensions, had cloud bases at similar levels, and traveled in the same direction. Elliptical radar echoes in the horizontal were evident in the observed and model storms. Differences in reflectivity maxima, maximum graupel diameter at the surface, maximum storm top height, and dissipation between the model and observed storms could, for the most part, be explained by inadequacies of the microphysical parameterization and differences in real and model atmospheric conditions.

Suggestions were made on how to improve the existing parameterizations. Particular criticism was focused on the method of representing graupel and the conversion of ice/snow to graupel. It was determined that to properly model both graupel and hail, a single particle category ("graupel") with one constant representative total particle concentration (N_{tg}) is not sufficient. Either N_{tg} should be allowed to vary internally or two or more separate categories should be used, each with an appropriate N_{tg}. It was also determined that the growth mode of ice/snow should be considered when converting ice/snow to graupel. In addition, a gradual or partial conversion of the ice/snow content at a point was considered preferable to the conversion of the entire content.

7.2 Conclusion

The Steiner-Yau 3D cumulus cloud model, with graupel microphysics added by the author, represents an invaluable tool in the attempt to better understand, simulate, predict, and control storms. At the least, the present model provides an excellent starting point or base for further work in numerical storm modeling. In its present state, the model faithfully and realistically simulated the general dynamical and microphysical characteristics common to large storms using relatively few (microphysical) equations embracing, in a simple manner, most of the important precipitation processes. The use of three dimensions eliminates the restrictions imposed by one- and two-dimensional models, and gives added realism to the results. With the improvements suggested in Chapter 6 and the next section (7.3), the model should be entirely adequate for the variety of uses suggested in Section 7.3. It is the hope of the author that it will be improved and eventually used to aid in the study of that fascinating display of atmospheric violence, the hailstorm.

7.3 Suggestions for further work

1. As mentioned above, the graupel parameterization should be modified so as to better model both graupel and hail. This would involve a provision for N_{tg} to vary internally and/or the addition of another class of condensate or any other method that would more realistically distinguish between the different categories of ice particles as defined in the introduction (Chapter 1). The ice/snow-to-graupel conversion should be modified as well, to better simulate this important process.

2. To make the ice-phase parameterization more complete, the ice multiplication process and the wet growth mode for graupel/hail could be included (as discussed in Chapter 3).

3. The present model has only been used with one sounding and compared to one storm, as reported by Chisholm (1970). Many other soundings, with corresponding observations of the resulting storms, are available, not only in Chisholm's 1970 thesis but in other publications as well. It would be particularly interesting to run the model with soundings that showed strong wind shear and which were associated with high-energy storms exhibiting such features as a pronounced bounded weak echo region (BWER), an anvil and a tilted orientation. (The time step, however, would have to be reduced to avoid numerical instability due to the high velocities involved.) In the process of simulating different types of storms, the model could be "fine-tuned"; i.e. parameters and threshold values could be adjusted to give the best results for all types of storms.

4. Apart from the microphysics, the area which is in the greatest need of improvement is the boundary conditions. The surface boundary could be modified to include the effects of precipitation evaporation, surface heating, and cloud shadow effects. The lateral boundary conditions should be changed from periodic to allow for the inflow of additional heat and moisture from outside the domain. This additional energy from outside the domain might encourage the formation of multi-cell storms and would certainly add to the realism of the modeled environmental conditions. To avoid the possibility of the storm moving out of the domain, a larger or moving domain might be considered.

5. The present model uses a large amount of computer time to simulate only 53 minutes of storm time. This limits somewhat the additions that can be made to the model and its applications. Thus, it would be worthwhile to somehow "streamline" the program, making it more efficient and reducing the execution time.

6. Practical uses

There are many practical uses for the model. The model could be used to predict severe storms and large hail by simply "feeding in" a given (or forecast) radiosonde and observing the generated storm. By observing the actual storm and comparing it with the predicted model storm, additional improvements could be made over a period of time to make the model forecast more accurate.

There is a large amount of research currently being done in the area of cloud seeding and hail suppression. Different control methods could easily be tested using the cloud model before they are applied to real clouds, thereby saving time and money and hopefully providing information on what methods are best and how they should be employed.

In addition to the above uses, the model could also be used to examine cloud ensembles, squall lines, multicellular storms, storm rotation, frontal convection, and many other phenomena connected with clouds and storms.

REFERENCES

Asai, T., 1965: A numerical study of the airmass transformation over the Japan Sea in winter. J. Meteor. Soc. Japan, 43, 1-15.

Asselin, R., 1972: Frequency filter for time integrations. Mon. Wea. Rev., 100, 487-490.

Bigg, E.K., 1953: The supercooling of water. Proc. Phys. Soc. London, B66, 668-694.

Browning, K.A. and F.H. Ludlam, 1960: Radar analysis of a hailstorm. Tech. Note No. 5, Contract AF61(052)-254, Dept. of Meteor., Imperial College, London, 109 pp.

__________ and __________, 1962: Airflow in convective storms. Quart. J. Roy. Meteor. Soc., 88, 117-135.

Charlton, R.B. and R.J. List, 1972: Hail size distributions and accumulation zones. J. Atmos. Sci., 31, 2148-2152.

Chisholm, A.J., 1970: Alberta Hailstorms: A Radar Study and Model. Ph.D. thesis, Dept. of Meteor., McGill University, Montreal, 237 pp.

__________ and M. English, 1973: Alberta hailstorms. A.M.S. Meteor. Monogr. No. 14, 98 pp.

Cotton, W.R., 1972: Numerical simulation of precipitation development in supercooled cumuli, I and II. Mon. Wea. Rev., 100, 757-784.

__________, 1975: On parameterization of turbulent transport in cumulus clouds. J. Atmos. Sci., 32, 548-564.

Danielson, E.F., R. Bleck, and D.A. Morris, 1972: Hail growth by stochastic collection in a cumulus model. J. Atmos. Sci., 29, 135-155.

Deardorff, J.W., 1970: A numerical study of three-dimensional turbulent channel flow at large Reynolds numbers. J. Fluid Mech., 41, 453-480.

__________, 1972: Numerical investigation of neutral and unstable planetary boundary layer. J. Atmos. Sci., 29, 91-115.

Dennis, A.S. and D.J. Musil, 1973: Calculations of hailstone growth and trajectories in a simple could model. J. Atmos. Sci., 30, 278-288.

Douglas, R.H., 1963: Size distribution of Alberta hail samples. Sci. Report MW-36, Stormy Weather Group, McGill University, Montreal, 55-70.

__________, 1964: Size spectra of Alberta hail. National Conference on Physics and Dynamics of Clouds. A.M.S., Chicago, Illinois.

__________, 1965: Size distribution of Alberta hail samples. Sci. Report MW-42, Stormy Weather Group, McGill University, Montreal, 43-48.

Federer, B. and A. Waldvogel, 1975: Hail and raindrop size distributions from a Swiss multicell storm. J. Appl. Meteor., 14, 91-97.

Fletcher, N.H., 1969: The Physics of Rainclouds. The Cambridge University Press, New York, N.Y., 390 pp.

Gokhale, N.R. and K.M. Rao, 1969: Theory of hail growth. J. Rech. Atmos., 4, 153-178.

Hallett, J. and S.C. Mossop, 1974: Production of secondary ice particles during the riming process. Nature, 249, 26-28.

Hill, G.E., 1974: Factors controlling the size and spacing of cumulus clouds as revealed by numerical experiments. J. Atmos. Sci., 31, 646-673.

Hindman, E.E. and D.B. Johnson, 1972: Numerical simulation of ice particle growth in a cloud of supercooled water droplets. J. Atmos. Sci., 29, 1313-1321.

Hitschfeld, W. and R.H. Douglas, 1963: A theory of hail growth based on studies of Alberta storms. Z. Agnew. Math. Phys., 14, 554-562.

Jayaweera, K., 1971: Calculations of ice crystal growth. J. Atmos. Sci., 28, 728-736.

Jones, R.F., 1959: Size distribution of ice crystals in cumulonimbus clouds. Quart. J. Roy. Meteor. Soc., 86, 187-194.

Kessler, E., 1969: On the Distribution and Continuity of Water Substance in Atmospheric Circulation. A.M.S. Meteor. Monogr. No. 32, 84 pp.

Knight, C.A. and N.C. Knight, 1970a: Hailstone embryos. J. Atmos. Sci., 27, 659-666.

__________ and __________, 1970b: Lobe structure of hailstones. J. Atmos. Sci., 27, 667-671.

Knight, C.A. and N.C. Knight, 1970c: The falling behavior of hailstones. J. Atmos. Sci., 27, 672-681.

Koenig, L.R., 1966: Numerical test of the validity of the drop freezing/splintering hypothesis of cloud glaciation. J. Atmos. Sci., 23, 726-740.

__________, 1971: Numerical modeling of ice deposition. J. Atmos. Sci., 28, 226-237.

__________, 1972: Parameterization of ice growth for numerical calculations of cloud dynamics. Mon. Wea. Rev., 100, 417-423.

__________ and F.W. Murray, 1976: Ice-bearing cumulus cloud evolution: Numerical simulation and general comparison against observation. J. Appl. Meteor., 15, 747-762.

__________, 1977: The rime-splintering hypothesis of cumulus glaciation examined using a field-of-flow cloud model. Quart. J. Roy. Meteor. Soc., 103, 585-606.

Langleben, M.P., 1954: The terminal velocity of snowflakes. Quart. J. Roy. Meteor. Soc., 80, 174-181.

List, R., 1963: General heat and mass exchange of spherical hailstones. J. Atmos. Sci., 20, 189-197.

__________, R.B. Charlton, and P.I. Buttals, 1968: A numerical experiment on the growth and feedback mechanisms of hailstones in a one-dimensional steady state model cloud. J. Atmos. Sci., 25, 1061-1074.

Ludlam, F.H., 1958: The hail problem. Nubila, 1, 12-95.

Macklin, W.C., 1962: The density and structure of ice formed by accretion. Quart. J. Roy. Meteor. Soc., 88, 30-50.

__________, 1963: Heat transfer from hailstones. Quart. J. Roy. Meteor. Soc., 90, 84-90.

Manton, M. and W. Cotton, 1977: Formulation of approximate equations for modeling moist deep convection on the mesoscale. Dept. of Atmos. Sci., Paper No. 266, Colorado State University, Ft. Collins, Colorado, 62 pp.

Marshall, J.S. and W. McK. Palmer, 1948: The distribution of raindrops with size. J. Appl. Meteor., 5, 165-166.

Marwitz, J.D., 1972a: The structure and motion of severe hailstorms. Part I: Supercell storms. J. Appl. Meteor., 11, 166-179.

__________, 1972b: The structure and motion of severe hailstorms. Part II: Multicell storms. J. Appl. Meteor., 11, 180-188.

__________, 1972c: The structure and motion of severe hailstorms. Part III: Severely sheared storms. J. Appl. Meteor., 11, 189-201.

Mason, B.J., 1956: On the melting of hailstones. Quart. J. Roy. Meteor. Soc., 82, 209-216.

Michaud, R., 1980: Initialization of a cumulus cloud model by using random surface conditions. M.Sc. thesis, McGill University, Montreal, 85 pp.

Miller, M.J., 1978: The Hampstead storm: A numerical simulation of a quasi-stationary cumulonimbus system. Quart. J. Roy. Meteor. Soc., 104, 413-427.

Musil, D.J., 1970: Computer modelling of hailstone growth in feeder clouds. J. Atmos. Sci., 27, 474-482.

________, P.L. Smith, Jr., and A.J. Heymsfield, 1978: Total hydrometeor spectra in a hailstorm and implications for precipitation growth processes. Conference on Cloud Physics and Atmospheric Electricity, A.M.S., Issaquah, Washington, 173-177.

Orville, H.D. and F.J. Kopp, 1977: Numerical simulation of the life history of a hailstorm. J. Atmos. Sci., 34, 1596-1618.

Pruppacher, H.R. and J.D. Klett, 1978: Microphysics of Clouds and Precipitation. D. Reidel Publishing Company, Dordrecht, Holland, 714 pp.

Schlesinger, R.E., 1975: A three-dimensional numerical model of an isolated deep convective cloud: Preliminary results. J. Atmos. Sci., 32, 934-957.

________, 1978: A three-dimensional model of an isolated thunderstorm. Part I: Comparative experiments for variable ambient wind shear. J. Atmos. Sci., 35, 690-713.

Scott, B.C. and P.V. Hobbs, 1977: A theoretical study of the evolution of mixed-phase cumulus clouds. J. Atmos. Sci., 34, 812-826.

Sekhon, R.S. and R.C. Srivastava, 1970: Snow size spectra and radar reflectivity. J. Atmos. Sci., 27, 299-307.

Simpson, J. and V. Wiggert, 1969: 1968 Florida seeding experiment: Numerical model results. Mon. Wea. Rev., 97, 471-489.

Smith, P.L., Jr., C.G. Myers, and H.D. Orville, 1975: Radar reflectivity factor calculations in numerical cloud models using bulk parameterization of precipitation. J. Appl. Meteor., 14, 1156-1165.

Steiner, J.T., 1973: A three-dimensional model of cumulus cloud development. J. Atmos. Sci., 30, 414-435.

Stephens, M.A., 1979: A Simple Ice Phase Parameterization. M.Sc. thesis, Atmos. Sci. Paper No. 319, Dept. of Atmos. Sci., Colorado State University, Fort Collins, Colorado, 122 pp.

Takahashi, T., 1976: Hail in an axisymmetric cloud model. J. Atmos. Sci., 33, 1579-1601.

Turpeinen, O. and M.K. Yau, 1981: Comparisons of results from a three-dimensional cloud model with statistics of radar echoes on day 261 of GATE. Mon. Wea. Rev., 109.

Weinstein, A.I., 1970: A numerical model of cumulus dynamics and microphysics. J. Atmos. Sci., 27, 246-255.

Wisner, C.W., et al, 1972: A numerical model of a hail bearing cloud. J. Atmos. Sci., 29, 1160-1181.

Yau, M.K. and P.M. Austin, 1979: A model for hydrometeor growth and evolution of raindrop size spectra in cumulus cells. J. Atmos. Sci., 36, 655-668.

__________, 1979a: Perturbation pressure and cumulus convection. J. Atmos. Sci., 36, 690-694.

__________, 1979b: Modeling of cloud dynamics. Report for Atmospheric Environment Service, AES Contract Serial No. OSU78-00258, Dept. of Meteorology, McGill University, Montreal, 21 pp.

__________, 1980a: The effects of evaporation, water load and wind shear on cloud development in a three-dimensional numerical model. J. Atmos. Sci., 37, 488-494.

__________, 1980b: A two-cylinder model of cumulus cells and its application in computing cumulus transports. J. Atmos. Sci., 37, 2470-2485.

Young, K.C., 1975: Growth of the ice phase in strong cumulonimbus updrafts. Pure and Appl. Geophys., special issue: Cloud Dynamics, ed. Hans R. Pruppacher, 1005-1017.